ABSTRACT

ROBLES POBLETE, FELIPE. Rate-dependent Interfacial Mechanics in Advanced Material Systems. (Under the direction of Dr. Yong Zhu).

An important branch of applied mechanics involves the category of problems which examines the mechanical behavior of contact regions. There are an extensive number of engineering applications that require one material to be bonded to another. Examples of these applications include adhesive joints, composite materials, protective coatings, and thin films used in the fabrication of microelectronics devices. A great deal of research has been devoted in order to develop techniques to predict the strength of the bond by endowing the interface with its own characteristic constitutive response, rather than plainly assuming it to be frictionless or perfectly bonded. In this dissertation, rate-dependent contact problems in different advanced materials systems were studied in order to better understand their behaviour at certain loading conditions.

First, the interlayer mechanical properties and adhesion between glass and Saflex^{TM} polyvinylbutyral (PVB) was studied. The adhesion characterization was accomplished by carrying out mode 1 and mode 2 fracture mechanics experiments of laminated glass-PVB specimens. The traction-separation laws for modes 1 and 2 obtained were used in the development of a finite element model of the crack initiation. The results presented were important to determine the resistance of laminated glass under certain loading conditions and contribute to a better understanding of the mechanism involved on the failure of laminated glass.

Second, this work reports on the nonlinear and cohesive shear-lag analysis of the interfacial shear stress transfer between a single silicon nanowire (SiNW) on top of two types of substrates under tensile loading: nontreated and 45 min. UVO-treated poly-(dimethylsiloxane) (PDMS COMPOSITE). Finite element analysis (FEA) was used to obtain the interface properties by fitting the average strain from experimental data. The model also provided the strain distribution along

the SiNW, which is compared to the analytical results. Nonlinear shear-lag model was used to quantify the adhesion between SiNW and nontreated PDMS COMPOSITE, which is characterized by weak and time-independent dispersion forces (type of van der Waals force). In contrast, cohesive shear-lag model was adopted to study the adhesion between SiNW and UVO-treated PDMS COMPOSITE, which is explained by a strong and time-dependent chemical (condensation) reaction. Similar analysis was used in the interfacial characterization between silver nanowire (AgNW) and PDMS COMPOSITE substrate, which is applied in the study of not only the stretching, but also the buckling and fracture of AgNWs. The information presented contributes to a better understanding of the mechanics behind the adhesion between 1D nanomaterials and elastomeric substrates as well as provide relevant information to help in the assembly of NW-based flexible/stretchable electronic devices.

Last, the contact modeling of the nanoindentation of aluminum oxide (Al_2O_3) and zinc oxide (ZnO) nanolattice films is presented. The mechanical properties of both nanolattice films were tested by applying uniaxial compressive loading through nanoindentation. FEA modeling was used to analyze energy absorption of the nanolattice material. Nanoindentation experiments were also conducted in order to investigate the anelastic behavior of these materials, which presents itself as the gradual full recovery of deformation once the load is removed, leading to dissipation of internal mechanical energy. FEA modeling was also employed to model the anelastic response of the nanolattice films under nanoindentation.

© Copyright 2018 by Felipe Robles Poblete

All Rights Reserved

Rate-dependent Interfacial Mechanics in Advanced Material Systems

by
Felipe Robles Poblete

A dissertation submitted to the Graduate Faculty of
North Carolina State University
in partial fulfillment of the
requirements for the degree of
Doctor of Philosophy

Mechanical Engineering

Raleigh, North Carolina
2018

APPROVED BY:

_____	_____
Yong Zhu Committee Chair	Jan Genzer
_____	_____
Fuh-Gwo Yuan	Chih-Hao Chang

DEDICATION

I dedicate this work to God Almighty, my source of strength, knowledge and understanding. I also dedicate this work to my parents, Maria Isabel Poblete e Richard Isaias Poblete who have supported me and guided me throughout my life. To my wife Jingxi Liang who has encouraged me all the way and has given me all the emotional support and help I needed to finish this endeavor. To my sons Mark and Luke who fill me with joy every day.

BIOGRAPHY

Felipe Robles Poblete is from Sao Paulo, Brazil. He obtained his Bachelor's degree in aeronautical engineering from the University of Sao Paulo in 2012. Following graduation he joined Dr. Zhu's lab at North Carolina State University and in 2014 he decided to pursue a PhD degree under Dr. Zhu's guidance. His research interests include interface mechanics, mechanical testing, and finite element modeling.

ACKNOWLEDGMENTS

I would like to thank my PhD advisor, Dr. Yong Zhu, for his guidance and support through my PhD career. I also thank all my colleagues in Dr. Zhu's group: Dr. Guangming Cheng, Dr. Jimmy Chang, Dr. Shanshan Yao, Dr. Qijin Huang, Dr. Jianxun Cui, Chengjun Li, and Zheng Cui. Thank you for all your help with experiments.

I'm thankful to Professors Fuh-Gwo Yuan, Chih-Hao Chang, and Jan Genzer for kindly serving as my Committee members. I'm also thankful to Dr. Michael Dickey for serving as a Committee member during my Prelim exams. Thank you for the comments and suggestions, which help greatly to improve this dissertation.

I would also like to thank EASTMAN for financial assistance and feedback provided to part of my work. I thank Dr. Feng Xu, Dr. Kunal Mondal, and I-Te Chen for providing experimental results necessary to the completion of my research. Finally, I'd like to thank Dr. James Kribs, John Cameron, and Neil Bain for help with experimental setup and fabrication of samples.

TABLE OF CONTENTS

LIST OF TABLES

LIST OF FIGURES

CHAPTER 1 Measuring the Traction-Separation Law for PVB/Glass Interface

1.1 Introduction

Laminated safety glass is manufactured by bonding a polymeric layer to two or more glass plies under high pressure and temperature[1]. Under these conditions, a strong bonding between the polymer's hydroxyl groups and the glass' silanol groups[2] is developed. In applications such as in automotive windshields, the shear coupling generated by the interlayer[3] prevents the glass laminate from shattering once it's impacted as the glass fragments remain connected to it. Thus, the interlayer greatly improves the post-glass fracture phase while reducing the possibility of injury that could be caused by scattered glass shards. Glass laminates are also commonly used in architectural glazing, in which long term stability is a key factor to be evaluated taking into account the presence of visual defects and delamination. Polyvinyl butyral (PVB) is the most frequent used interlayer material in industry due to its high adhesive power and enhanced optical qualities. Another recent application of glass-PVB laminates is in the car roofs, improving the habitability of the vehicle. This situation requires the laminate to sustain higher loads at considerable lower rates.

Early researchers focused on the study of the mechanical properties of each laminate component separately. Experiments were conducted to evaluate the laminate failure pressure[4-6], as well as finite element models have been proposed[7-9]. Nevertheless, the characterization of the interface fracture between glass and PVB is critical in order to understand the behavior of the glass laminate. The interfacial adhesion plays a key role in safety and durability of these laminates. High adhesion ensures that the glass shards are firmly attached to the polymer interlayer although it makes the laminate more susceptible to the penetration of objects. On the contrary, low adhesion means a higher impact resistance but also lower retention of shards.

In recent years, there has been several studies on glass-PVB adhesion through the investigation of fractured laminate deformation and delamination. The current framework of linear elastic fracture mechanics (LEFM) is difficult to be implemented due to large localized deformation of the interlayer polymer[10-11] and the impossibility of finding a defect large enough to be considered a crack[11]. In view of this limitation, other methods had to be applied. Several researchers have used an energy balance method[12-14], which equates the external work done to the strain energy stored in the interlayer and the energies dissipated by interlayer viscous deformation and interface delamination. Through cracked tension (TCT) specimens are predominantly used[12,14-16] to evaluate the interfacial shear fracture toughness (Mode 2) between glass and PVB. Other configurations also used are the double lap shear test[17] and the compression shear test[10]. Although it's claimed that pure Mode 2 fracture toughness can be obtained from these methods; there is a concern, especially for the last two configurations, that they may cause compression of and friction on the crack faces.

Moreover, the main limitation of the energy balance approach is that usually only one interfacial parameter, namely the interfacial energy release rate (fracture toughness), is obtained. On the other hand, cohesive zone modeling introduces a second fracture parameter: the cohesive strength, relating the fracture toughness to the critical crack-tip opening displacement required for crack propagation.

According to Dugdale, 1960; Barenblatt, 1962,[18] who first discussed the concepts of cohesive zone modeling, the failure process zone is characterized by a traction-separation law. This law relates the cohesive traction $\sigma(\delta)$, which varies along the process zone, and the local opening displacement, δ. Cohesive zone models have successfully been applied in the study of interfacial fracture problems. Earlier examples include the analysis done by Needleman, 1987;

Needleman, 1990[19-20] of void nucleation, growth and coalescence through the modeling of the crack plane using springs with a built-in traction-separation law. Tvergaard and Hutchinson, 1993; Tvergaard and Hutchinson, 1994[21-22] expanded this model in order to investigate interfacial debonding under mixed-mode conditions. More recently, Roe and Siegmund, 2003[23] developed a cohesive zone model that described the failure of adhesive-bonded composite under cyclic loading. In this case, the traction-separation behavior does not follow a predetermined traction-separation path and the damage evolution can vary from point to point.

The characterization of several interface problems have been carried out using cohesive zone modeling. Yang et al, 2001[24] modeled fatigue damage and crack growth in quasibrittle materials. Li and Chandra, 2003[25] studied the influence of crack-tip plasticity in the crack initiation and propagation in ductile elasto-plastic material. Yang and Cox, 2005[26] modeled the mixed mode damage evolution of cracks in laminated composites. Ji et al., 2010[27] studied the effect of adhesive thickness on the Mode 1 fracture of low carbon Steel plates bonded with epoxy. Traction-separation law rate dependency in quasi-static experiments has also been reported. Recently, Iwasaki et al, 2007[28] measured the traction-separation law for glass-PVB laminates at high loading rate. Karac et al., 2011[29] tested a tapered double cantilever beam composed of aluminum alloy bonded with epoxy at different loading rates. Rosa et al., 2012[30] adopted a time dependent cohesive model while studying the effect of loading rate in concrete failure.

The extraction of traction-separation relations can be done iteratively by determining parameters through comparison between numerical solutions and measured properties[31-32] or directly by simultaneously measuring the crack front displacement and the J-integral. The direct method was successfully employed by Sorensen et al., 2008[33] in the bridging of fiber composite subjected to Mode 1 delamination. Zhu et al, 2009[34] directly extracted Modes 1 and 2 traction-

separation laws for polyurea/Steel interfaces. Dastjerdi et al, 2013[35] employed a rigid DCB technique in order to directly obtain the traction-separation law for polyurethane, epoxy, and silicone adhesives. Gowrishankar et al, 2012[36] compared direct and iterative methods for determining the mode 1 traction-separation law for silicon-epoxy interface and concluded that the direct method provided more accurate results with the ease of parameter extraction.

The present paper has the objective of characterizing the interface between glass and PVB by directly obtaining traction-separation laws for modes 1 and 2 at different loading rates. First, we describe the experiment methods used to test the fracture behavior of the laminate. Next, we report the mode 1 and mode 2 traction-separation laws obtained for glass/PVB interface. These extracted laws are then directly input into finite element models, when the calculated force-extension curves are compared to the ones obtained through the experiments as a way to validate the models. Finally, the results and possible limitations encountered are discussed.

1.2 Experimental methods

This section describes the experiment procedures employed to obtain the modes 1 and 2 traction-separation laws for the glass/PVB interface. The glass-PVB sandwich specimens were provided by EASTMAN Chemical Company.

1.2.1 Test methods

The mode 1 traction-separation law was obtained through the use of a double cantilever beam (DCB) configuration. The specimen geometry and loading are shown in **Figure 1.1**. During the glass-PVB specimen fabrication, a preexisting crack was represented by the interfacial region between glass and PVB in which there is no PVB. Two Steel backing beams were added in order to decrease the stresses in the glass layer developed during the test, precluding its undesired brittle failure. Steel and glass were glued by an epoxy resin that avoided any relative displacement

between them. The backing beam thickness necessary to achieve this goal was found through FEA. In the FEA model, it was considered the bonding between glass and PVB to be perfect. Then, the structure was loaded as in the DCB test by applying a vertical displacement at the end of one of the beams while keeping the other beam fixed. **Figure 1.2** shows the maximum principal stress distribution along the length of the glass beam when a Steel backing beam with different thicknesses is attached to it. From the plot, it's noticed that the stress concentration is localized in the glass region just above where the PVB film starts (crack front). By increasing the Steel backing beam thickness to *1"*, it's possible to decrease the stress concentration in that region to about *100 MPa* which is below the tensile and compressive strength reported[37]. Because the DCB arm thickness was considerably large, their effect could not be neglected so that the J-integral was calculated based on a beam with elastic foundation[38].

$$J = \frac{12P^2a^2}{E_{fx}B^2h^3}\left[1 + 1.28\left(\frac{h}{a}\right)\left(\frac{E_{fx}}{E_z}\right)^{1/4} + 0.41\left(\frac{h}{a}\right)^2\left(\frac{E_{fx}}{E_z}\right)^{1/2}\right] \quad \textbf{(1.1)}$$

In the equation above, *P* is the applied load, *a* is the crack length, *h* is the adherent thickness, *B* is the specimen width, *Efx* is the specimen longitudinal elastic modulus and *Ez* is the specimen transverse elastic modulus. The longitudinal and transverse elastic moduli for the bimaterial beam were estimated by the composite theory of the rule of mixtures[39].

$$E_{fx} = \bar{h}E_{glass} + \bar{h}E_{Steel} \quad \textbf{(1.2)}$$

$$E_z = \left(\bar{h}E_{glass} + \bar{h}/E_{Steel}\right)^{-1} \quad \textbf{(1.3)}$$

$$\bar{h} = \frac{h_{glass}}{h_{glass}+h_{Steel}} \quad \textbf{(1.4)}$$

where E_{glass} and E_{Steel} are the Young's modulus of glass and Steel, respectively.

During the test, the Steel backing beam was subjected to stresses below its yield strength *(~500 MPa*) and glass is a brittle material. PVB is a polymeric resin considered to be a nonlinear

elastic material. Because all the materials involved presented an elastic stress-strain behavior, the J-integral approach could be applied. The J-integral along a path just outside the failure process zone is given by:

$$J = \int_0^{\tilde{\delta}_n} \sigma(\delta_n) d\delta_n \quad \textbf{(1.5)}$$

where δ_n and $\tilde{\delta}_n$ are the normal opening and normal end-opening of the cohesive zone, respectively, and σ is the normal traction. When $\tilde{\delta}_n$ achieves a critical normal end-opening value δ_{NC}, the J-integral reaches a steady state value. Because the J-integral is path independent, the relationship given by **Equation (1.5)** should yield the same result as equation **Equation (1.1)** and the entire failure process zone can be described by a cohesive law. Digital images of the normal end-opening $\tilde{\delta}_n$ yielding the differentiation of **Equation (1.5)** with respect to $\tilde{\delta}_n$ as follows:

$$\sigma(\tilde{\delta}_n) = \frac{\partial J}{\partial \tilde{\delta}_n} \quad \textbf{(1.6)}$$

Thus, the mode 1 traction-separation law was obtained by simultaneously measuring the applied load, which leads to the J-integral calculation, and the normal end-opening displacement $\tilde{\delta}_n$.

In the case of mode 2 fracture, a modified ARCAN shear mode testing technique[40] was adopted. **Figure 1.3** shows the loading apparatus and the specimen geometry for the test. The fixture was composed by a circular plate cut into half along the diameter with a square window in the center. Glass-PVB sandwich specimens were glued to the butterfly-shaped coupling by using the same epoxy resin adopted for the DCB tests. **Figure 1.3(a)**, **(b)**, and **(c)** show, respectively, schematics of the circular grip plate and the loading coupling with the specimen and an optical image of the entire setup.

The J-integral for the modified ARCAN specimen is given below:

$$J = \eta \frac{A}{Bb} \quad \textbf{(1.7)}$$

where η is a constant that depends on the ratio between the crack length and the specimen length, *A* is the area under the local load-displacement curve where the local shear displacement is the one accounted for, *B* is the specimen out-of-plane width, and *b* is the length of the uncracked ligament. For a *a/W* ratio equaling *0.5*, the constant η is assumed to be *0.9*.

The J-integral evaluation along a path just outside the failure process zone yields the following:

$$J = \int_0^{\tilde{\delta}_t} \sigma(\delta_t) d\delta_t \quad \textbf{(1.8)}$$

where δ_t and $\tilde{\delta}_t$ are the tangential opening and shear end-opening of the cohesive zone, respectively, and τ is the tangential traction. Differentiating **Equation (1.7)** with respect to δ_t gives:

$$J = \sigma\left(\tilde{\delta}_t\right) = \frac{\partial J}{\partial \tilde{\delta}_t} \quad \textbf{(1.9)}$$

Again, recording the path independence of the J-integral, **Equation (1.7)** and **(1.8)** results should be the same. Then, similarly to mode 1, the mode 2 shear traction-separation law was obtained through simultaneous recording of the J-integral and the shear end-opening displacement.

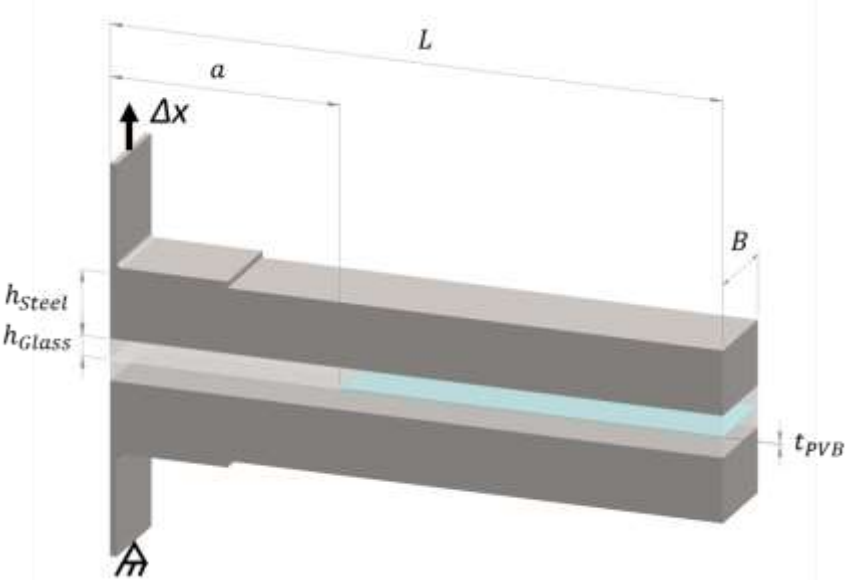

Figure 1.1 Schematics of the DCB test configuration and specimen (L = 240 mm, B = 36 mm, a = 90 mm, h_{Steel} = 25.4 mm, h_{Glass} = 8 mm, t_{PVB} = 0.3 mm).

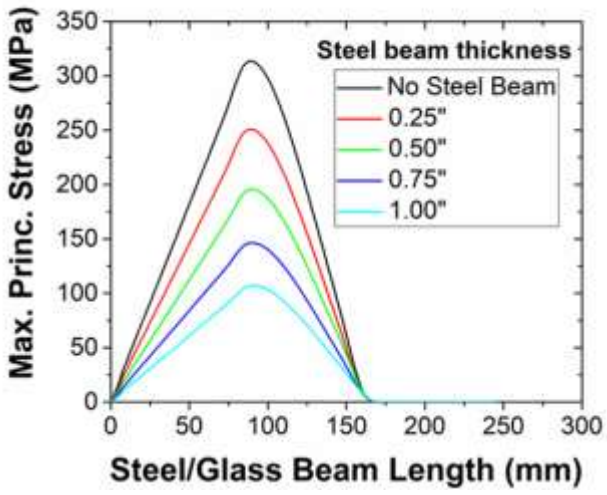

Figure 1.2 Stress concentration along the Steel/Glass beam length for the different Steel beam thicknesses.

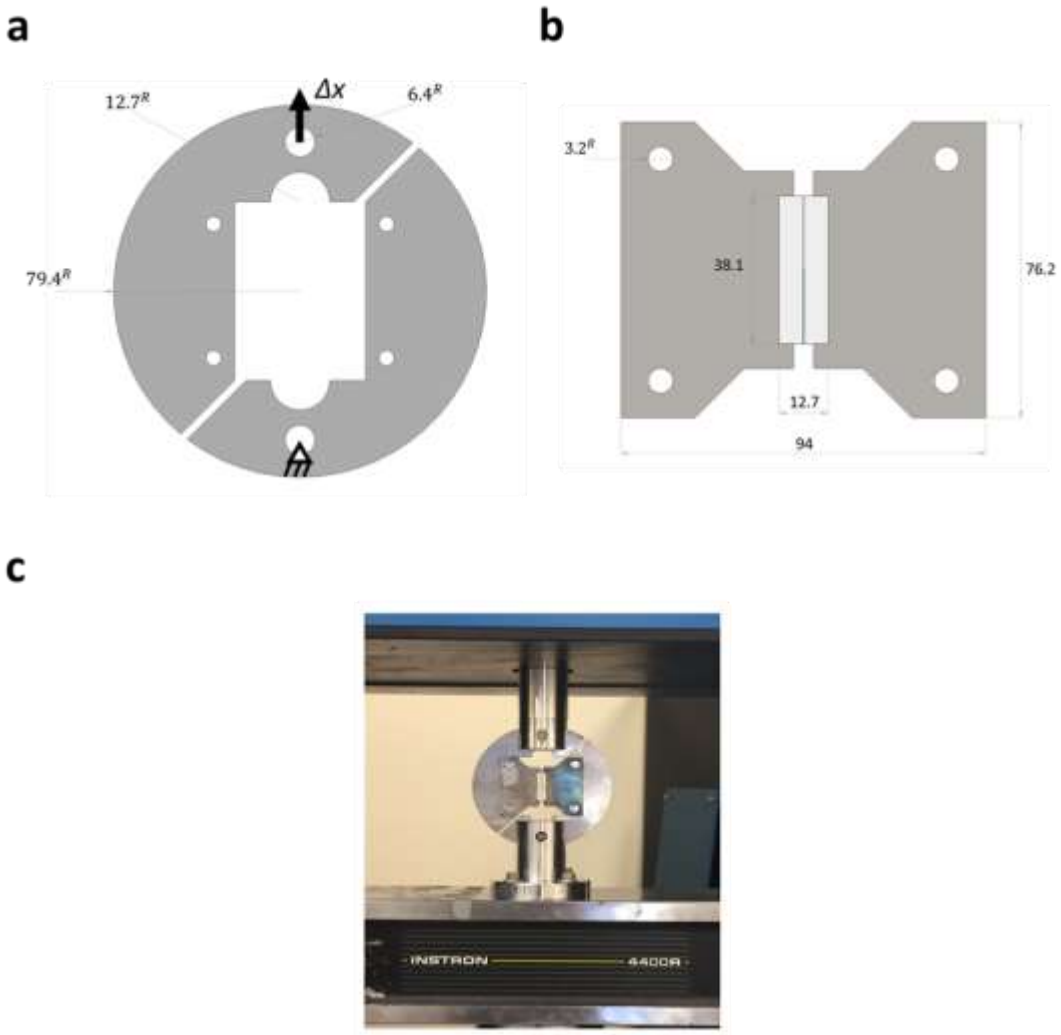

Figure 1.3 Schematics of the modified ARCAN test fixture and shear sample, including (a) the circular grips, (b) the coupling with specimen attachment, and (c) an optical image of the setup mounted in the Instron testing machine. All dimensions are in millimeters.

1.2.2 Test procedures

The glass-PVB sandwich specimens were prepared by EASTMAN. The DCB sample was modified by adding the aforementioned backing beams and hinges in order to attach the sample to the grip of the testing machine. Both modes 1 and 2 experiments were conducted by a servo hydraulic machine (Instron universal testing machine) under constant cross section speed and at room temperature. Simultaneously, the end-opening displacements were recorded by a CCD

camera, making it possible to monitor the initiation of separation and crack propagation. The analysis of the images taken of the exact end-opening displacement was important in order to quantify the fracture process in terms of traction-separation laws. The adherent deformation for both modes 1 and 2 was considered to be small compared to the bulk deformation of PVB and the separation across the glass-PVB interface. The image analysis took place after the experiments were conducted.

1.3 Results

1.3.1 Mode 1 fracture – experimental

DCB tests were conducted at seven loading rates ranging from *0.01* to *1.8 mm/min*. Tests conducted at a speed higher than 1.8 mm/min caused the glass substrate to fracture due to high stress. At least three samples were tested at a given loading rate. For each case, the J-Integral value was recorded along with the end-opening displacement. **Figure 1.4(a)** shows the increase of the J-integral with respect to the end-opening up to a steady-state value. The curve was then differentiated in order to obtain the traction-separation law. The derivative at a given point was computed by taking the average of the slopes between the points and its two closest neighbors. As the X data (end-opening displacement) was evenly distributed, the derivative curves were accurately smoothed using the Savitzky-Golay method (**Figure 1.4(b)**).

The images taken simultaneously were used to characterize the damage initiation and progress in the DCB specimens. In **Figure 1.5(a)** and **(b)**, it's possible to notice that following its initiation, the crack propagates at the interface between glass and PVB, which a priori characterized an adhesive failure. An analysis of the postmortem specimen (**Figure 1.5(c)**) with the naked eye showed no noticeable residue of PVB in one of the substrates for the range of loading rates tested. Further investigation under an optical microscope corroborated this observation.

The loading speed considerably affected the traction-separation law for glass-PVB. The peak cohesive stress, which is equivalent to the bond strength, was about *3.1 MPa* for the slowest loading rate tested (*0.1 mm/min*). For the faster rate used (*1.8 mm/min*), the peak cohesive stress was about *12.6 MPa* which is more than four times the value obtained for the first case. There was also an increase in the fracture energy (toughness), that is given by the area under the traction-separation law, with an increase in the loading rate. **Figure 1.6(a)** and **(b)** shows the J-integral and traction-separation law curves while **Table 1.1** has the important traction-separation law parameters for each loading rate tested.

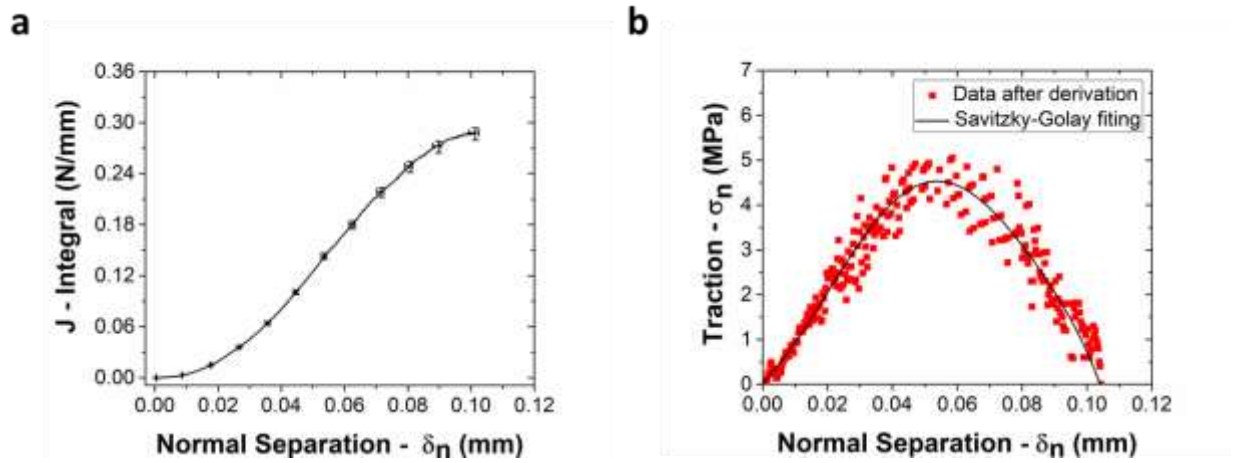

Figure 1.4 (a) J-integral vs. normal separation curve for the loading rate of 0.3 mm/min − δ_n and (b) traction-separation law obtained through differentiation and after applying the Savitzky-Golay method for the loading rate of 0.3 mm/min.

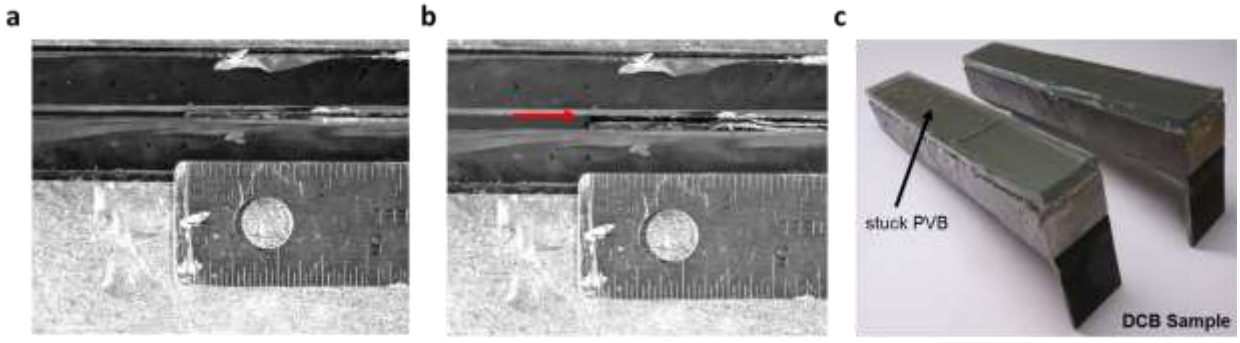

Figure 1.5 (a) Side view of the DCB specimen before testing and (b) Side view of the DCB specimen during testing showing the interfacial delamination. (c) Postmortem DCB specimen showing PVB film adhered to one of the substrates.

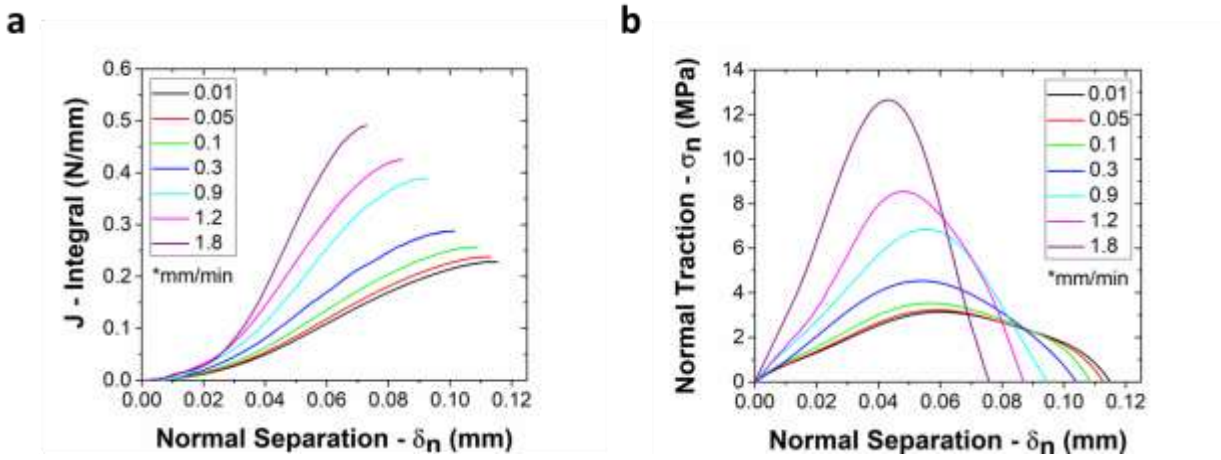

Figure 1.6 (a) J-integral vs. normal separation curve and (b) normal traction vs. normal separation curves for loading rates ranging from 0.01 to 1.8 mm min.

Table 1.1 Parameters of the mode 1 traction-separation law as a function of the loading rate.

Loading rate (mm/min)	Fracture energy, Γ_n (N/m)	Normal strength, σ_n (MPa)
0.01	236	3.1
0.05	242	3.2
0.1	258	3.5
0.3	293	4.5
0.9	384	6.9
1.2	430	8.5
1.8	477	12.6

1.3.2 Mode 2 fracture – experimental

As previously mentioned, a modified version of the Arcan configuration[34] was used in the mode 2 experiments. The experiment was conducted at several loading rates, ranging from *0.01* to *1.2* mm/min. The application of higher loading rates was precluded by the brittleness of the glass. The J-integral curves presented the same trend as the one found for the mode 1 fracture regarding the loading rate, as J increased with increasing shear end-opening δ_t until reaching a steady-state value. The traction-separation laws were obtained following the same method presented for mode 1 fracture. The crack initiation and propagation were recorded at the same time the test was being carried out. The images in **Figure 1.7(a)** and **(b)** shows that the crack propagates at the interface between glass and PVB, which characterizes an adhesive type of failure. This fact was further corroborate by observing that most, if not all, of the PVB film stuck to one of the glass substrates at the end of the test (**Figure 1.7(c)**).

Like it was seen for mode 1, the loading speed also affected the response of mode 2. As the loading rate increase from *0.01* to *1.2 mm/min*, the shear bonding strength ranged from *0.45* to *0.75 MPa*. A lower increase if compared to mode 1. In the same way, the fracture energy increased from *239* to *326 N/m*. **Figure 1.8(a)** and **(b)** shows J-integral and traction-separation law curves while **Table 1.2** presents the important parameters from the mode 2 traction-separation law at different loading rates.

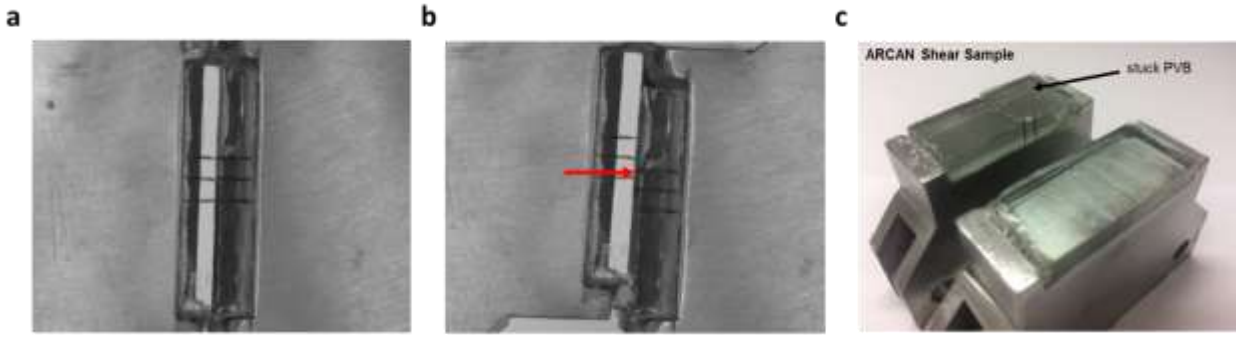

Figure 1.7 (a) Front view of the ARCAN Shear specimen before testing and (b) front view of the ARCAN Shear specimen during testing showing the interfacial delamination. (c) Postmortem ARCAN Shear specimen showing PVB film adhered to one of the substrates.

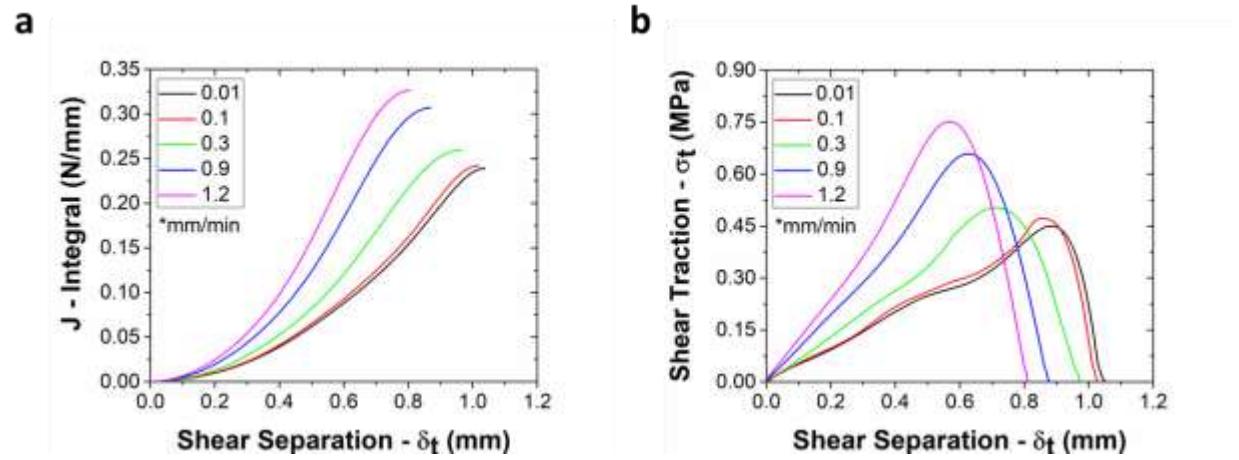

Figure 1.8 (a) J-integral vs. shear separation curve and (b) shear traction vs. normal separation curves for loading rates ranging from 0.01 to 1.2 mm min.

Table 1.2 Parameters of the mode 2 traction-separation law as a function of the loading rate.

Loading rate (mm/min)	Fracture energy, Γ_t (N/m)	Shear strength, σ_t (MPa)
0.01	239	0.45
0.1	242	0.47
0.3	259	0.50
0.9	307	0.66
1.2	326	0.75

1.3.3 Mode 1 fracture – FEA simulation

A FEA model of the DCB test was carried out in Abaqus 6.14. Cohesive elements were used to model the PVB layer and its constitutive response was given directly in term of traction versus separation. In this manner, the traction-separation laws obtained experimentally were input into the model by means of a user material subroutine (UMAT) written in FORTRAN language. The DCB test was analyzed as a 2D model. Both, glass and Steel, were modeled with 2D structural plane strain elements (8-node biquadratic – CPE8) while PVB was modeled with 2D cohesive elements (4-node – COH2D4). The substrate constitutive properties were assumed to be linear elastic. The Young's modulus and Poisson's ratio of Steel were taken as *190 GPa* and *0.305*, respectively. For glass, a Young's modulus of *72 GPa* and a Poisson's ratio of *0.23* were adopted. Different loading rates were considered in the simulation. The traction-separation law obtained experimentally was interpolated by a high-order polynomial function, resulting in a equation that relate stress (traction) and strain (separation). This equation could then be input into the UMAT. The subroutine was validated by testing and an one-element model. In order to evaluate the accuracy of the model representation and validate it, the FEA simulated force-extension curves were compared to the ones obtained experimentally. **Figure 1.9(a)** shows a very good agreement between these results for three different loading rates.

1.3.4 Mode 2 fracture – FEA simulation

The modified ARCAN shear test was also modeled by FEA. For this case, a 2D model could not be implemented due to the difference in thickness of the components. Nevertheless, cohesive elements with a traction-separation constitutive response were again used to model PVB. Glass and Steel used 3D structural elements (20-node quad brick – C3D20) while PVB was modeled with 3D cohesive elements (8-node – COH3D8). The Young's modulus and Poisson's

ratio for glass and Steel are the same values as used in the DCB model. Also, similarly to the mode 1 fracture model, UMAT subroutines were employed in order to input the traction-separation laws obtained experimentally at different loading rates. A good agreement between experiment and simulation force-extension curves were also achieved, as shown in **Figure 1.9(b)**, which validated the mode 2 fracture model.

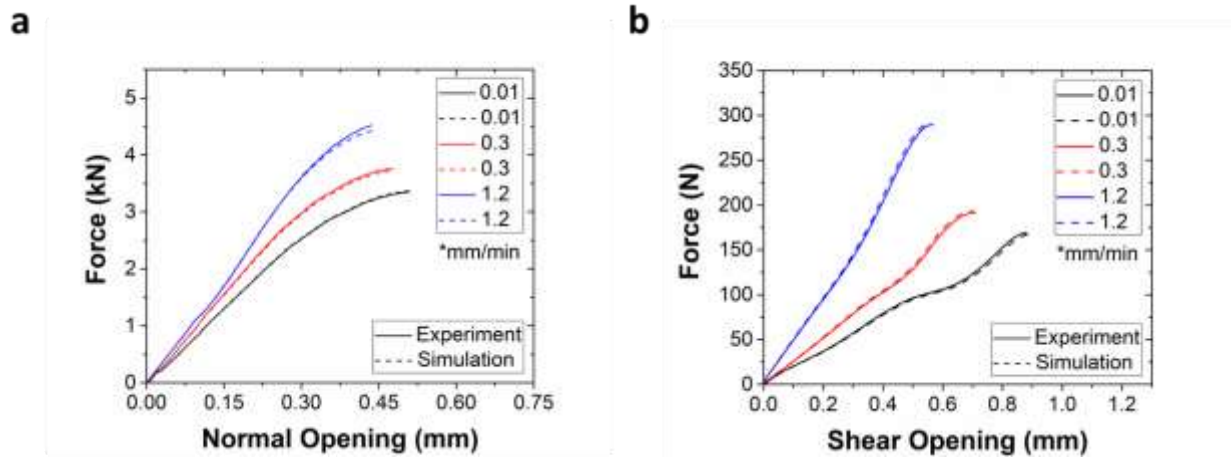

Figure 1.9 (a) Force-extension curves comparison between experiment and simulation for mode 1 fracture and (b) force-extension curves comparison between experiment and simulation for mode 2 fracture.

1.4 Discussion

The traction-separation law for mode I was obtained at loading rates varying from *0.01* to *1.8 mm/min*, while for mode II the loading rates varied from *0.01* to *1.2 mm/min*. The range applied to the mode I fracture experiments was mainly limited by the brittleness of the glass. The Steel backing beams added to the DCB sample could not prevent the high stress concentration developed near the crack tip at higher loading rates. In the case of mode II experiments, the shear strength of the epoxy used to bond the glass substrates to the fixture imposed a limitation in the loading rates used. Lower loading rate values were attempted in order to obtain a traction-separation law that is independent of this parameter.

The traction-separation laws obtained for both modes 1 and 2 portray a same trend. The fracture energy gradually increases with increasing loading rates. The strength (normal and shear) and the stiffness (slope of ascending curve) of the interface also increases at higher loading rates, which led to the increase in fracture energy. The fracture energy dependency on the loading rate may be attributed to the ductile properties of the PVB adhesive as it changes from visco-elastic to glassy behavior at higher loading rates[28.41]. In other words, at low loading rates the energy depends only on the work of adhesion, but at higher loading rates the energy is governed by the work of deformation[42].

As mentioned previously, an unaided eye inspection of both modes 1 and 2 postmortem specimens revealed that the PVB was almost totally stuck to one of the glass substrates leaving the other one apparently clean. This observation was further corroborated by the postmortem sample analysis under the microscope and because any PVB trace could be identified at the apparently clean glass substrate, more expensive analysis such as FTIR or XPS were not pursued. This characterizes an interfacial rather than cohesive type of failure both modes 1 and 2 fracture occurred at the interface between the glass substrate and PVB, characterizing an interfacial type of failure. In fact, cohesive failure strength of an adhesive is usually higher than the polymer-metal interfacial strength[43]. Likewise, the smooth surface of the glass substrates contributes to a lower interfacial strength[44]. Another factor that may contribute to an interfacial failure is due to a surface being excessively basic, since good adhesion bonding usually favors a slightly acidic surface.

There are not many results reported in the literature about the mode 1 fracture toughness of glass laminates. Schupp et al[45] has reported adhesion values between *400* and *900* J/m^2 employing a tapered double cantilever beam fracture specimen. Mode 1 fracture toughness was also evaluated through peel tests. The experiments were conducted at a peel angle of 90^o at loading

rates ranging from *0.01* to *20 mm/min*. Although this type of test provides limited information on the interfacial adhesion when compared to the DCB test aforementioned, it does enable the employment of higher loading rates as the glass substrate, placed at the bottom of the testing apparatus shown in **Figure 1.10**, is not subjected to any loading during the test. In **Table 1.3**, a similar trend is observed (in 90º peel test experiment) regarding the increase of the fracture energy with the loading rate growth, even though the values obtained at lower loading rates differ from the ones derived from the DCB test. This can be explained by the fact that the peel test may not subject the specimen to a pure mode I state as shear and sliding may be involved during the test. Also, the asymmetry in the material properties of both arms could also contribute to a mixed-mode type of fracture[46]. Moreover, it was observed PVB residue in both substrates at loading rates higher than 1.8 mm/min, which suggested that the failure may have transitioned to a cohesive type due to the increase in fracture toughness and strength with the loading rate.

The mode II fracture energy reported in the present paper compares well with the values reported by other researchers. Muralidhar et al, 2000[12] found values between *280* and *930 J/m^2* at a fixed loading rate of 1 mm/s. Sha et al, 1997[47] reported values in the range of *100-300 J/m^2* from experiments conducted *8.47x10^{-3} mm/s*. Jagota et al, 2000[10] found values in the range of *150-600 J/m^2* for loading rates in the rage of *10-5-100 s^{-1}*. Iwasaki et al, 2007[28] reported a fracture toughness ranging from *400* to *800 J/m^2* at loading rates ranging from *1.67x10^{-4} m/s* to *2.96 m/s*. Even though the results presented here are comparable to the ones reported in the literature, it's important to mention that they may vary depending on many factors; including how the laminated glass was fabricated, and the type and/or thickness of PVB used.

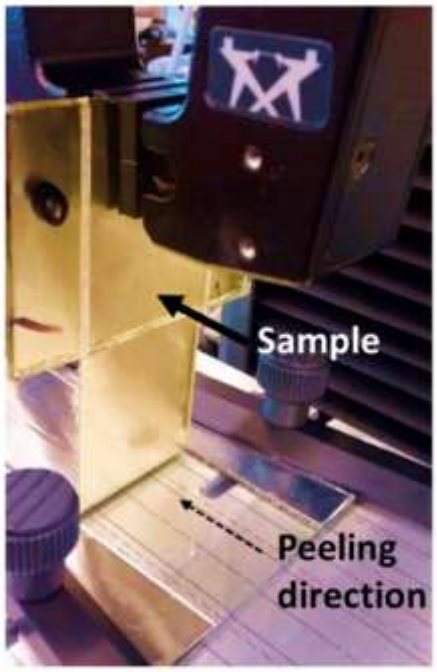

Figure 1.10 (a) Glass-PVB laminate subjected to a peel test.

Table 1.3 Fracture energy values at different peel rates.

Loading rate (mm/min)	Fracture energy, Γ_n (N/m)
0.01	5.6
0.03	15.2
0.1	108.8
0.3	166
0.9	424
1.8	648
2.5	904
5	1200
10	1840
15	2200
20	2320

1.5 Conclusion

The present paper describes the direct extraction of Modes I and II traction-separation laws for the glass-PVB interface at different loading rates. In this way, the Interface could be

characterized in more detail though parameters such as stiffness, normal and shear strength, and fracture energy.

The mode I traction-separation law was achieved by a double cantilever beam test. Chosen by its simple design and ability to provide a pure mode I fracture test, the DCB sample had to have a Steel backing beam attached to it in order to reduce the stress concentration near the crack front in the glass during the test. The fracture energy values obtained in the DCB test compared well with the ones found in peel tests. At the loading rates tested in the DCB tests, the failure occurred at the interface between glass and PVB. However, peels test at higher loading rates revealed the presence of PVB residue in the opposite glass substrates which may characterize a change in failure type from interfacial to cohesive at higher loading rates.

The mode II traction separation law was obtained via a modified ARCAN shear test. This setup was chosen as it's known to reduce the friction between the specimen elements, which in turn would result in a pure mode II fracture test. Fracture energy values compared reasonably with the ones reported in literature. Similarly to what was found in the mode I tests, the failure occurred at the glass-PVB interface.

Finite element simulations coupled with user material subroutines were able to reproduce similar force-displacement response obtained experimentally. The traction-separation laws could be directly input into the model to make it more precise.

In summary, the results obtained in the present work can be utilized in order to predict the failure mode of a given laminated glass under certain conditions.

Supplementary Information (SI)

1.S1 Failure mode prediction

The failure mode of the glass-PVB samples under certain loading conditions was predicted by FEA using Abaqus 6.14. A three-point bending test was modeled in which a cylinder was used to load a rectangular glass-PVB structure (*10 x 5 mm* and *3 mm* thick) at *0.01 mm/min* loading rate. Glass compressive strength was assumed to be *300 MPa* and tensile strength to be *30 MPa*. Modes 1, 2, and 3 were considered for interfacial failure between glass and PVB. The Mode 1 traction-separation law constants were simply taken from the obtained results at a loading rate of *0.01 mm/min*. Modes 2 and 3 traction-separation laws used were bilinear and their constants were considered to be the same and were varied in order to study the effect of each one on the glass-PVB failure mode. The interfacial shear stiffness (K_t), shear strength (σ_t), and fracture energy (Γ_t) were varied to see which failure mode occurs first: glass breakage or interfacial failure. The result is shown in **Figure 1.S1** where the red points in the 3D graph indicate glass brittle failure while the green points correspond to glass-PVB interfacial failure. From the plot, it's possible to conclude that the variable that most affects the failure mode is the shear strength. This behavior is expected as σ_t greatly controls when interfacial damages starts. A high value of σ_t means that the stress necessary to initiate interfacial damage must be high and the glass-PVB interface can be assumed as perfectly bonded as σ_t increases. In this situation, the glass is more likely to fail first. Interfacial stiffness and fracture energy have little influence on the failure mode. Low K_t values tend to increase the possibility of glass brittle failure due to it causes a lower interfacial stress as it's less stiff while high Γ_t values prompt the same behavior as amount of energy necessary to cause interfacial damage is bigger. The results presented by this analysis can serve as guideline to

anyone who wishes to control the damage mode of given structure under certain loading conditions by tailoring its interfacial properties.

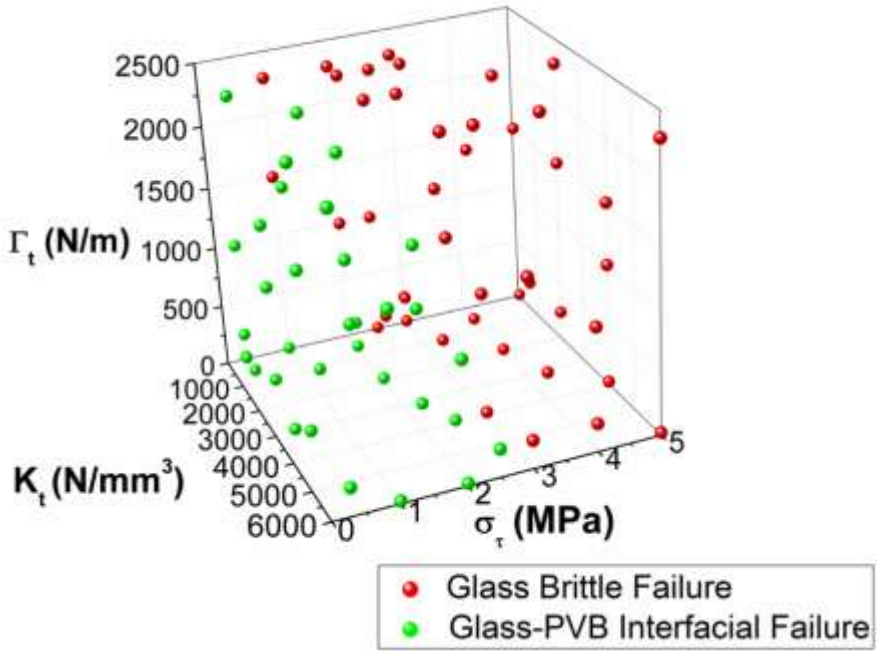

Figure 1.S1 Parametric study of the traction-separation law constants for mode 2 and 3 that was used to predict the failure mode of a glass-PVB structure subjected to a quasi-static three-point bending test.

REFERENCES

1. ASTM C1172 – 14. Standard Specification for Laminated Architectural Flat Glass;

2. Keller, U., & Mortelmans, H., 1999, Adhesion in laminated safety glass–what makes it work. In Glass processing days (Vol. 8, pp. 353-356);

3. Galuppi, L., & Royer-Carfagni, G., 2013, The design of laminated glass under time-dependent loading. Int. J. Mech. Sci., *68*, 67-75;

4. Flocker, F. W., & Dharani, L. R., 1997, Stresses in laminated glass subject to low velocity impact. Eng. Struct., *19*(10), 851-856;

5. Flocker, F. W., & Dharani, L. R., 1998, Low velocity impact resistance of laminated architectural glass. J. Archit. Eng., 4(1), 12-17;

6. Behr, R. A., Karson, M. J., & Minor, J. E., 1991, Reliability analysis of window glass failure pressure data. Struct. Saf., 11(1), 43-58;

7. Du Bois, P. A., Kolling, S., & Fassnacht, W., 2003, Modelling of safety glass for crash simulation. Comput. Mater. Sci., *28*(3-4), 675-683;

8. Timmel, M., Kolling, S., Osterrieder, P., & Du Bois, P. A., 2007, A finite element model for impact simulation with laminated glass. Int. J. Impact Eng., 34(8), 1465-1478;

9. Larcher, M., Solomos, G., Casadei, F., & Gebbeken, N., 2012, Experimental and numerical investigations of laminated glass subjected to blast loading. Int. J. Impact Eng., *39*(1), 42-50;

10. Jagota, A., Bennison, S. J., & Smith, C. A., 2000, Analysis of a compressive shear test for adhesion between elastomeric polymers and rigid substrates. Int. J. Fract., 1*04*(2), 105-130;

11. Li, S., Thouless, M. D., Waas, A. M., Schroeder, J. A., & Zavattieri, P. D., 2005, Use of mode-I cohesive-zone models to describe the fracture of an adhesively-bonded polymer-matrix composite. Compos. Sci. Technol., 65(2), 281-293;

12. Muralidhar, S., Jagota, A., Bennison, S. J., & Saigal, S., 2000, Mechanical behaviour in tension of cracked glass bridged by an elastomeric ligament. Acta Mater., *48*(18-19), 4577-4588;

13. Delincé, D., Sonck, D., Belis, J., Callewaert, D., & Van Impe, R., 2008, Experimental investigation of the local bridging behaviour of the interlayer in broken laminated glass. In International Symposium on the Application of Architectural Glass ISAAG 2008 Conference Proceedings, Munich, October 27-28, 2*008* (pp. 41-49);

14. Bati, S. B., Fagone, M., & Ranocchiai, G., 2009, Analysis of the post-crack behaviour of a laminated glass beam. Glass Performance Days 2009, 349-352;

15. Ferretti, D., Rossi, M., & Royer-Carfagni, G., 2012, Through-cracked-tensile delamination tests with photoelastic measurements. Challenging Glass, 3, 641-652;

16. Butchart, C., & Overend, M., 2012, Delamination in fractured laminated glass. In *engineered transparency international conference at glasstec* (pp. 249-257);

17. Biolzi, L., Cagnacci, E., Orlando, M., Piscitelli, L., & Rosati, G., 2014, Long term response of glass–PVB double-lap joints. Composites Part B, 63, 41-49;

18. Dugdale, D. S., 1960, Yielding of steel sheets containing slits. J. Mech. Phys. Solids, *8*(2), 100-104;

19. Needleman, A., 1987, A continuum model for void nucleation by inclusion debonding. J. Appl. Mech., *54*(3), 525-531;

20. Needleman, A., 1990, An analysis of tensile decohesion along an interface. J. Mech. Phys. Solids, *38*(3), 289-324;

21. Tvergaard, V., & Hutchinson, J. W., 1993, The influence of plasticity on mixed mode interface toughness. J. Mech. Phys. Solids, *41*(6), 1119-1135;

22. Tvergaard, V., & Hutchinson, J. W., 1994, Toughness of an interface along a thin ductile layer joining elastic solids. Philos. Mag. A, 70(4), 641-656;

23. Roe, K. L., & Siegmund, T., 2003, An irreversible cohesive zone model for interface fatigue crack growth simulation. Eng. Fract. Mech., *70*(2), 209-232;

24. Yang, B., Mall, S., & Ravi-Chandar, K., 2001, A cohesive zone model for fatigue crack growth in quasibrittle materials. Int. J. Solids Struct., *38*(22-23), 3927-3944;

25. Li, H., & Chandra, N., 2003, Analysis of crack growth and crack-tip plasticity in ductile materials using cohesive zone models. Int. J. Plast., *19*(6), 849-882;

26. Yang, Q., & Cox, B., 2005, Cohesive models for damage evolution in laminated composites. Int. J. Fract., *133*(2), 107-137;

27. Ji, G., Ouyang, Z., Li, G., Ibekwe, S., & Pang, S. S., 2010, Effects of adhesive thickness on global and local Mode-I interfacial fracture of bonded joints. Int. J. Solids Struct., *47*(18-19), 2445-2458;

28. Iwasaki, R., Sato, C., Latailladeand, J. L., & Viot, P., 2007, Experimental study on the interface fracture toughness of PVB (polyvinyl butyral)/glass at high strain rates. Int. J. Crashworthiness, *12*(3), 293-298;

29. Karac, A., Blackman, B. R. K., Cooper, V., Kinloch, A. J., Sanchez, S. R., Teo, W. S., & Ivankovic, A., 2011, Modelling the fracture behaviour of adhesively-bonded joints as a function of test rate. Eng. Fract. Mech., *78*(6), 973-989;

30. Rosa, A. L., Yu, R. C., Ruiz, G., Saucedo, L., & Sousa, J. L. A. O., 2012, A loading rate dependent cohesive model for concrete fracture. Eng. Fract. Mech., *82*, 195-208;

31. Mello, A. W., & Liechti, K. M., 2006, The effect of self-assembled monolayers on interfacial fracture. J. Appl. Mech., *73*(5), 860-870;

32. Banea, M. D., Da Silva, L. F. M., & Campilho, R. D. S. G., 2011, Mode I fracture toughness of adhesively bonded joints as a function of temperature: experimental and numerical study. Int. J. Adhes Adhes, *31*(5), 273-279;

33. Sorensen, L., Botsis, J., Gmür, T., & Humbert, L., 2008, Bridging tractions in mode I delamination: Measurements and simulations. Compos. Sci. Technol., *68*(12), 2350-2358;

34. Zhu, Y., Liechti, K. M., & Ravi-Chandar, K., 2009, Direct extraction of rate-dependent traction–separation laws for polyurea/steel interfaces. Int. J. Solids Struct., *46*(1), 31-51;

35. Dastjerdi, A. K., Tan, E., & Barthelat, F., 2013, Direct measurement of the cohesive law of adhesives using a rigid double cantilever beam technique. Exp. Mech., *53*(9), 1763-1772;

36. Gowrishankar, S., Mei, H., Liechti, K. M., & Huang, R., 2012, A comparison of direct and iterative methods for determining traction-separation relations. Int. J. Fract., *177*(2), 109-128;

37. Azo Materials, 2001. Retrieved September 29, 2017, from https://www.azom.com/properties.aspx?ArticleID=89

38. Shokrieh, M. M., & Heidari-Rarani, M., 2011, A comparative study for beams on elastic foundation models to analysis of mode-I delamination in DCB specimens. Struct. Eng. Mech., *37*(2), 149-162;

39. Tsai, S., 2018, Introduction to composite materials. Routledge;

40. Banks-Sills, L., & Sherman, D., 1991, J II fracture testing of a plastically deforming material. Int. J. Fract., *50*(1), 15-26;

41. Yamagata, Y., Lu, X., Sekiguchi, Y., & Sato, C., 2017, Experimental investigation of mode I fracture energy of adhesively bonded joints under impact loading conditions. Appl. Adhes. Sci., *5*(1), 7;

42. Benedek, I., 2004, Pressure-sensitive adhesives and applications. CRC Press;

43. Yao, Q., & Qu, J., 2002, Interfacial versus cohesive failure on polymer-metal interfaces in electronic packaging—effects of interface roughness. J. Electron. Packag., *124*(2), 127-134;

44. von Fraunhofer, J. A., 2012, Adhesion and cohesion. Int. J. Dent., *2012*;

45. Schupp, D. A., & Gerberich, W. W., 1991, Effects of film thickness on the work of fracture between adhesives and glass. J. Adhes., *35*(4), 269-283;

46. Padhye, N., Parks, D. M., Slocum, A. H., & Trout, B. L., 2016, Enhancing the performance of the T-peel test for thin and flexible adhered laminates. Rev. Sci. Instrum., 87(8), 085111;

47. Sha, Y., Hui, C. Y., Kramer, E. J., Garrett, P. D., &Knapczyk, J. W., 1997, Analysis of adhesion and interface debonding in laminated safety glass. J. Adhes. Sci. Technol., 11(1), 49-63.

CHAPTER 2 Study of stress transfer between SiNW and PDMS COMPOSITE

2.1 Introduction

In recent years, one-dimensional nanomaterials have received great attention mainly because of their outstanding length-scale dependency on the mechanical properties. One-dimensional structures including nanowires (NWs) have been employed as building blocks in composite materials used in several applications[1-4]. Transparent devices combining excellent electrical performance with high flexibility have relied on metal NWs as an alternative to ITO[5-6]. Based on the increased need for electronic devices to be used in conformity with the human skin, not only flexible but stretchable structures have to be designed. Carbon nanotubes (CNTs) and nanowires are among the materials that have been increasingly used in such structures[7-8] and, especially, Si NWs have been widely explored for stretchable electronics[9-11]. CNTs have been commonly used in nanocomposite structures in order to enhance their mechanical and other multifunctional properties[12-13], while crystalline NWs, known by their exceptional mechanical properties[14], are also being incorporated in highly conductive and stretchable nanocomposite conductors[15]. As nanostructures including NWs can endure a higher level of elastic strain when compared to their bulk counterparts, they are being used to adjust the fundamental properties of semiconductor materials in what is called elastic strain engineering. So far, the methods being used to introduce strain in the NW includes buckling[9] or bending[16] it on a stretchable substrate and stretching[17] a freestanding NW.

The interface mechanics between NWs and substrate play an important role in the performance and reliability of NW-based flexible and stretchable electronics especially when the structure is subjected large deformation. For instance, it was observed the occurrence of interface sliding between Si NWs and PDMS COMPOSITE substrate[9] and that the interfacial sliding could

be suppressed by increasing the static friction (interfacial strength)[18] when applying a surface treatment to PDMS COMPOSITE. Also, the NW buckling shape is greatly influenced by the interface sliding[19-20]. Similarly, when it comes to nanocomposites, it's important to understand the interface mechanics between nanomaterials and matrix. In fact, CNT-based nanocomposites have been extensively investigated with regard to that. The two most common methods to measure the interfacial properties of CNTs and polymer matrix are single pull-out tests[21-25] and fragmentation length measurement[26-29]. In addition, there are other methods used to obtain shear strength and or fracture energy (toughness) between fibers (often microscale) and matrix. For instance, push-out experiments[30-32] have been conducted in order to measure interfacial shear strength of glass fibers and matrix. In this test, the force applied to the individual fiber leads to the complete fracture of the fiber/matrix interface through sliding which results the fiber being pushed out of the matrix. Push-in tests[33-35] are similarly carried out, but in this case the fiber is constrained to the matrix interior. The microbond (microdroplet) test[36-38], which involves pulling a fiber out of a bead, or droplet, of matrix usually through a knife-edge, has been another option to quantify the interfacial fracture properties of fiber-reinforced composites. It'd be possible to adapt these tests to the study of nanowire-matrix interface. Recently, a new approach was developed in which the static friction of SiNWs placed on top of poly-(dimethylsiloxane) (PDMS COMPOSITE) was measured[18] based on "the most-bent state" of the NWs[39]. In this method, the NW is manipulated by AFM and its curvature is measured through images. Then by subsequent derivations, the strain energy and the lateral friction force along the NW can be obtained, respectively. However, this method could present some accuracy problems as it's dependent on the level of discretization of the bent wire. In this respect, it would be interesting to have a model able to capture the present phenomenon with a good accuracy and repeatability.

The experimental methods aforementioned require either the 1D material to be directly loaded or that it breaks in the case of fragmentation measurement. Shear-lag models have been employed to quantify the shear stress transfer between graphene and substrate[40-41]. Such an analysis approach can be extended to NWs and substrate as well. In this paper, we present the study of the interfacial shear stress transfer between a single SiNW and PDMS COMPOSITE in tension using nonlinear and cohesive shear-lag models. The experimental method conducted in AFM, which consists of applying a tensile strain to the PDMS COMPOSITE with Si NWs on its top, has already been successfully employed to analyze the interface interactions between a 2D nanomaterial (monolayer graphene) and an elastomeric substrate (PET)[41]. Different cohesive law models were used to analyze two different cases: untreated PDMS COMPOSITE and 45 min. UVO-treated PDMS COMPOSITE. FEA was used to quantify the interface parameters, mainly interfacial shear strength and fracture energy, by fitting the average strain in the NW from the experiments. Strain distribution on the NW were provided by both FEA and analytical solutions. The cohesive models adopted were also used to study the case when the SiNW is tilted with respect to the direction of applied strain on the PDMS COMPOSITE substrate via parametric study. Moreover, a parametric study was conducted in order to predict the fracture of the SiNWs with different lengths and diameters, which could provide some guideline for future applications of this nanomaterial.

2.2 Experimental setup

For the SiNW/PDMS COMPOSITE stretching experiment, two kinds of PDMS COMPOSITE 10:1 samples fabricated from Sylgard-184 were prepared. One of the samples was kept as it is while the other sample was subjected to a 45 min UVO treatment carried out in a commercial UVO chamber. An array of SiNWs was dispersed on top of both samples so that an

horizontal SiNW could be chosen for each case. In both cases, the SiNW chosen to be analyzed had a diameter of approximately 20 nm. The SiNW on top of the nontreated PDMS COMPOSITE sample had a length of about 22.40 µm while the length of the SiNW that was on top of the UVO-treated sample was about 16.40 µm. The stretching experiments were conducted under AFM microscope where an uniaxial tensile load was applied to PDMS COMPOSITE at a constant strain rate. The average strain on the nanowire was measured in ImageJ with the images obtained from Raman spectroscopy. **Figure 2.1** shows that for the nontreated sample, five different strain levels applied to PDMS COMPOSITE were recorded (from 0 to 20.4%) while for the UVO-treated sample, six different strain levels were recorded (from 0 to 23.5%).

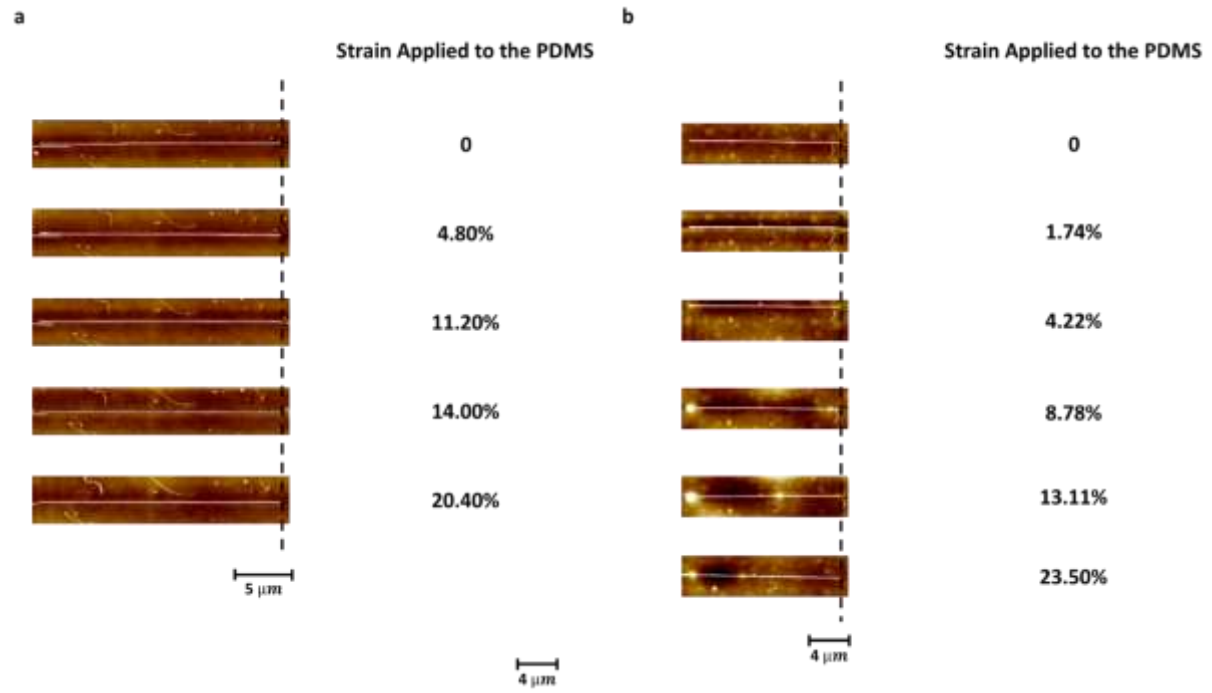

Figure 2.1 SiNW/PDMS COMPOSITE stretching experiments for (a) nontreated PDMS COMPOSITE and (b) 45 min UVO-treated PDMS COMPOSITE.

2.3 Theoretical analysis

2.3.1 Nonlinear shear-lag model

Based on information gathered in experiments, a PDMS COMPOSITE substrate that has not been UVO-treated bonds with the SiNW only through van der Walls interactions. The nonlinear shear-lag analysis was used to study this case. When uniaxial tension is applied to the substrate, the SiNW first deforms concurrently with the substrate due to the interfacial shear stress transfer. Once the interfacial stress reaches a critical value, the SiNW may slide along the interface. Taking advantage of the symmetry of the problem, only half of the NW/substrate system in the horizontal (x) direction is considered. The SiNW has a half-length L in the x-direction with $x = 0$ at the center of the NW. SiNWs with a diameter of 20 nm has a Young's modulus of E_{NW} ($= 120\ GPa$), so its constitutive equation can be given as $\sigma = E_{NW}\varepsilon$, where σ and ε denote the axial stress and strain in the SiNW, respectively.

More details on the derivation of the equations are provided elsewhere[40]. Based on the early shear-lag model developed by Cox[42] for a fiber embedded in a matrix, the equilibrium equation between the axial stress in the SiNW on top of PDMS COMPOSITE and the interfacial shear stress between them can be calculated as follows:

$$\left(\frac{3\sqrt{3}}{2}a^2\right)\sigma_f + (adx)\tau = \left(\frac{3\sqrt{3}}{2}a^2\right)(\sigma_f + d\sigma_f) \quad \textbf{(2.1)}$$

The contact width between SiNW and PDMS COMPOSITE was estimated[43] as the side length of the hexagonal cross section[44-45] of the SiNW. The indentation depth was found to be negligible[46]. Reducing **Equation (2.1)** with respect to dx the following relation is obtained.

$$\frac{d\sigma_f}{dx} = \frac{2\tau}{3\sqrt{3}a} \quad \textbf{(2.2)}$$

where $a = 10\ nm$ is the side length of the SiNW.

Finally, the relation between shear stress with sliding displacement can be found to be

$$\tau = E_{NW}(\lambda)\frac{d^2\delta}{dx^2} \quad \textbf{(2.3)}$$

where $\lambda = \frac{3\sqrt{3}R}{2\pi}$.

As the applied displacement in the first stage is relatively small, the sliding displacement in the entire SiNW is smaller than the critical sliding displacement (δ_i), which characterizes the SiNW/substrate interface as perfectly bonded. Knowing that the shear traction (τ) is linearly related to the sliding displacement (δ) by a stiffness constant (K_0), **Equation (2.3)** yields the following ordinary differential equation:

$$\frac{d^2\sigma}{dx^2} = \frac{K_0}{E_{NW}(\lambda)}\delta \quad \textbf{(2.4)}$$

Applying the pertinent boundary conditions, **Equation 2.4** can be solved and the axial strain in the SiNW is obtained as

$$\varepsilon = \varepsilon_m\left(1 - \frac{\cosh(\beta x)}{\cosh(\beta L)}\right) \quad \textbf{(2.5)}$$

where $\beta = \sqrt{K_0/E_{NW}(\lambda)}$ is the shear-lag parameter.

The maximum shear stress occurs at the ends of the SiNW ($x = \pm L$) with the magnitude

$$\tau_{max} = \beta E_{NW}(\lambda)\varepsilon_m \tanh(\beta L) \quad \textbf{(2.6)}$$

Interface sliding between SiNW and substrate occurs when the maximum interfacial shear stress equals a critical value ($\tau_{max} = \tau_c$). The critical strain for onset of sliding is thus

$$\varepsilon_c = \frac{\tau_c}{\beta E_{NW}(\lambda)}\coth(\beta L) \quad \textbf{(2.7)}$$

When $\varepsilon_m > \varepsilon_c$, the interface consists of a no-sliding zone at the center with two sliding zones emerging from the edges. Let s be the sliding zone size at each end. In the sliding zones ($L > |x| > L - s$), $u_{NW} \neq u_m$ and the interfacial shear stress is assumed to be a constant ($\tau = \pm\tau_c$). By **Equation (2.2)**, the axial force in the SiNW becomes

$$\sigma = \pm\tau_c(x \pm L) \quad \textbf{(2.8)}$$

In the no-sliding zone ($|x| < L - s$), the stresses are

$$\tau = Asinh(\beta x) \quad \textbf{(2.9)}$$

$$\sigma = E_{NW}(\lambda)\varepsilon_m + Acosh(\beta x)/\beta \quad \textbf{(2.10)}$$

The term A can be found by requiring the shear stress to be continuous at $x = \pm(L - s)$. Finally, an equation for the sliding zone size s can be obtained by requiring the axial force in SiNW to be continuous at $x = \pm(L - s)$

$$\coth[\beta(L - s)] + \beta s = \frac{\beta E_{NW}(\lambda)\varepsilon_m}{\tau_c} \quad \textbf{(2.11)}$$

Equation (2.11) can then be applied to calculate the sliding zone size s once $\varepsilon_m > \varepsilon_c$.

Once s is known, the shear stress at the interface and the axial force in the SiNW can be calculated from **Equations (2.9)-(2.10)**. **Figure 2.2(a)** shows the interfacial phases (bonded and damaged) that arise when the nontreated PDMS COMPOSITE is further stretched. The traction-separation law used for this case is also shown.

2.3.2 Integrated cohesive zone model with shear-lag analysis

Cohesive zone models have widely been used in crack initiation and propagation at the interface of many types of bi-materials[47-48]. Although cohesive laws can assume a variety of forms, a typical model takes a similar feature as a bilinear traction-separation relationship[49]. When PDMS COMPOSITE is UVO-treated, chemical bonds are formed between SiNW and the substrate[50]. As an endergonic chemical reaction, these bonds need a certain time to take place and can be permanently broken as the interfacial stress increase which may cause not only sliding but also irreversible interfacial damage. In this case, nonlinear shear-lag analysis combined with cohesive zone modeling was adopted.

Again, further details about the derivation of the equations were published elsewhere[41]. As mentioned before, when the substrate is stretched in the uniaxial direction, the sliding displacement increases between SiNW and substrate. In this analysis, it's assumed that shear stress, after the initial linear increase, will decrease linearly till vanishing according to the bilinear cohesive zone model. Hence, it's possible to characterize three stages of the interface behavior: first part – bonded ($0 < x < L_1$), second part – damaged ($L_1 < x < L_2$), and third part – debonded ($L_2 < x < L$).

The analysis of the first stage when SiNW and substrate are perfectly bonded is identical to the one presented at the nonlinear shear-lag model and calculated by **Equations (2.3)-(2.6)**. As the applied strain increases, sliding starts to occur from the edges of the SiNW dividing the interface into two parts. The axial strain in the bonded part can be obtained as

$$\varepsilon = \varepsilon_m - \delta_i \beta \frac{\cosh(\beta x)}{\sinh(\beta L_1)} \quad \textbf{(2.12)}$$

where here again $\beta = \sqrt{K_0/E_{NW}(\lambda)}$. In the second stage, the sliding displacement exceeds δ_i causing damage at the interface. The axial strain in the damaged part takes the form of

$$\varepsilon = \varepsilon_m + A\alpha \sin\big(\alpha(x - L_1)\big) - B\alpha\cos(\alpha(x - L_1)) \quad \textbf{(2.13)}$$

where $\alpha = \sqrt{\tau_{max}/(E_{NW}(\lambda)(\delta_f - \delta_i))}$.

By applying the pertinent boundary conditions, both the critical value for L_1 (L_{1c}) and the second critical strain ε_{c2} can be determined[41]. Further increase in the applied strain will lead to a debonding of the interface. Both bonded and damaged part have a combined length of L_2. The strain in the bonded part and damage part as well as the lengths L_1 and L_2 can be found according to Guo et al[41]. In the debonded part, the strain in the SiNW becomes zero. **Figure 2.2(b)** shows the interfacial phases (bonded, damaged, and debonded) that arise when the UVO-treated PDMS COMPOSITE is further stretched. The traction-separation law used for this case is also shown.

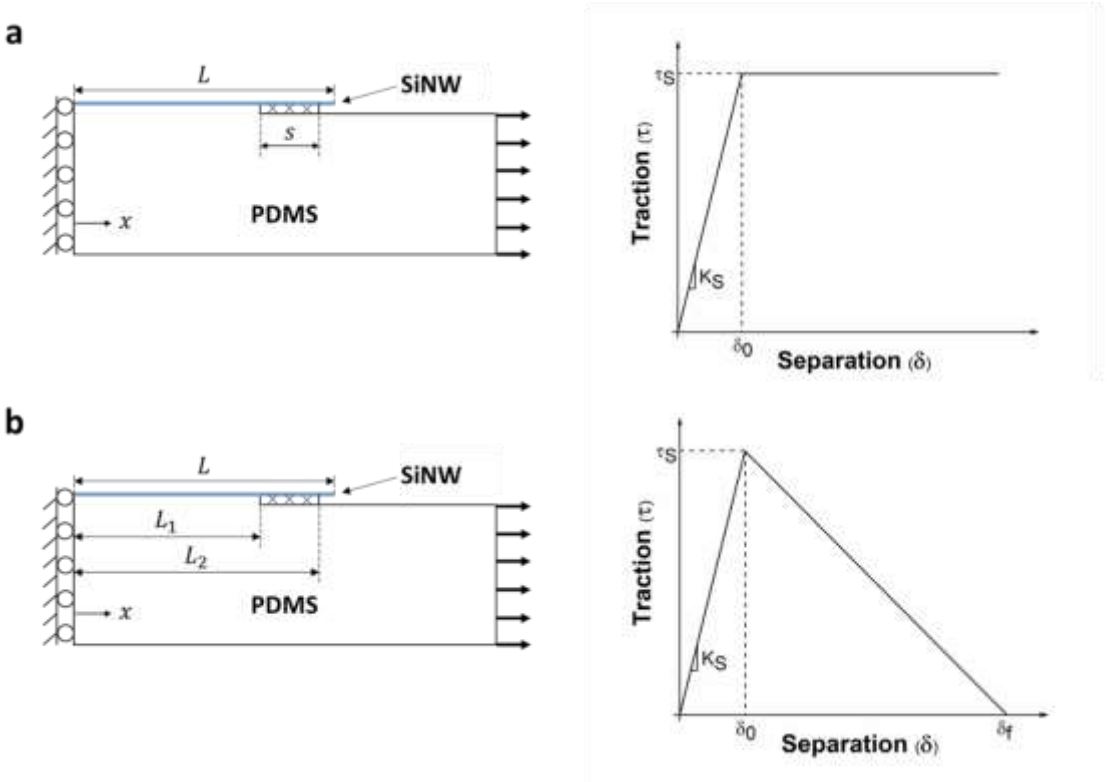

Figure 2.2 SiNW/PDMS COMPOSITE interfacial phases and traction-separation laws for (a) nontreated PDMS COMPOSITE and (b) 45 min UVO treated PDMS COMPOSITE.

2.3.3 Mechanism of NW Alignment

As previously reported, the motion of the SiNW placed on top of the PDMS COMPOSITE substrate under tensile strain can be attributed to geometric compatibility with the substrate and the static friction between NW and substrate[51]. An schematic showing the mechanism of NW alignment is shown in **Figure 2.3**. Assuming a NW with initial length L_0 and skew angle θ_0, the width, height and area of the rectangle bounding the NW are $L_0 sin\theta_0$, $L_0 cos\theta_0$, and $A_0 = L_0^2\, sin\theta_0 cos\theta_0$, respectively. When the strain is released, assuming linear elasticity, the width, height, and area of the rectangle change to $L_0 sin\theta_0/(1+\varepsilon_{pre})$, $L_0 cos\theta_0/(1-\upsilon\varepsilon_{pre})$, and $A_1 = A_0/((1+\varepsilon_{pre})(1-\upsilon\varepsilon_{pre}))$, respectively, where ε_{pre} is the strain and υ is the Poisson's ratio. As a results of the strain release, the NW is expected to slide on top of the PDMS

COMPOSITE as the static friction is not large enough to hold the axial strain. NW sliding may affect differently the strain in the NW depending on which initial angle the NW is placed. Instead of assuming a perfect bond between SiNW and PDMS COMPOSITE, the analysis described previously (nonlinear and cohesive shear-lag analysis) can be employed to model the interface between the two structures. Also, varying interface parameters helps better understand how the model works when the NW is at different angles.

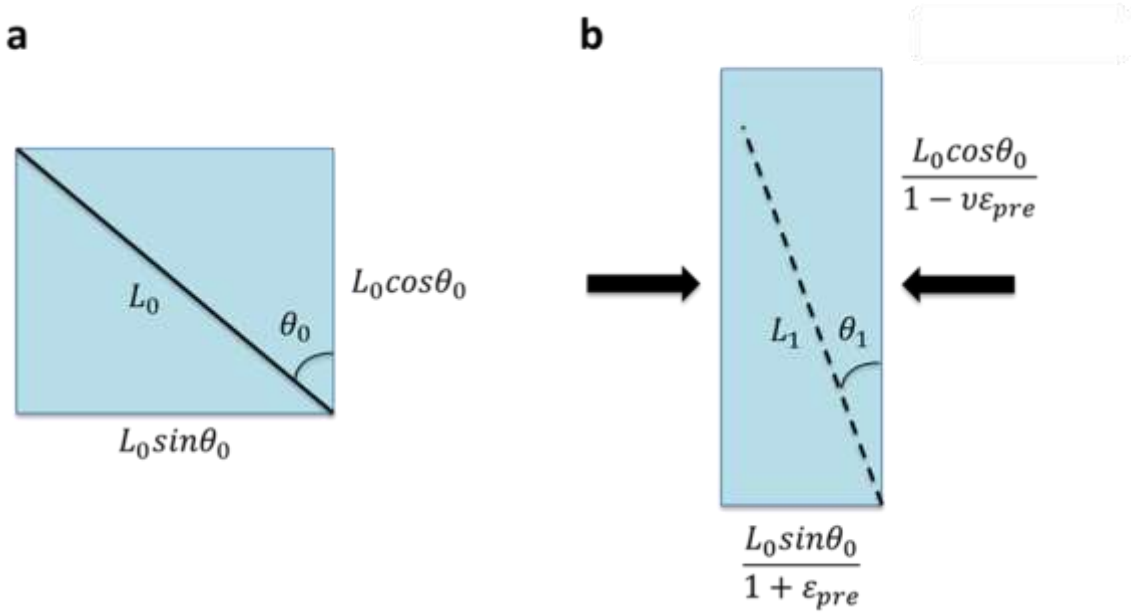

Figure 2.3 Schematics showing the mechanism of NW alignment: (a) a NW transferred to a strained PDMS COMPOSITE with a rectangle of PDMS COMPOSITE bounding the NW; (b) the NW position after release of strained PDMS COMPOSITE, which is analogous to a longitudinal compressive displacement.

2.4 FEA model

The development of a predictable tool is paramount for the assessment of the interface properties between 1D materials and elastomeric substrates. A 3D finite element analysis performed in Abaqus 6.14 was used in order to calculate the strain transferred to the SiNW placed on top of PDMS COMPOSITE and aligned to its stretching direction. The FE model for both cases,

PDMS COMPOSITE with and without UVO treatment, was carried out in a similar way. Only half of the PDMS COMPOSITE/SiNW system was considered by taking advantage of the symmetry of the problem in the horizontal direction as can be seen in **Figure 2.2**. The SiNW was modeled with hexagonal cross-section[44-45] and having one of its faces in contact with PDMS COMPOSITE. C3D8R reduced linear brick elements were used to model PDMS COMPOSITE and SiNW. It was adopted an isotropic linear elastic material behavior for both structures. Young's modulus of *120 GPa* and Poisson ratio of *0.3* was used for the SiNW[44]. For the PDMS COMPOSITE substrate, it was assigned a Young's modulus of *2 MPa* and a Poisson ratio of *0.48*[52]. To be consistent, the SiNW dimensions were chosen to be the same as in the experiments. The diameter of the SiNW for both cases was set as *20 nm*. The nontreated SiNW length used was *22.40 μm* while the UVO treated had a length of *16.40 μm*. The interfacial shear stress is responsible for transferring the effect of uniaxial loading applied to the PDMS COMPOSITE substrate to the SiNW and with the model developed, it's possible to evaluate the mode II fracture toughness and the strain distribution along the SiNW. The interface between SiNW and PDMS COMPOSITE was modeled using cohesive contact properties given in terms of a bilinear traction-separation law, which parameters were obtained through comparison with experiment results.

Two forms of simple bilinear cohesive zone modeling were employed in this study as shown in Figure 1. In both cases, the traction first increases linearly with a constant stiffness K_0 up to the point when it reaches its maximum value τ_{max}. The plot seen in **Figure 2.2(a)** represents the traction-separation law at the interface between a pure PDMS COMPOSITE (nontreated) and SiNW taking into consideration the assumption that after τ_{max} is achieved, NW sliding occurs but without debonding as the van der Waals force still acts at the interface after this point assuring a constant traction. On the other hand, the plot in **Figure 2.2(b)** represents the traction-separation

law between an UVO-treated PDMS COMPOSITE and SiNW as can be seen by the linear decrease in traction to zero after its maximum value due to the irreversible breaking of some of the interfacial chemical bonds. In this case, not only the shear strength τ_{max} but also the fracture toughness G_C, which is given by the area under the traction-separation plot, must be obtained. Eventually both, the SiNW average strain and the strain distribution along the SiNW obtained by FEA were compared to experimental and analytical results, respectively.

In order to study the effect of the interface properties for SiNW at different angles, a 3D finite element analysis using the same software was employed. The schematic of the model was shown in **Figure 2.3**. The SiNW was placed on top of the PDMS COMPOSITE substrate at several different angles with respect to the PDMS COMPOSITE stretching direction while a compressive strain was applied in the transverse direction resulting in *80%* substrate stretch in the longitudinal direction. The angles studied varied from *0* to *90°* equally spaced by *5°*. C3D8R brick elements were used to model PDMS COMPOSITE and SiNW. The material properties adopted for PDMS COMPOSITE and SiNW were the same as for the previous model. The diameter of the SiNW was *20 nm* while the length was *10 μm*. Similarly, the interface between SiNW and PDMS COMPOSITE was modeled using cohesive contact properties given in terms of a bilinear traction-separation law. Both laws described previously were tested and its respective parameters were varied in order to study its effect.

2.5 Results and discussion

Traction-separation laws with different shapes and parameters have been used to evaluate the response of several interface systems[53]. For nontreated PDMS COMPOSITE, the traction-separation law chosen (**Figure 2.2(a)**) shows that the traction does not drop after the cohesive element yields when it reaches the interfacial shear strength (τ_s). The shape of the curve is similar

to the simple Coulomb friction law applied by Snozzi and Molinari[54] and recently by Nian et al[55] for fiber-reinforced composites.

When it comes to the traction-separation law used for the case of UVO-treated PDMS COMPOSITE (**Figure 2.2(b)**), it's possible to see that although the shear strength value is higher than nontreated PDMS COMPOSITE case because of the strong nature of the chemical reactions, the traction decreases as it passes that point. This bilinear model of traction-separation law was first presented by Geubelle and Baylor[56] and applied in the study of delamination in composites cause by impact. This relationship is already implemented in Abaqus. For the chemical bonding type of interface, there have been studies showing softening at the traction-separation laws obtained through interfacial shear tests or molecular dynamics (MD) shear simulations.

MD simulations have been widely used in order to obtain the traction-separation law for a range of different interfaces. Dandekar et al[57] used this method to describe the Al-SiC interface mechanics. This type of material, which is called metal matrix composite material, is characterized by the formation of a chemical bond between the reinforcement and molten metal. Chemical bonding occurs when the atoms of matrix and reinforcement are in direct contact and is accomplished by exchange of electrons. This type of bonding can be metallic, ionic or covalent[57,58]. Rahman and Haque[59] characterized the interface between crosslinked graphene and epoxy through molecular mechanics and molecular dynamics simulations. The research shows a considerable increase in the interfacial strength by chemical bonding.

Li and Seidel[60] obtained a shear traction-separation law between graphene sheet and polyethylene through MD simulations. The cohesive law takes into account the chemical effect of the covalent bonds. You et al[61] employed fiber push-put tests to study the interface between Silicon carbide and Copper matrix. The traction separation law derived from the fitted damage evolution

curve for the chemically bonded interface clearly shows a softening region after the traction strength is reached. Bianchi and Zhang[62] developed a cohesive zone model to describe the shear delamination resistance of z-pin reinforcements in a double cantilever beam sample. The cohesion between the z-pins and the DCB matrix is due to interfacial chemical bonding.

The results related to the stretching of a SiNW on top of an nontreated and an UVO-treated PDMS COMPOSITE sample will be presented and discussed. As previously mentioned, the average strain on the nanowire was measured using images obtained from Raman spectroscopy at different stages of the experiment. The problem was modeled by FE in order to find the interface parameters for each case. One way to validate the values found for the parameters was to compare the average strain found by FE with the experiment strain values. As a result, the interface parameters could be derived for both cases, nontreated and UVO-treated PDMS COMPOSITE. **Figure 2.4(a)** shows the comparison of the SiNW average strain between simulation and experiment for the nontreated PDMS COMPOSITE. Initially, the strain in SiNW increases, but as the applied strain at the PDMS COMPOSITE reaches about *13%*, the SiNW strain reaches a plateau. It's known that when the applied strain increases the shear stress at the SiNW ends tends to decrease and damage tends to gradually initiate at the location[40-41]. As the applied strain in PDMS COMPOSITE further increases, there is no decrease in SiNW strain which also justifies the use of the traction-separation law shown in **Figure 2.2(a)** as the best suited to fit the experimental data where the interfacial stress was set to a constant value after the shear strength level is achieved. These results confirm that the bonding between SiNW and nontreated PDMS COMPOSITE is of physical nature. Most physical forces tend to originate from electrostatic interactions between dipole molecules. However, there is another type of van der Waals force referred most commonly as dispersion force that acts between neutral atoms and molecules,

without the necessity of them being charged. Even though a non-polar atom has a zero average dipole moment, the constant movement of the electrons around its nuclear protons may create an instantaneous dipole moment. This instantaneous dipole generates an electric field that polarizes any nearby atom, inducing a dipole moment in it. The interaction between the two dipoles gives rise to an instantaneous attractive force between the two atoms. Dispersion forces are relatively weak and depends only on the distance between the atoms to occur[63].

Figure 2.4(b) shows the comparison of the SiNW average strain for the UVO-treated PDMS COMPOSITE. Like the first case, the SiNW strain increases up to a peak value, which is about at *10%* applied at the PDMS COMPOSITE. After this point, it's possible to see a decrease in SiNW strain after a certain strain level is applied to the UVO-treated PDMS COMPOSITE which corresponds to the point when the shear strength value is achieved. When PDMS COMPOSITE is UVO-treated, covalent chemical bonds such as siloxane bonds *(-Si-O-Si-)* are formed through condensation reactions at the interface between SiNW and PDMS COMPOSITE. These bonds are known to be stronger than van der Waals forces, which explains the higher SiNW average strains obtained when the PDMS COMPOSITE is UVO-treated. In this type of reaction, two molecules combine to form a single molecule with the loss of a small molecule[50]. Condensation reactions are also endergonic, which means they require energy to be driven[64,65]. They are chemical reactions in which the standard change in free energy is positive, and energy is absorbed. In other words, an energetic barrier has to be overcome in order for these chemical reactions to take place and, for that reason, once the bonds are broken it takes time for them to re-form resulting in a decrease in SiNW strain once damage at the interface continues to progress due to an increase in applied strain on PDMS COMPOSITE. The traction-separation law used in this case (**Figure 2.2(b)**) was also suitable to fit the strain results.

Based on the SiNW average strains, interface parameters were found for each case. **Tables 2.1** and **2.2** show the interface parameters that best fit the experimental results for the nontreated and UVO-treated PDMS COMPOSITE, respectively. The FEA results agreed very well with the analytical case when it's assumed that only one side of the SiNW touches the substrate. The interface stiffness value for the UVO-treated PDMS COMPOSITE is higher when compared to the nontreated as the static friction increases due to hydrophobic-to-hydrophilic conversion of the PDMS COMPOSITE surface under UVO treatment[18]. As discussed before, the UVO-treated PDMS COMPOSITE also presented a higher shear strength value due to the stronger nature of the chemical bonding that takes place between SiNW and PDMS COMPOSITE[18].

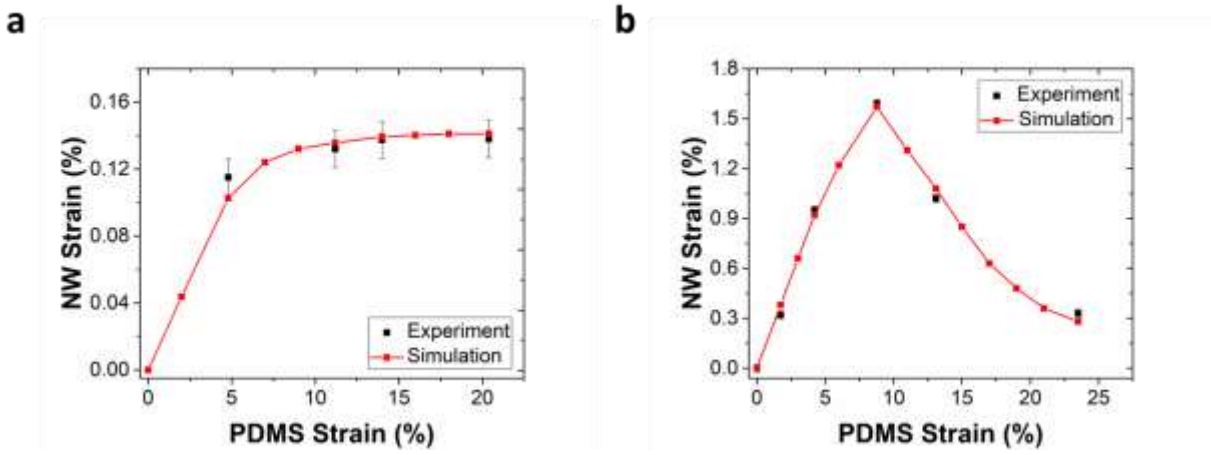

Figure 2.4 Comparison between experiment and FEA results of the average SiNW strain versus the applied PDMS COMPOSITE strain for (a) nontreated PDMS COMPOSITE and (b) 45 min UVO-treated PDMS COMPOSITE.

Table 2.1 Interfacial property values found from the analytical solution and FEA for the nontreated PDMS COMPOSITE.

	Analytical	Simulation
K_S (TPa/m)	1.7	1.7
τ_S (MPa)	0.8	0.8

Table 2.2 Interfacial property values found from the analytical solution and FEA for the 45 min UVO-treated PDMS COMPOSITE.

	Analytical	Simulation
K_S (TPa/m)	41	41
τ_S (MPa)	16	16
G_S (N/m)	7.8	7.8

Because there is no experiment information on local strain distribution along the SiNW length, it was assumed that it should have a characteristic shape based on the classic shear-lag analysis[40]. **Figure 2.5** shows the strain distribution comparison between FEA and the analytical solution which derivation was previously presented and implemented in MATLAB. The parabolic distribution seen is a result of the cohesive zone model adopted. **Figure 2.5(a)** shows the results for the nontreated UVO sample. In **Figure 2.5(b)**,which shows the strain distribution for the UVO-treated case, it's possible to see a decrease in the SiNW strain as a result of the interface damage. Also, when the applied strain in the PDMS COMPOSITE is *23.5%*, the strain distribution is flat at the edges. This result suggests that interface debonding may have already started to occur at both edges of the SiNW and, for that reason, the strain in that region is zero. **Figure 2.5** also helps corroborate the FEA model used since both, analytical and simulation results, agreed very well.

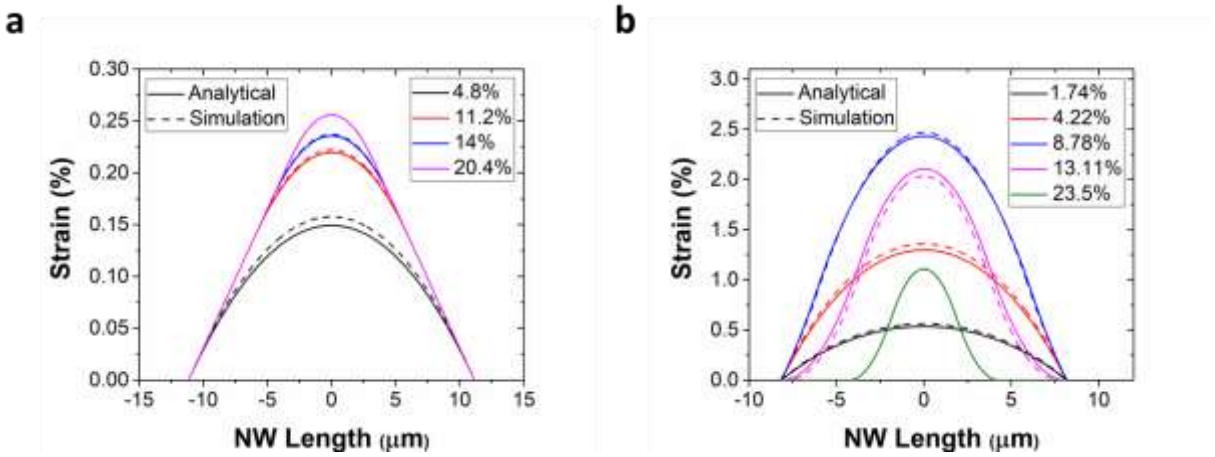

Figure 2.5 Comparison between analytical and FEA results of the SiNW strain distribution along its length for (a) nontreated PDMS COMPOSITE and (b) 45 min UVO-treated PDMS COMPOSITE.

Next, the alignment simulation results are presented and discussed. **Figure 2.6** shows the prediction of the new skew angles for the SiNWs with respect to their previous configuration when the PDMS COMPOSITE substrate is compressed by *80%*. It was already demonstrated how the experiment results compared very well with the nonlinear elastic analysis results[51]. The simulation results obtained for the new skew angles, which were also in good agreement with the other results, were independent of the interface parameters chosen. In other words, the simulation shows that the skew angle change can be attributed to the geometric compatibility with PDMS COMPOSITE, rather than the static friction between SiNW and PDMS COMPOSITE. Nevertheless, the average strain in the SiNW can be affected by this same static friction. From the FEA model, it was observed that only Mode II interface properties influence in the SiNW final length. In order to investigate how these parameters control SiNW stretching when it's tilted at different angles ranging from *0°* to *90°*, the two types of bilinear cohesive laws already presented in **Figure 2.2** were adopted. For each case, the interface stiffness and shear strength were varied for a wide range of values. For the second bilinear curve, the fracture energy was varied as well.

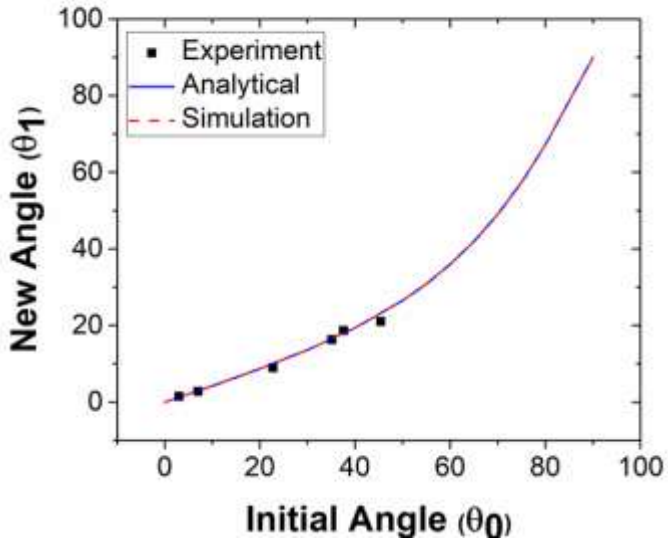

Figure 2.6 FEA and experimental results relating the new skew angle to the initial skew angle after release of a strain of 80% in PDMS COMPOSITE.

Figure 2.7 shows the first bilinear cohesive law adopted and the strain results related to the initial SiNW skew angle. A SiNW tilted at an angle ranging from *0* to *45°* with respect to the transverse direction experience tension, while at angles from *45°* to *90°* it experiences compression. **Figure 2.7(b)** shows the SiNW strain variation with the change in interface stiffness. For this particular study, the shear strength was kept at a constant value ($\tau_S = 0.8\,MPa$). First of all, it's clearly noticeable an increase in strain for all angles when the stiffness increases from *0.17* to *1.7 TPa/m*. This is caused by the increase in the static friction between SiNW and PDMS COMPOSITE. There is not much increase in strain when the stiffness increases from *1.7* to *17 TPa/m*, but there are some differences nevertheless. First analyzing the SiNW in tension, It'd be expected that SiNWs placed at angles from *0* to about *25°* had a higher strain when compared to SiNWs at angles from *30°* to *45°* because they are more aligned to the transverse direction where tensile strain should be higher. However, due to the same higher strain the interface damage is also higher and, for that reason, the SiNW strain is smaller for NWs placed at an angle from *0* to about

25°. The same logic can be applied when analyzing the compression part of the plot. SiNWs tilted at angles from *45°* to *70°* experience a higher compressive strain despite the fact that SiNWs tilted at angles ranging from *70°* to *90°* are more aligned to the longitudinal direction where the compressive strain is higher. **Figure 2.7(c)** shows the SiNW strain variation with the change in shear strength. In this case, the interface stiffness was kept at a constant value of *1.7 TPa/m*. When the shear strength is set to *0.08 MPa*, the SiNW is very small for all angels studied. That's simply due to the fact that interface damage is much more prone to occur when a lower maximum stress value is set. When the shear strength increases from *0.8* to *8 MPa*, there are some differences that need to be pointed out. First looking at the SiNW in tension, the plot shows an increase in strain for angles between *0* and *30°* with the increase in shear strength. As previously discussed, a SiNW tilted at an angle in between those will be subjected to a higher tensile stress. However, interface damage is retarded or prevented by the increase in shear strength. Similar behavior is experienced by a SiNW in compression when it's tilted at angles between *70°* and *90°*. Analogous study was carried out using the other bilinear cohesive law. The results shown in **Figure 2.9** are in very close proximity to the ones previously presented. **Figure 2.8(b)** shows a small decrease in strain when the interface stiffness is *17 TPa/m* for angles between *0* and *25°* and between *70°* and *90°* when compared to the previous results using the first cohesive law. **Figure 2.8(d)** shows that the variation of SiNW strain by changing the interface fracture energy and keeping the other parameters constant ($K_S = 41\ TPa/m$ and $\tau_S = 16\ MPa$) is relatively small as it only affects the SiNW strain after the damage has initiated. The simulation results indicate that for the same applied strain at the PDMS COMPOSITE substrate, the shape of the bilinear cohesive law does not influence considerably the strain in the SiNW tilted at different angles.

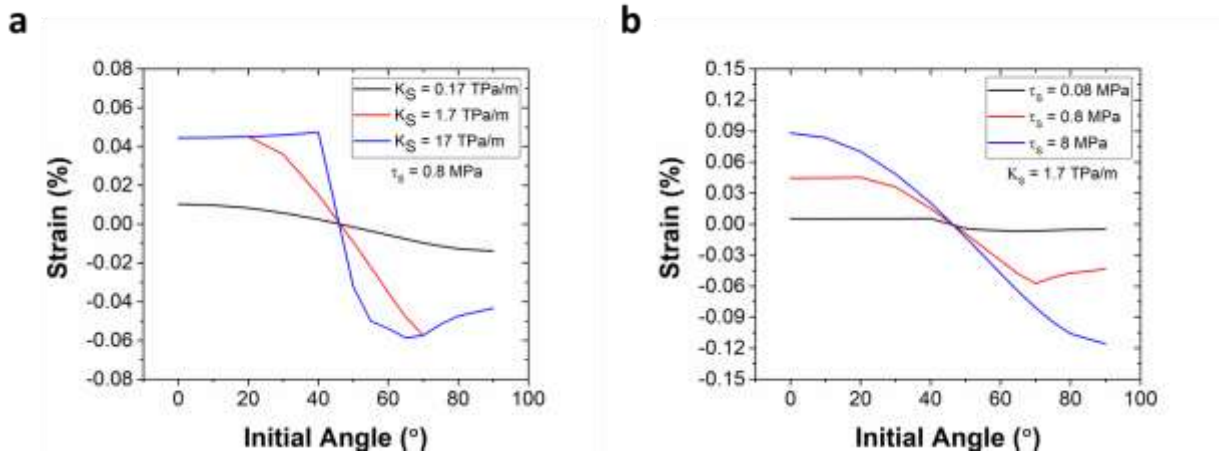

Figure 2.7 SiNW average strain dependence on (a) shear stiffness and (b) shear strength using the bilinear cohesive law in Figure 2(a).

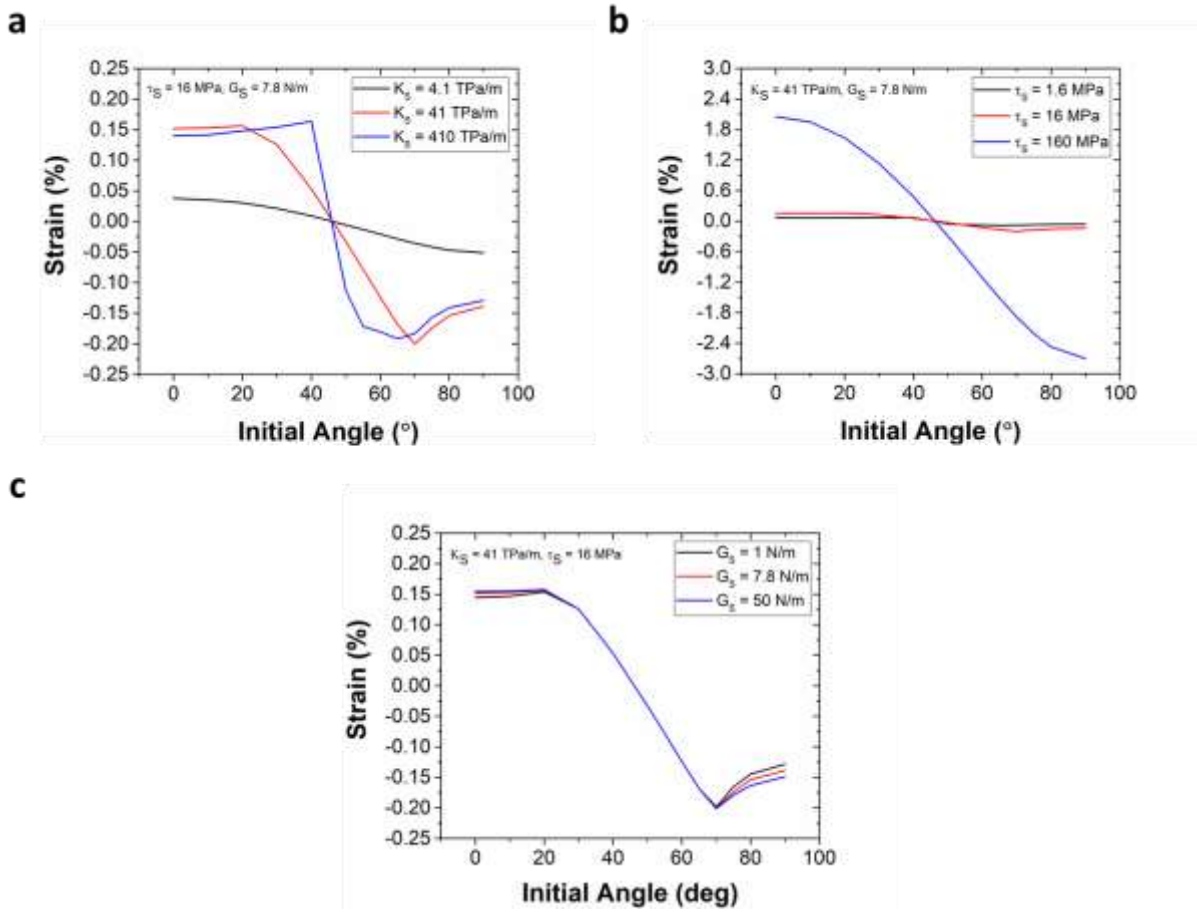

Figure 2.8 SiNW average strain dependence on (a) shear stiffness, (b) shear strength, and (c) shear fracture energy using the bilinear cohesive law in Figure 2(b).

Parametric studies were also conducted to investigate the possible fracture of SiNWs by the stress transfer mechanism highlighted on this paper when the PDMS COMPOSITE is stretched up to *50%*. In this study, it was used the traction-separation laws shown in **Figure 2.2** for both, nontreated and UVO-treated PDMS COMPOSITE, with the parameters found and shown in **Tables 2.1** and **2.2**. First, the a *15 μm* long SiNW was chosen and its diameter was varied to *10* to *60 nm*. Then, a SiNW with a diameter of *20 nm* was taken and its length was varied from *1 μm* to *25 μm*. **Figure 2.9** shows the results for the nontreated PDMS COMPOSITE, and **Figure 2.10** for the UVO-treated PDMS COMPOSITE. The plots are composed by the maximum strain found in SiNW at given strain applied to the PDMS COMPOSITE, which according to shear-lag theory it's in the middle of the SiNW[40]. By comparing these results with the SiNW fracture strain values found by tensile test in situ inside a scanning electron microscope[44], it's found that the SiNW will not fracture regardless of its diameter and length for the range of strain applied to both, nontreated and UVO-treated PDMS COMPOSITE. This means that there is more room for testing this NWs using the discussed testing setup before they break and suggests that these 1D nanostructures reliably used in applications that require a large substrate stretchability with little or no fracture present in the percolating network[66].

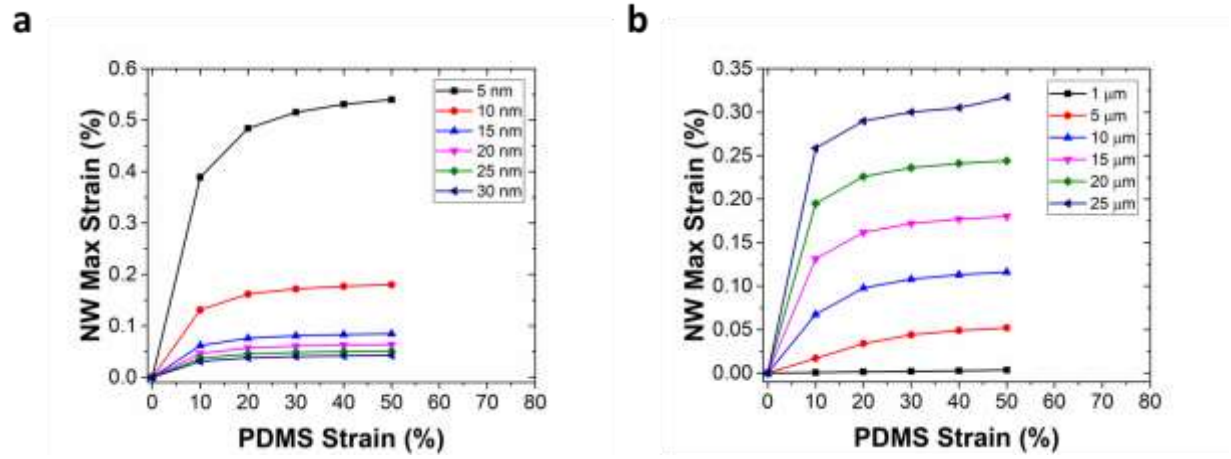

Figure 2.9 SiNW maximum strain variation on top of nontreated PDMS COMPOSITE for a range of (a) SiNW diameters (L=15 μm) and (b) SiNW lengths (D=20 nm).

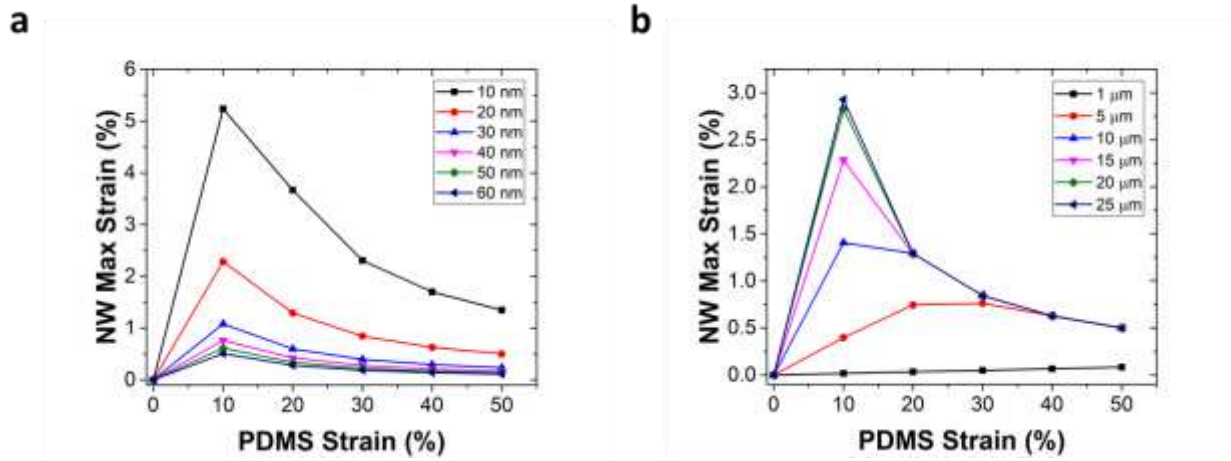

Figure 2.10 SiNW maximum strain variation on top of 45 min UVO-treated PDMS COMPOSITE for a range of (a) SiNW diameters ($L = 15$ μm) and (b) SiNW lengths ($D = 20\ nm$).

2.6 Conclusion

The interfacial shear stress transfer between a single SiNW and PDMS COMPOSITE was investigated. Two types of PDMS COMPOSITE substrates were used: nontreated and UVO-treated for *45 minutes*. The type of interaction that occurs at the interface between SiNW and nontreated PDMS COMPOSITE is composed basically by van der Walls forces, or more specifically, dispersion forces. These physical forces are weak in nature in tend to form

instantaneously. Non-linear shear lag model was used to study this type of interface. By fitting the experimental data, the interface stiffness and shear strength were found to be, $K_s = 1.7\ TPa/m$ and $\tau_S = 0.8\ MPa$, respectively. In contrast, the interactions that occur between the SiNW and UVO-treated PDMS COMPOSITE are condensation reactions. This chemical-type bond is known to be relatively stronger, although it needs time to take place as the reaction energy barriers has to be overcome. This type of interface was better modeled by an integrated cohesive zone model with shear-lag analysis. Similarly, the experimental data was fitted and the interface stiffness, shear strength, and mode II fracture toughness were identified with the values of $K_s = 41\ TPa/m$, $\tau_S = 16\ MPa$, and $G_S = 7.8\ N/m$, respectively. The traction-separation laws used to model the interfaces in the previous cases were used to study the strain when a SiNW is on top of PDMS COMPOSITE, but tilted with respect to the applied strain on the substrate. Several angle configurations were modeled and a parametric study was performed by varying the interface parameters. It was found that SiNW tiled at angles between 0° and 30° and between 70° and 90° with respect to the transverse direction is more affected by the parameter variation. Both traction-separation laws rendered very close results for the range of parameters studied. These results may serve as a guideline on how the interface properties may affect the alignment of NWs placed on top of a substrate which contributed to a better understanding on the assembly of such devices. Also, parametric studies were conducted to predict SiNW fracture of different lengths and diameters. By comparison with the SiNW fracture strain values found by tensile test in situ inside a scanning electron microscope, it was found that for the strain applied to PDMS COMPOSITE (up to *50%*), the SiNW does not break for the range of lengths and diameters studied. These results suggest that SiNWs could be reliably used in applications in which the substrate is largely stretched without fracturing the NWs that are part of the percolation network. Overall, the study reported as

well the results found contribute to a better understanding of the mechanics behind the shear interaction between 1D nanomaterials and elastomeric substrates. The analytical and FEA models can be extended in future work to study other configurations, such as embedded NWs and buckling conditions, as well as other types of 1D nanostructures and substrates.

Supplementary Information (SI)

2.S1 Adhesion tests

A simple experiment was devised in order to provide further evidence of the difference in interface behavior that nontreated and UVO-treated PDMS COMPOSITE substrates may present. First, PDMS COMPOSITE 10:1 samples fabricated from Sylgard-184 having about $1\ cm^2$ size were prepared and placed on a glass substrate. One of the samples was kept on a petri dish, protected from the environment, while the other sample was subjected to a *20 min* UVO treatment carried out in a commercial UVO chamber. The samples were tested in the Delaminator v8.2 adhesion test system as **Figure 2.S1** shows. The samples had their glass substrates glued to the fixed clamp while a $1\ cm^2$ piece of silicon wafer was glued to the movable clamp. Eventually, both clamps were brought together as fast as possible to avoid environment contamination. The experiment consisted in pulling the silicon wafer apart from the PDMS COMPOSITE samples at a constant rate of $0.1\ mm/s$ and at different intervals of time. **Figure 2.S2(a)** shows the results for an nontreated PDMS COMPOSITE sample. The first pulling was done right after the two parts made contact ($\sim 2\ sec$) and it shows that the force recorded was about *0.045 N*. For the second pulling, the samples were brought back together again and they were pulled apart after a wait time of $1\ min$. This process was repeated with different wait times as depicted in the figure legend. The same level of force was achieved by each subsequent pulling. This means that the adhesion between PDMS COMPOSITE and silicon is time-independent and happens just by the contact of

the two parts. This behavior is characteristic of dispersion forces, which are physical in nature. Two UVO-treated samples were tested with the same methodology. **Figure 2.S2(b)** shows that the first pulling occurred 2 min after the two part made contact. The peak force recorded for this case was about 7 N, which is much higher compared to the nontreated sample. However, the peak force seems to decrease with subsequent pulling which indicates that the some of the chemical bonds formed during first contact may be broken off as the experiment goes on. Also, it's interesting to note that when the contact is allowed minimum time to take place ($\sim 2\ sec$), the force recorded is almost negligible. This is corroborated by the second test shown in **Figure 2.S2(c)**, when the first pulling was carried out almost immediately after contact ($\sim 2\ sec$). These results suggest that the bonding between silicon and an UVO-treated PDMS COMPOSITE sample although stronger need some time to form. In other words, the adhesion may be dictated by a chemical reaction, and as common to any other reaction of this nature, an energy barrier has to be overcome in order for it to take place.

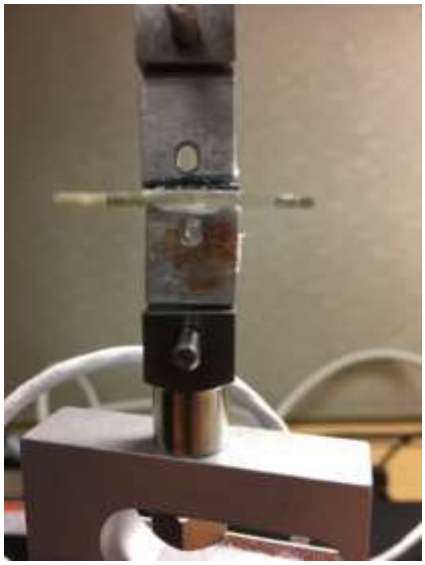

Figure 2.S1 Sample mounted in the Delaminator v8.2 Adhesion Test System.

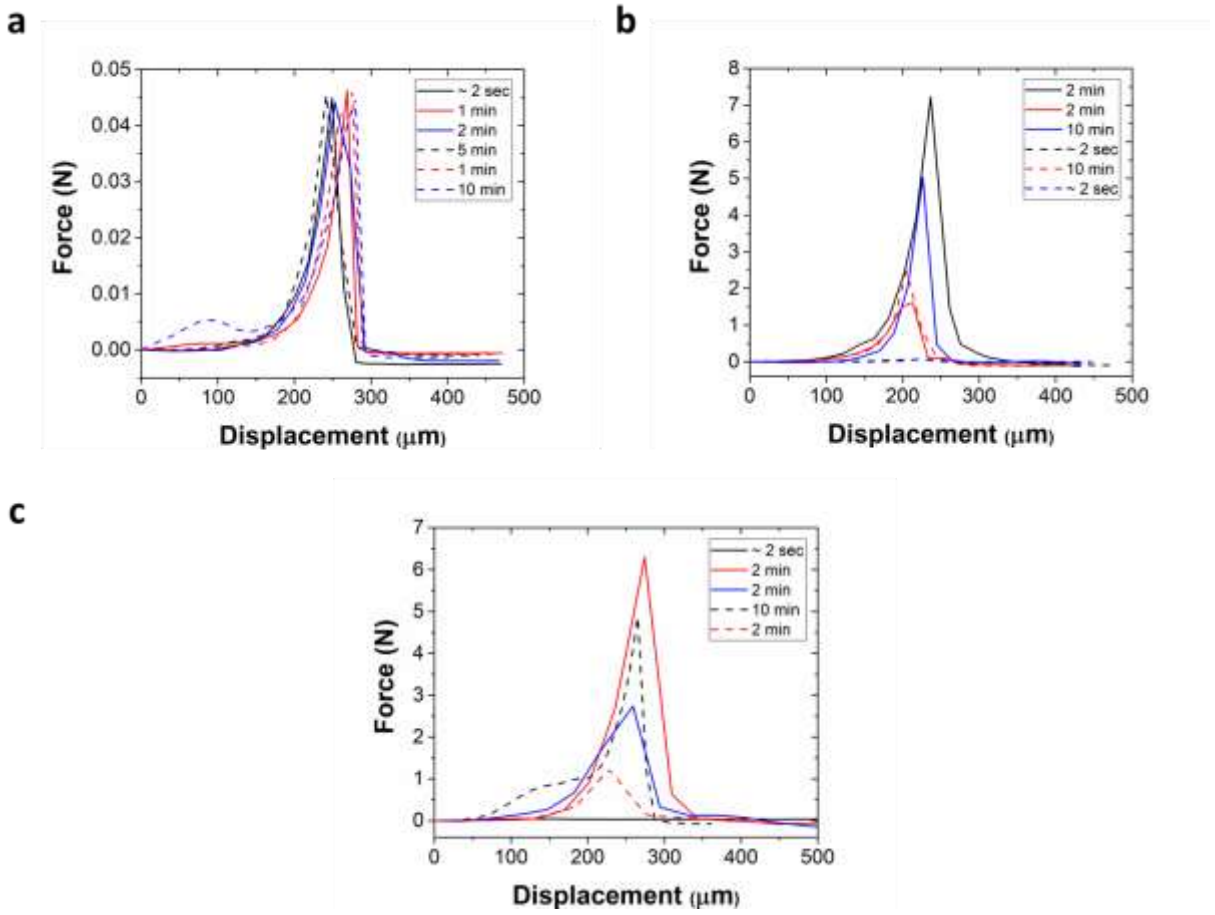

Figure 2.S2 Adhesion force recorded for (a) nontreated PDMS COMPOSITE sample and (b-c) two different 20 min UVO-treated PDMS COMPOSITE samples.

2.S2 FEA parametric study

An attempt was made to use the traction-separation law showed in **Figure 2.4(b)**, which was applied to the case where the PDMS COMPOSITE is UVO-treated, to fit the experimental data obtained with the nontreated PDMS COMPOSITE sample showed in **Figure 2.5(a)**. Different interface parameters were chosen in the FEA model and the results presented in **Figure 2.S3** shows that a reasonable correlation can be attained but only for higher values of fracture energy G_S. However, high values of G_S are more characteristic of an UVO—treated interface. It's also possible to notice that the higher values of SiNW strain don't reach a plateau like the experiment results.

Interface stiffness K_S could be varied, but it would make hard to fit the lower values of SiNW strain with the experiment results. **Figure 2.S4** shows the attempt to fit the experimental data from the UVO-treated PDMS COMPOSITE sample (**Figure 2.5(b)**) with the traction-separation law showed in **Figure 2.4(a)**. It's clear that a good correlation could not be attained. These results reinforce the fact that both interfaces must be analyzed differently.

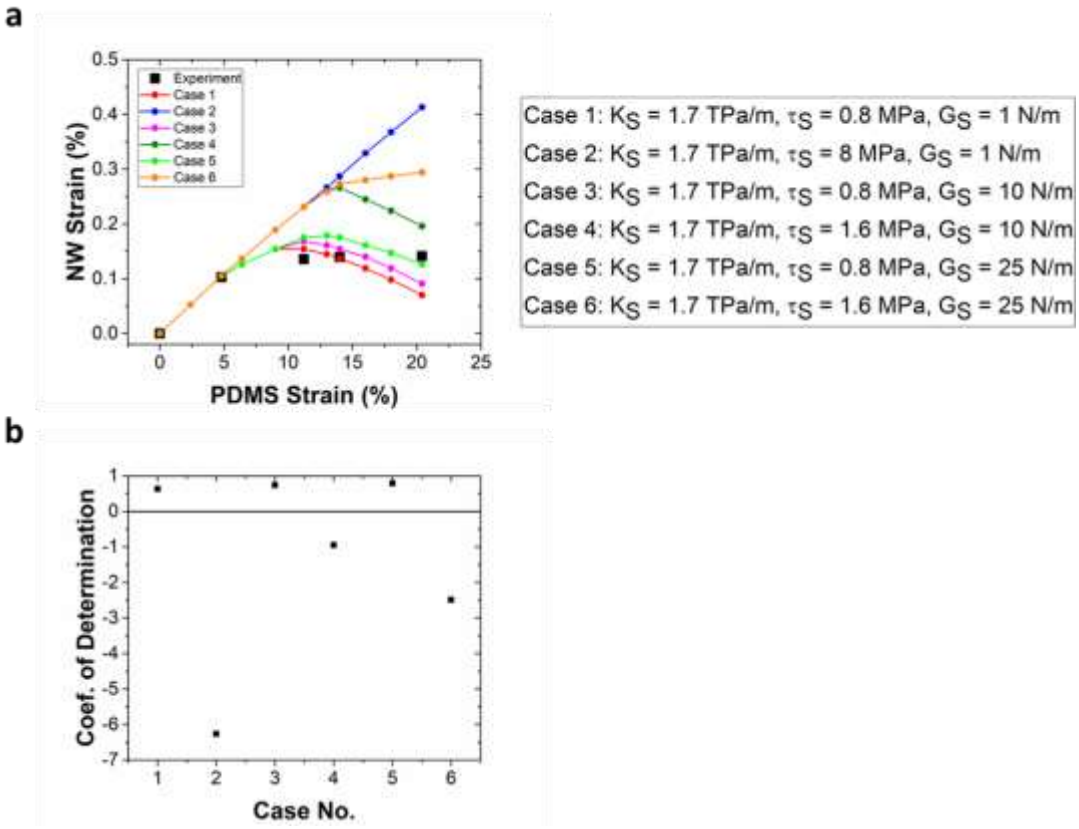

Figure 2.S3 (a) Comparison between the experiment average SiNW strain for the nontreated PDMS COMPOSITE with the average SiNW strain calculated in FEA by varying the interface parameters of the traction-separation law employed in the case of UVO-treated PDMS COMPOSITE and (b) R squared curve.

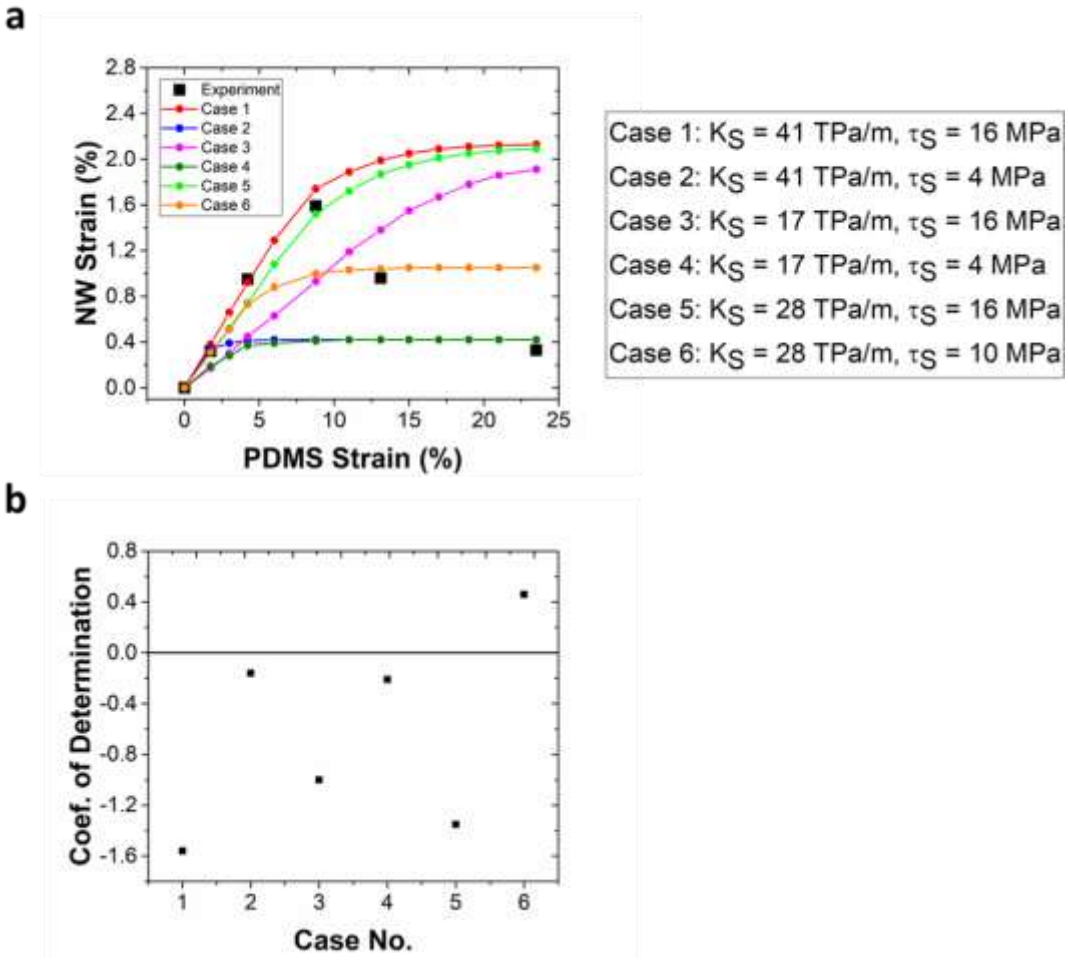

Figure 2.S4 (a) Comparison between the experiment average SiNW strain for the UVO-treated PDMS COMPOSITE with the average SiNW strain calculated in FEA by varying the interface parameters of the traction-separation law employed in the case of nontreated PDMS COMPOSITE and (b) R squared curve.

REFERENCES

1. Fan, Z. Y., Ho, J. C., Takahashi, T., Yerushalmi, R., Takei, K., Ford, A. C., Chueh, Y. L., and Javey, A., 2009, Toward the Development of Printable Nanowire Electronics and Sensors. Adv. Mater., 21(37), pp. 3730–3743;
2. Ju, S., Facchetti, A., Xuan, Y., Liu, J., Ishikawa, F., Ye, P., Zhou, C., Marks, T. J., and Janes, D. B., 2007, Fabrication of Fully Transparent Nanowire Transistors for Transparent and Flexible Electronics. Nat. Nanotechnol., 2, pp. 378–384;
3. McAlpine, M. C., Ahmad, H., Wang, D. W., and Heath, J. R., 2007, Highly Ordered Nanowire Arrays on Plastic Substrates for Ultrasensitive Flexible Chemical Sensors. Nat. Mater. 6, pp. 379–384;
4. Lu, W., and Lieber, C. M., 2006, Semiconductor Nanowires. J. Phys. D: Appl. Phys., 39, pp. R387–R406;
5. Hu, L. B., Kim, H. S., Lee, J. Y., Peumans, P., and Cui, Y., 2010, Scalable Coating and Properties of Transparent, Flexible, Silver Nanowire Electrodes. ACS Nano, 4(5), pp. 2955–2963;
6. Wu, J., Zang, J., Rathmell, A. R., Zhao, X., and Wiley, B. J., 2013, Reversible Sliding in Networks of Nanowires. Nano Lett., 13(6), pp. 2381–2386;
7. Yao, S., and Zhu, Y., 2015, Nanomaterial-Enabled Stretchable Conductors: Strategies, Materials and Devices. Adv. Mater., 27(9), pp. 1480–4511;
8. Hammock, M. L., Chortos, A., Tee, B. C.-K., Tok, J. B.-H., and Bao, Z., 2013, 25th Anniversary Article: The Evolution of Electronic Skin (E-Skin): A Brief History, Design Considerations, and Recent Progress. Adv. Mater., 25(42), pp. 5997–6038;

9. Xu, F., Lu, W., and Zhu, Y., 2011, Controlled 3D Buckling of Silicon Nanowires for Stretchable Electronics. ACS Nano, 5(1), pp. 672–678;
10. Ryu, S. Y., Xiao, J. L., Il Park, W., Son, K. S., Huang, Y. Y., Paik, U., and Rogers, J. A., 2009, Lateral Buckling Mechanics in Silicon Nanowires on Elastomeric Substrates. Nano Lett., 9(9), pp. 3214–3219;
11. Durham, J. W., and Zhu, Y., 2013, Fabrication of Functional Nanowire Devices on Unconventional Substrates Using Strain-Release Assembly. ACS Appl. Mater. Interfaces, 5(2), pp. 256–261;
12. Baughman, R. H., Zakhidov, A. A., and de Heer, W. A., 2002, Carbon Nanotubes—The Route Toward Applications. Science, 297, pp. 787–792;
13. De Volder, M. F. L., Tawfick, S. H., Baughman, R. H., and Hart, A. J., 2013, Carbon Nanotubes: Present and Future Commercial Applications. Science, 339(6119), pp. 535–539;
14. Cheng, G., Chang, T.-H., Qin, Q., Huang, H., and Zhu, Y., 2014, Mechanical Properties of Silicon Carbide Nanowires: Effect of Size-Dependent Defect Density. Nano Lett., 14(2), pp. 754–758;
15. Wu, R., Zhou, K., Yue, C. Y., Wei, J., and Pan, Y., 2015, Recent Progress in Synthesis, Properties and Potential Applications of SiC Nanomaterials. Prog. Mater. Sci., 72, pp. 1–60;
16. Chen, J., Conache, G., Pistol, M.-E., Gray, S. M., Borgstr€om, M. T., Xu, H., Xu, H. Q., Samuelson, L., and Ha˚kanson, U., 2010, Probing Strain in Bent Semiconductor Nanowires With Raman Spectroscopy. Nano Lett., 10(4), pp. 1280–1286;

17. Wei, B., Zheng, K., Ji, Y., Zhang, Y., Zhang, Z., and Han, X., 2012, SizeDependent Bandgap Modulation of ZnO Nanowires by Tensile Strain. Nano Letters, 12(9), pp. 4595–4599;
18. Qin, Q. Q., and Zhu, Y., 2011, Static Friction Between Silicon Nanowires and Elastomeric Substrates. ACS Nano 5(9), pp. 7404–7410;
19. Chen, Y., Zhu, Y., Chen, X., and Liu, Y., 2016, Mechanism of the Transition From In-Plane Buckling to Helical Buckling for a Stiff Nanowire on an Elastomeric Substrate. ASME J. Appl. Mech., 83(4), p. 041011;
20. Chen, Y., Liu, Y., Yan, Y., Zhu, Y., and Chen, X., 2016, Helical Coil Buckling Mechanism for a Stiff Nanowire on an Elastomeric Substrate. J. Mech. Phys. Solids, 95, pp. 25–43;
21. Barber, A.H., Cohen, S.R. and Wagner, H.D., 2003. Measurement of carbon nanotube–polymer interfacial strength. Appl. Phys. Lett, 82(23), pp.4140-4142;
22. Wong, M., Paramsothy, M., Xu, X.J., Ren, Y., Li, S. and Liao, K., 2003. Physical interactions at carbon nanotube-polymer interface. Polymer, 44(25), pp.7757-7764;
23. Manoharan, M.P., Sharma, A., Desai, A.V., Haque, M.A., Bakis, C.E. and Wang, K.W., 2009. “The interfacial strength of carbon nanofiber epoxy composite using single fiber pullout experiments,” Nanotechnology, 20(29), p.295701;
24. Ozkan, T., Chen, Q. and Chasiotis, I., 2012. Interfacial strength and fracture energy of individual carbon nanofibers in epoxy matrix as a function of surface conditions. Compos. Sci. Technol., 72(9), pp.965-975;
25. Chen, X., Zhang, L., Zheng, M., Park, C., Wang, X. and Ke, C., 2015. Quantitative nanomechanical characterization of the van der Waals interfaces between carbon nanotubes and epoxy. Carbon, 82, pp.214-228;

26. Wagner, H.D., Lourie, O., Feldman, Y. and Tenne, R., 1998. Stress-induced fragmentation of multiwall carbon nanotubes in a polymer matrix. Appl. Phys. Lett., 72(2), pp.188-190;
27. Lachman, N., Carey, B.J., Hashim, D.P., Ajayan, P.M. and Wagner, H.D., 2012. Application of continuously-monitored single fiber fragmentation tests to carbon nanotube/carbon microfiber hybrid composites. Compos. Sci. Technol., 72(14), pp.1711-1717;
28. Kamae, T. and Drzal, L.T., 2012. Carbon fiber/epoxy composite property enhancement through incorporation of carbon nanotubes at the fiber–matrix interphase–Part I: The development of carbon nanotube coated carbon fibers and the evaluation of their adhesion. Composites Part A, 43(9), pp.1569-1577;
29. Li, R., Lachman, N., Florin, P., Wagner, H.D. and Wardle, B.L., 2015. Hierarchical carbon nanotube carbon fiber unidirectional composites with preserved tensile and interfacial properties. Compos. Sci. Technol., 117, pp.139-145;
30. Godara, A., Gorbatikh, L., Kalinka, G., Warrier, A., Rochez, O., Mezzo, L., Luizi, F., Van Vuure, A.W., Lomov, S.V. and Verpoest, I., 2010. Interfacial shear strength of a glass fiber/epoxy bonding in composites modified with carbon nanotubes. Compos. Sci. Technol., 70(9), pp.1346-1352;
31. Canal, L.P., González, C., Segurado, J. and LLorca, J., 2012. Intraply fracture of fiber-reinforced composites: microscopic mechanisms and modeling. Compos. Sci. Technol., 72(11), pp.1223-1232;
32. Medina M, C., Molina-Aldareguía, J.M., González, C., Melendrez, M.F., Flores, P. and LLorca, J., 2016. Comparison of push-in and push-out tests for measuring interfacial shear

strength in nano-reinforced composite materials. J. Compos. Mater., 50(12), pp.1651-1659;

33. Molina-Aldareguía, J.M., Rodríguez, M., González, C. and LLorca, J., 2011. An experimental and numerical study of the influence of local effects on the application of the fibre push-in test. Philos. Mag., 91(7-9), pp.1293-1307;
34. Rodríguez, M., Molina-Aldareguía, J.M., González, C. and LLorca, J., 2012. A methodology to measure the interface shear strength by means of the fiber push-in test. Compos. Sci. Technol., 72(15), pp.1924-1932;
35. Medina M, C., Molina-Aldareguía, J.M., González, C., Melendrez, M.F., Flores, P. and LLorca, J., 2016. Comparison of push-in and push-out tests for measuring interfacial shear strength in nano-reinforced composite materials. J. Compos. Mat., 50(12), pp.1651-1659;
36. Pisanova, E., Zhandarov, S., Mäder, E., Ahmad, I. and Young, R.J., 2001. Three techniques of interfacial bond strength estimation from direct observation of crack initiation and propagation in polymer–fibre systems, Composites Part A, 32(3-4), pp.435-443;
37. Zhandarov, S., Gorbatkina, Y. and Mäder, E., 2006. Adhesional pressure as a criterion for interfacial failure in fibrous microcomposites and its determination using a microbond test. Compos. Sci. technol., 66(15), pp.2610-2628;
38. Zu, M., Li, Q., Zhu, Y., Dey, M., Wang, G., Lu, W., Deitzel, J.M., Gillespie Jr, J.W., Byun, J.H. and Chou, T.W., 2012. The effective interfacial shear strength of carbon nanotube fibers in an epoxy matrix characterized by a microdroplet test. Carbon, 50(3), pp.1271-1279;

39. Bordag, M., Ribayrol, A., Conache, G., Fröberg, L.E., Gray, S., Samuelson, L., Montelius, L. and Pettersson, H., 2007. Shear stress measurements on InAs nanowires by AFM manipulation. small, 3(8), pp.1398-1401;
40. Jiang, T., Huang, R. and Zhu, Y., 2014. Interfacial sliding and buckling of monolayer graphene on a stretchable substrate. Adv. Funct. Mater., 24(3), pp.396-402;
41. Guo, G. and Zhu, Y., 2015. Cohesive-shear-lag modeling of interfacial stress transfer between a monolayer graphene and a polymer substrate. J. Appl. Mech., 82(3), p.031005;
42. Cox, H.L., 1952. The elasticity and strength of paper and other fibrous materials. Br. J. appl. Phys., 3(3), p.72;
43. She, H., Malotky, D. and Chaudhury, M.K., 1998. Estimation of adhesion hysteresis at polymer/oxide interfaces using rolling contact mechanics. Langmuir, 14(11), pp.3090-3100;
44. Zhu, Y., Xu, F., Qin, Q., Fung, W.Y. and Lu, W., 2009. Mechanical properties of vapor− liquid− solid synthesized silicon nanowires. Nano letters, 9(11), pp.3934-3939;
45. Wu, Y., Cui, Y., Huynh, L., Barrelet, C.J., Bell, D.C. and Lieber, C.M., 2004. Controlled growth and structures of molecular-scale silicon nanowires. Nano letters, 4(3), pp.433-436;
46. Sneddon, I.N., 1965. The relation between load and penetration in the axisymmetric Boussinesq problem for a punch of arbitrary profile. Int. J. Eng. Sci., 3(1), pp.47-57;
47. Barenblatt, G.I., 1959. The formation of equilibrium cracks during brittle fracture. General ideas and hypotheses. Axially-symmetric cracks. J. Appl. Math. Mech., 23(3), pp.622-636;
48. Dugdale, D.S., 1960. “Yielding of steel sheets containing slits,” J. Mech. Phys. Solids, 8(2), pp.100-104;

49. Alfano, G., 2006. On the influence of the shape of the interface law on the application of cohesive-zone models. Compos. Sci. Technol., 66(6), pp.723-730;
50. Sun, Y. and Rogers, J.A., 2007. Structural forms of single crystal semiconductor nanoribbons for high-performance stretchable electronics. J. Mater. Chem., 17(9), pp.832-840;
51. Xu, F., Durham III, J.W., Wiley, B.J. and Zhu, Y., 2011. Strain-release assembly of nanowires on stretchable substrates. ACS nano, 5(2), pp.1556-1563;
52. Johnston, I.D., McCluskey, D.K., Tan, C.K.L. and Tracey, M.C., 2014. Mechanical characterization of bulk Sylgard 184 for microfluidics and microengineering. J. Micromech. Microeng., 24(3), p.035017;
53. Chandra, N., Li, H., Shet, C., & Ghonem, H., 2002, Some issues in the application of cohesive zone models for metal–ceramic interfaces. Int. J. Solids Struct., 39(10), 2827-2855;
54. Snozzi, L., & Molinari, J. F., 2013, A cohesive element model for mixed mode loading with frictional contact capability. Int. J. Numer. Meth. Eng., *93*(5), 510-526;
55. Nian, G., Li, Q., Xu, Q., & Qu, S., 2018, A cohesive zone model incorporating a Coulomb friction law for fiber-reinforced composites. Compos. Sci. Technol., 157, 195-201;
56. Geubelle, P. H., & Baylor, J. S., 1998, Impact-induced delamination of composites: a 2D simulation. Composites Part B, 29(5), 589-602;
57. Dandekar, C. R., & Shin, Y. C., 2011, Molecular dynamics based cohesive zone law for describing Al–SiC interface mechanics. Composites Part A, 42(4), 355-363;
58. Rajan, T. P. D., Pillai, R. M., & Pai, B. C., 1998, Reinforcement coatings and interfaces in aluminium metal matrix composites. J. Mater. Sci., 33(14), 3491-3503;

59. Rahman, R., & Haque, A., 2013, Molecular modeling of crosslinked graphene–epoxy nanocomposites for characterization of elastic constants and interfacial properties. Composites Part B, 54, 353-364;
60. Li, Y., & Seidel, G. D., 2015, Multiscale modeling of functionalized interface effects on the effective elastic material properties of CNT–polyethylene nanocomposites. Comput. Mater. Sci., 107, 216-234;
61. You, J. H., Lutz, W., Gerger, H., Siddiq, A., Brendel, A., Höschen, C., & Schmauder, S., 2009, Fiber push-out study of a copper matrix composite with an engineered interface: Experiments and cohesive element simulation. Int. J. Solids Struct., 46(25-26), 4277-4286;
62. Bianchi, F., & Zhang, X., 2011, A cohesive zone model for predicting delamination suppression in z-pinned laminates. Compos. Sci. Technol., 71(16), 1898-1907;
63. Israelachvili, J.N., 2011. Intermolecular and surface forces. Academic press;
64. Ratner, S., & Pappas, A., 1949, Biosynthesis of urea I. Enzymatic mechanism of arginine synthesis from citrulline. J. Biol. Chem., 179(3), 1183-1198;
65. http://www.rsc.org/Education/Teachers/Resources/cfb/metabolism.htm;
66. Guo, C.F. and Ren, Z., 2015. Flexible transparent conductors based on metal nanowire networks. Materials Today, 18(3), pp.143-154.

CHAPTER 3 Study of stress transfer between AgNW and PDMS COMPOSITE

3.1 Introduction

One-dimensional nanomaterials such as nanowires and nanotubes have been used in many applications ranging from composite materials[1,2] and flexible[3,4] or stretchable electrodes[5,6]. Among these nano structures, silver nanowires (AgNW) are greatly studied and applied in many devices due to silver's highest electrical conductivity when compared to other metals[7] and the fact that AgNWs can be grown by a variety of methods[8], including hydrothermal method, UV irradiation technique, and the polyol synthesis process, to cite a few. AgNWs are typically grown with diameters of 30-200 nm and lengths of 1-20 μm[9]. Another important characteristic of AgNWs is that they can form networks showing high transmittance for a wide range of wavelengths. AgNW networks have also replaced ITO in the development and fabrication of transparent electrodes[10,11]. Thanks to the superior electrical/optical performance of AgNWs, they have also been combined with soft polymeric substrates in order to produce low-cost flexible[12,13] and stretchable[14,15] devices.

By taking advantage of the buckling of aligned arrays of stiff materials on elastomeric substrates, important applications can be developed, such as stretchable electronics[16] and flexible optoelectronics[17]. Recent research shows several buckled or wrinkled structural configurations of nanomaterials by integrating them with compliant substrates subjected to mechanical forces[18,19]. Zhao et al[20] studied the buckling of elastic fibers embedded in a soft matrix. Ryu et al[21] reported the in-plane buckling of silicon nanowires on an elastomeric substrate while Khang et al[22] demonstrated the out-of-plane buckling of single-wall carbon nanotubes (SWNT) due to the small energy difference between normal and in-surface buckling of SWNTs and the rather small SWNT diameter (1 nm). Su et al[23] reported on the non-planar buckling of an elastic rod embedded on a soft matrix as coiled structures could be attained based on certain control parameters. As

mentioned previously, not only the buckling but also the fracture study of AgNWs is important as it may affect the performance of flexible and stretchable devices. Experimental measurements on the plasticity and failure of AgNWs are rare and challenging[24,25]. Zhu et al[26] reported stress-strain measurements and tensile strength of AgNWs using in-situ tensile tests inside a scanning electron microscope (SEM). Some researchers have used MD simulations in order to study the deformation mechanism behind the fracture of nanowires under tension or bending[27,28]. Kim et al[29] recently reported on a failure criterion for standalone AgNWs based on in-situ buckling and tensile tests.

Moreover, the interface mechanics between NWs and substrate play an important role in the performance and reliability of NW-based flexible and stretchable electronics especially when the structure is subjected large deformation. Buckling and/or fracture of nanowires on top of or embedded on a soft substrate can be controlled if the stress transfer mechanism is properly understood. For instance, it was observed the occurrence of interface sliding between Si NWs and PDMS COMPOSITE substrate[30] and that the interfacial sliding could be suppressed by increasing the static friction (interfacial strength)[31] when applying a surface treatment to PDMS COMPOSITE. Also, the NW buckling shape is greatly influenced by the interface sliding[32,33].

Tracking nano or sub-nano displacement of tiny structures such as MEMS devices and nanowires using an optical microscope can be quite challenging due to a resolution limitation related to the wavelength of the light being used by the optical microscope. This is known as Rayleigh criterion or the optical diffraction limit[34]. Several optical motion detection techniques have been used to circumvent this limitation, such as laser Doppler vibrometry[35] and interferometry with stroboscopic illumination[36]. However, theses methods are reportedly difficult to be applied in the detection of in-plane motion[37] as they are mostly used for the detection of out-of-plane motion. Nevertheless, digital image correlation (DIC) is a method that is increasingly

being adopted in order to enhance the resolution of in-plane measurements[38,39]. In this method, the images to be analyzed are assumed to have constant shape and intensity. The image of the structure at rest is used as a template when comparing to the subsequent images. The new position of each pixel is defined as the peak of a correlation function that is defined between pixels in the original template. The DIC method has manage to achieve sub-pixel resolution through several different algorithms such as the coarse-fine searce[40,41], peak-finding[42,43], Newton-Raphson[44-45] and other algorithms.

In this work, the interfacial mechanics between AgNW and PDMS COMPOSITE is evaluated through in-situ experiments under an optical microscope combined with DIC measurements. Samples composed of AgNWs on top of a PDMS COMPOSITE substrate were subjected to tensile tests when AgNWs are aligned to the direction of strain or are transversal to it (buckling). PDMS COMPOSITE samples were also subjected to UVO treatment in order strengthen the bonding between AgNW and PDMS COMPOSITE, making it possible to study the strength of AgNWs as their fracture strain could be obtained. Finally, AgNWs embedded on a PDMS COMPOSITE substrate (pristine and UVO-treated) were also studied.

3.2 Experimental setup

PDMS COMPOSITE film with a thickness of about *0.3 mm* was prepared using Sylgard 184 (Dow Corning) by mixing the "base" and the "curing agent" with a ratio of 10:1. After the air bubbles disappeared, the liquid mixture was spin-coated on a silicon wafer and then thermally cured at *100 degree C* for *30 min*. After the PDMS COMPOSITE film was cured, the film was first peeled-off the silicon wafer and then placed on a 30 degree-tilted glass substrate. UVO-treated PDMS COMPOSITE films were prepared by using UVO Cleaner Moder No. 42A (Jelight Company, Inc.) and the films were UVO-treated for *45 minutes*. AgNWs were synthesized by

polyol method and diluted in ethanol with a concentration of *0.02 mg/ml*. The as-prepared AgNWs solution was dropped on the high-end of PDMS COMPOSITE film with a syringe. The AgNWs flowed on the PDMS COMPOSITE surface and were aligned along flowing direction. Testing samples with AgNWs embedded in UVO-treated PDMS COMPOSITE were prepared in a similar fashion. The only difference was that another UVO-treated PDMS COMPOSITE substrate was placed on top of the AgNW/PDMS COMPOSITE sample. As a last step, the samples composed of pristine PDMS COMPOSITE and UVO-treated PDMS COMPOSITE with AgNWs deposited were cut into *10 x 40 mm* rectangle shape and installed on Fullam stage (Ernest F. Company) for in-situ testing under an optical microscope (Nikon LV150 Microscope) with 100x magnification lenses. Pictures taken of the samples subjected to increasing levels of strain were analyzed via digital image correlation.

3.3 AgNW/PDMS COMPOSITE experiments and FEA modeling

3.3.1 Stretching of AgNWs on top of nontreated PDMS COMPOSITE

The samples used in the initial experiments were composed of AgNWs placed on top of a pristine PDMS COMPOSITE substrate and aligned with the direction of the tensile strain applied to the substrate. The maximum strain applied to PDMS COMPOSITE was about *31%*. In this case, sliding is expected to happen at the interface between AgNW and PDMS COMPOSITE once the interfacial stress reaches a critical value according to the nonlinear shear-lag model. As shown in **Figure 3.1**, three different AgNWs were used: NW #1 (*10.4 μm long*) and NW #3 (*12.4 μm*) being in the same PDMS COMPOSITE substrate while NW #2 (*11.4 μm*) being from a different batch. The samples were stretched under an optical microscope while images were taken at different strain levels. The overall strain in the AgNW was measured using a open source digital image

correlation software based on Matlab and developed by Gianola et al[46]. The software accuracy is reported to be around 10% of a pixel and the pixel size of the images taken was about *30 nm*.

In order to model the interface properties between AgNW and a pristine PDMS COMPOSITE, a 3D finite element analysis (FEA) was performed in Abaqus 6.14 using cohesive zone modeling. In a NW/polymer system, a large fracture process zone may develop at the interface under stretching, where the cohesive traction is assumed to vary along the fracture process zone but depend only on the local sliding and/or opening[47]. Thus, the cohesive law can be considered as a basic fracture property. A typical cohesive zone model takes a similar feature of traction–separation relationship. Although there are many forms that a traction-separation law can assume[48,49], previous results[50] from the analysis of the SiNW on top of a pristine PDMS COMPOSITE sample shows that a more suitable traction-separation law has the form shown in **Figure 3.2(a)**. Two key parameters are necessary for the traction-separation law to be defined: interface stiffness (K_S) and interface shear strength (τ_s). These parameters were found by comparing the average strain found by FEA with the experimental strain values.

In the FEA model, taking advantage of the symmetry of the problem, only half of the NW/substrate system in the substrate stretching direction was considered. The AgNWs used in this study have a diameter of *60 nm*, based on measurements done in SEM, which corresponds to an Young's modulus of approximately *90 GPa*[51]. The contact width between AgNW and PDMS COMPOSITE was estimated[52] as the side length of the pentagonal cross section[51] of the AgNW. The indentation depth was found to be negligible[53]. C3D8R reduced linear brick elements were used to model PDMS COMPOSITE and AgNW. It was adopted an isotropic linear elastic material behavior for both structures. A Poisson ratio of *0.3* was used for the SiNW. For the PDMS COMPOSITE substrate, it was assigned a Young's modulus of *2 MPa* and a Poisson ratio of *0.48*[54].

The length of each AgNW was taken as the same as in the experiments. As mentioned before, the values found for the interface parameters were validated by comparing the average strain found by FEA with the experiment strain values. Figure 2(b) shows the average strain results found for the three AgNWs analyzed. Overall, the strain increases linearly until it reaches a plateau value that varies from *0.12* to *0.16%*. In order to best fit the experimental results, the interfacial parameters used in the FEA simulation were $K_S = 3.7\ TPa/m$ and $\tau_S = 1.2\ MPa$. **Figure 3.2(c)** shows a good correlation between the strain values for NW #1.

It's interesting to note that these experiments have not induced fracture in any of the AgNWs. That can be explained by considering that the bonding between AgNW and pristine PDMS COMPOSITE is of physical nature. This bonding originates from electrotactic interactions between neutral atoms and molecules due to the instantaneous dipole moment generated by their constant movement. The interaction between the dipoles gives rise to an instantaneous attractive force between the atoms or molecules[55]. Because these dispersion forces are relatively weak in nature, the strain transfer from the substrate to the AgNW is not efficient resulting in a AgNW subjected to lower stress.

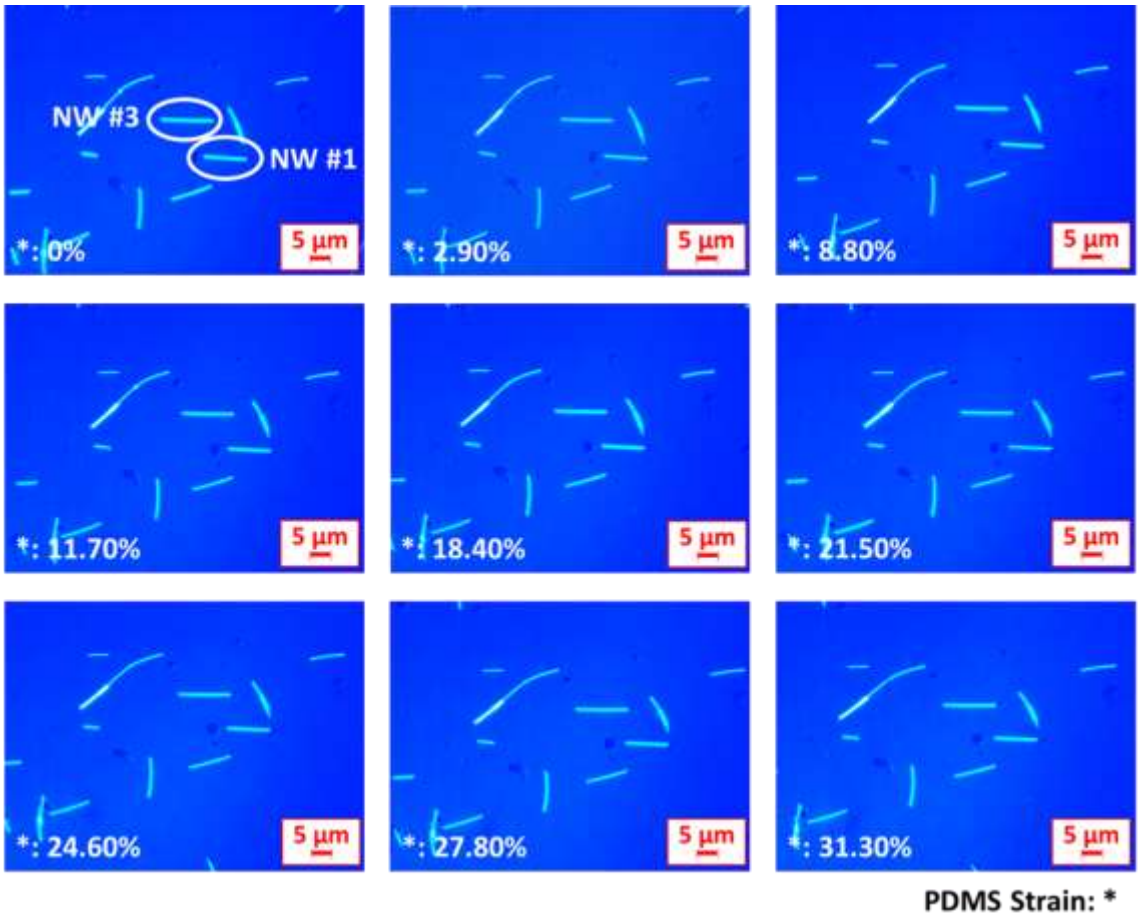

Figure 3.1 NW#1 and NW#3 placed on top of pristine PDMS COMPOSITE substrate subjected to the tensile strain shown in the pictures.

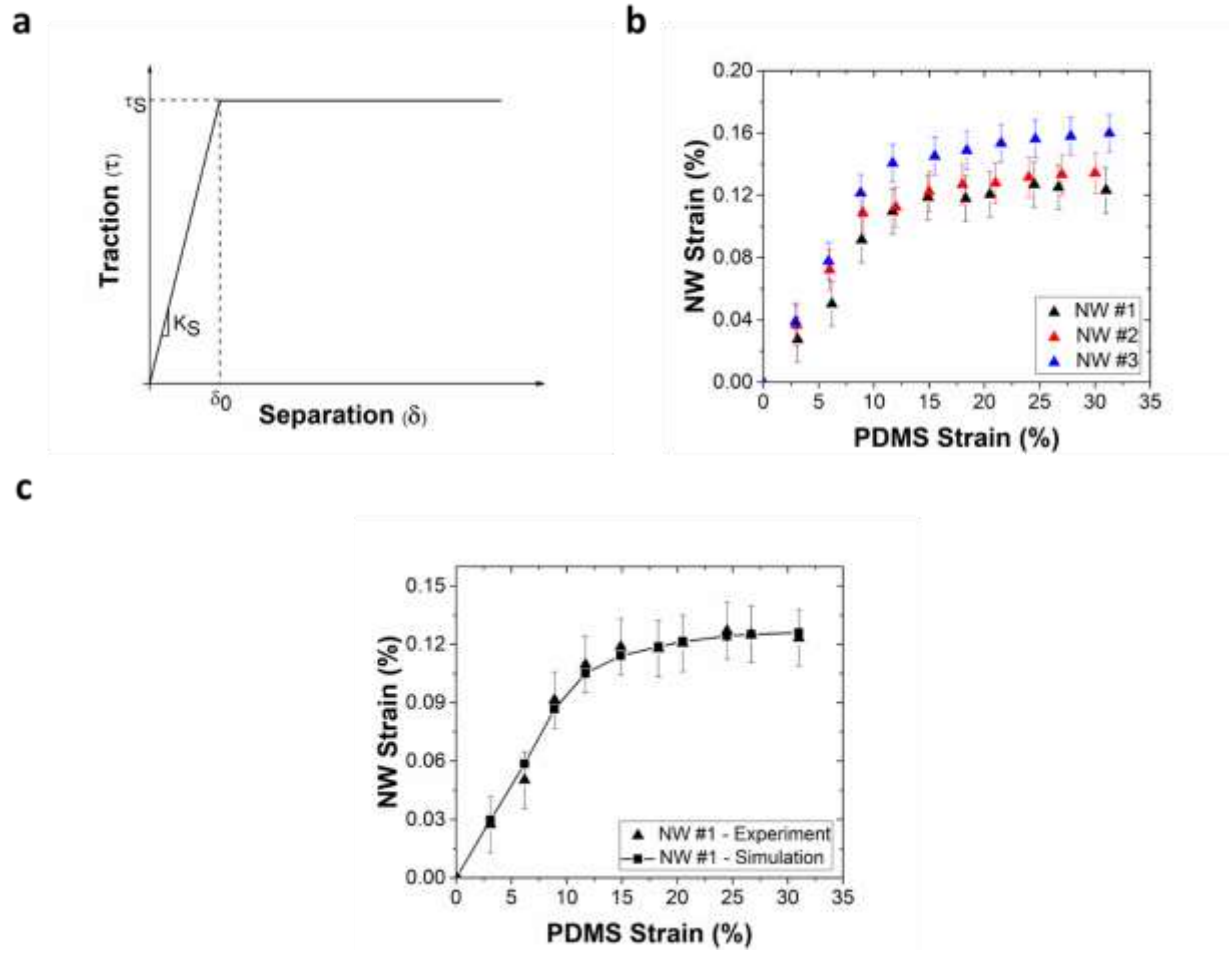

Figure 3.2 (a) Traction-separation law used in the FEA cohesive model for AgNW on top of pristine PDMS COMPOSITE , (b) experimental results for the average strain in three different AgNWs, and (c) experimental vs. FEA results for the average strain in NW #1.

3.3.2 Buckling of AgNWs on top of nontreated PDMS COMPOSITE

Similar to the previous experiments, AgNWs were placed on top of a pristine PDMS COMPOSITE substrate; but this time they were positioned in the transverse direction with respect to the strain applied to PDMS COMPOSITE in order to study AgNW buckling. Tensile strain was applied to PDMS COMPOSITE to the point when AgNW buckling could be perceived through the images and the post-buckling behavior could also be captured. **Figure 3.3** shows one of the AgNWs tested (NW #3). Three different AgNWs were used: NW #1 (*12.6 μm* long) and NW #2

(*14.6 μm*) being in the same PDMS COMPOSITE substrate while NW #3 (*18.8 μm*) being from a different batch. The experiments were conducted in a similar fashion as in the previous case and images were taken by optical microscope and analyzed by DIC. The pixel size of the images taken was about *30 nm*.

Figure 3.3 shows the deformation evolution for the NW #3, which buckles when the strain applied to the PDMS COMPOSITE is about *6%*. A small perturbation close to the center of NW #3 can be seen when the strain applied to the PDMS COMPOSITE is *5.95%*. After that, the buckling becomes more pronounced as the center of the NW deforms to a lump-like shape. The other AgNWs tested also presented similar behavior. From **Figure 3.4(a)**, NW #1 and NW #2 buckled when the strain applied to the PDMS COMPOSITE substrate was around *14%* and *13%*, respectively and that the average strain prior to buckling in the three AgNWs tested varied from *0.10%* to *0.15%*. The critical compressive strain for AgNW buckling can be analytically estimated[20,23]. Considering the AgNW as a slender beam, the equilibrium equation is given by:

$$E_{NW} I \frac{\partial^4 w}{\partial x^4} + E_{NW} S \varepsilon_0 \frac{\partial^2 w}{\partial x^2} + Kw = 0 \qquad \textbf{(3.1)}$$

where ε_0 is the overall compressive strain in the substrate, $E_f I$ is the bending stiffness of the AgNW and S is the cross sectional area. The buckling mode $w = Acos(kz)$ is given in terms of the amplitude A and wavenumber $k = 2\pi/\lambda$, in which λ is the buckling wavelength. The Young's modulus of PDMS COMPOSITE was taken as the effective stiffness of the soft foundation K. When $kr \to 0$, **Equation (3.1)** becomes:

$$E_{NW} S \varepsilon = E_{NW} I k^2 + \frac{E_{PDMS}}{k^2} \qquad \textbf{(3.2)}$$

Minimizing **Equation (3.2)** with respect to the wavenumber k gives the critical buckling strain as:

$$\varepsilon_c = \frac{I}{S}k_c^2 + \frac{E_{PDMS}}{E_{NW}Sk_c^2} \quad \textbf{(3.3)}$$

where the critical wave number is given by $k_c = \sqrt[4]{E_{PDMS}/E_{NW}I}$. Using the measurements and elastic properties of the AgNWs used in the experiments, the critical AgNW buckling strain in found to be *0.21%*. However, the result obtained from the previous calculation has to be compared with the maximum compressive strain experienced by the AgNW. By considering the interface between AgNW and PDMS COMPOSITE to be weak and not perfectly bonded, it's known from the shear-lag analysis that maximum strain in the NW is found in its center[56]. In other words, when the maximum compressive strain in the AgNW reaches the critical strain given by **Equation (3.3)**, buckling is supposed to occur.

FEA modeling was used in order to obtain the strain distribution along the AgNW (NW #3) and also to obtain the overall strain in the AgNW and in the PDMS COMPOSITE prior to buckling. The model was very similar to the one described previously (same materials properties and elements for both AgNW and PDMS COMPOSITE), except that now the AgNW is transversally placed with respect to the direction of the applied strain in PDMS COMPOSITE. Also, the same interface parameters ($K_S = 3.7\ TPa/m$ and $\tau_S = 1.2\ MPa$) were adopted since the PDMS COMPOSITE substrate used is pristine and has not undergone any surface modification. The simulation was performed in two steps. In the first step, a small residual force was applied perpendicular to the center of the AgNW in order to trigger the desired buckling shape in the subsequent step. Several test were conducted to ensure that the magnitude of the trigger load was sufficiently small so that it did not affect the overall post-buckling solution. Next, the trigger force was removed from the model and the post-buckling response was captured through the Riks method offered by Abaqus Standard. **Figure 3.4(a)** shows the average strain obtained through the simulation of each of the three AgNWs just before they buckled. From the FE model, the strain

applied to the PDMS COMPOSITE on the onset of AgNW buckling was *15.67%*, *12.02%*, and *5.65%* for NW #1, NW #2, and NW#3; respectively. These results showed good agreement with the experimental data measured. **Figure 3.4(b)** shows the strain distribution along the NW #3 prior to buckling. The plot reveals that the maximum strain at NW #3 was about *0.20%*, which is very close to the critical value analytically obtained through **Equation (3.3)**. **Figure 3.4(c)** shows the strain distribution along the NW #3 after buckling has occurred. It can be seen that a region with large deformation develops at the center of NW #3 as the strain applied to the PDMS COMPOSITE increases. The maximum strain reached was about *2%*, which is very close to the fracture strain reported in literature for AgNWs[26,29]. Also the highly localized nature of the strain distribution makes fracture more likely to happen due to the high stress concentration in the region. In fact, experiments conducted by gradually removing the applied strain in PDMS COMPOSITE shows that most AgNWs after suffering considerable buckling will not come back to their original shape after the strain is released. The evolution of NW #3 deformation modeled by FEA is presented in **Figure 3.5** and it shows that the NW #3 buckling occurred in-plane. SEM images of the postmortem specimen also shows in-plane buckling of the AgNWs (**Figure 3.S1(a)**). It has been reported[21] that in the case of NWs, lateral buckling has a lower energy compared to normal buckling and it's therefore more energetically favorable to occur.

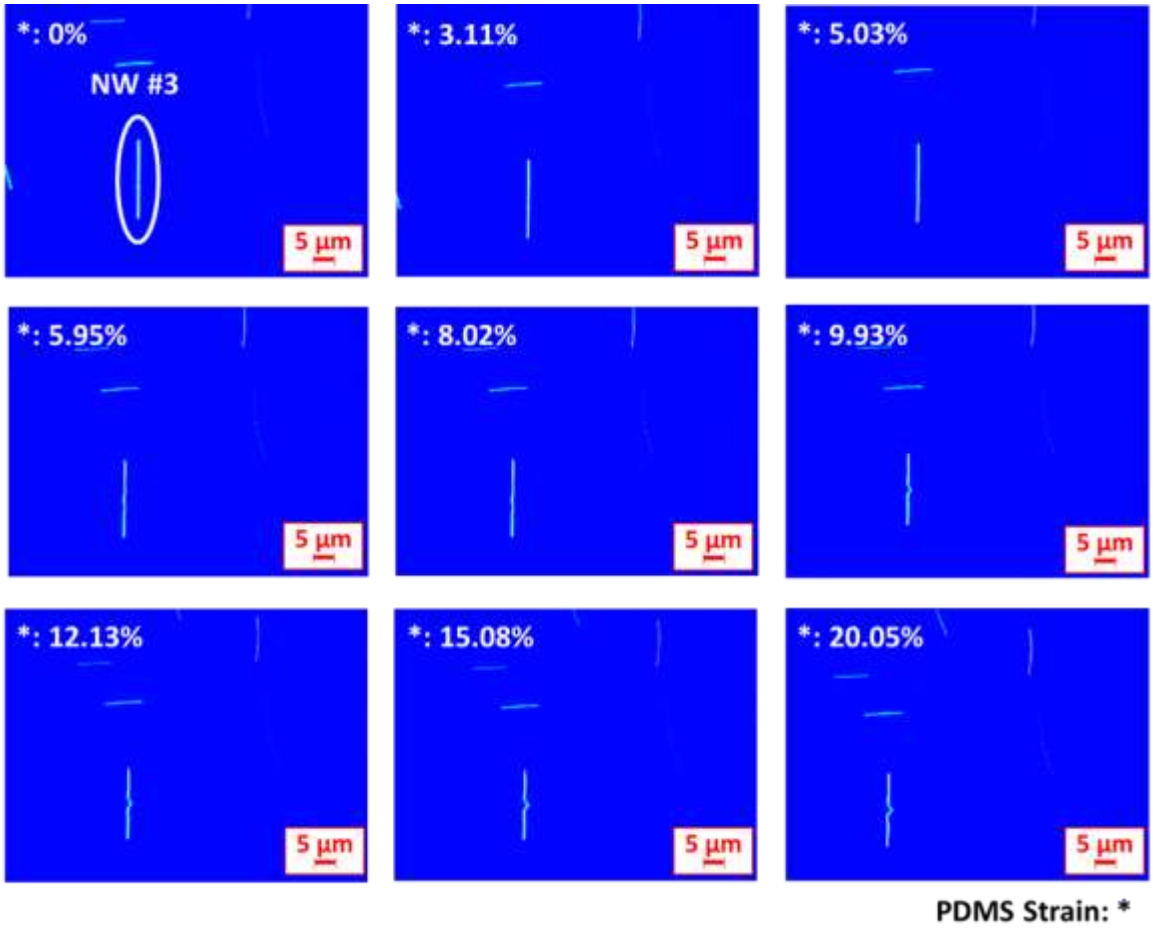

Figure 3.3 NW #3 transversally placed on top of pristine PDMS COMPOSITE substrate subjected to the tensile strain shown in the pictures.

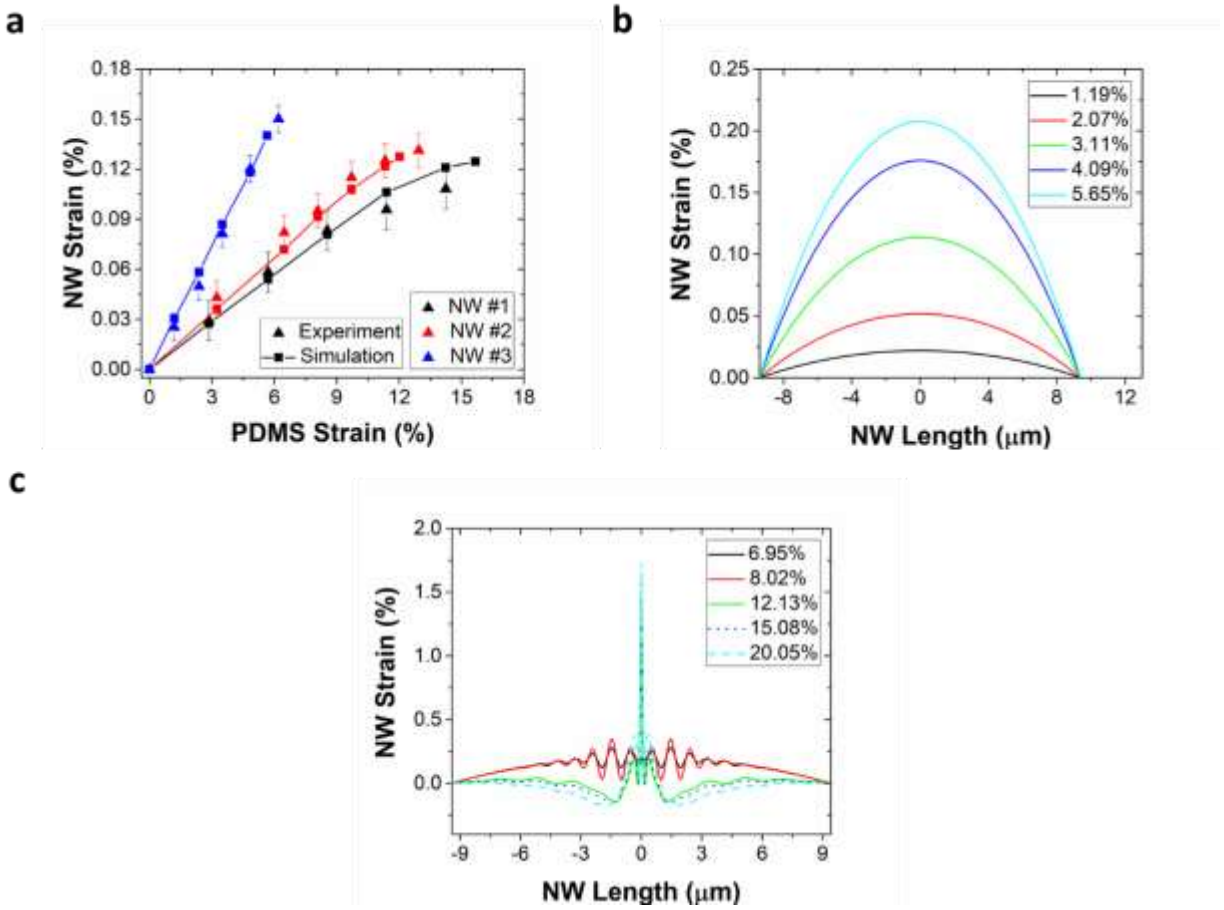

Figure 3.4 (a) Experimental vs. FEA results for the average strain in three different AgNWs on top of pristine PDMS COMPOSITE and (b) strain distribution along NW #3 length before buckling happens and (c) strain distribution along NW #3 length after buckling happens.

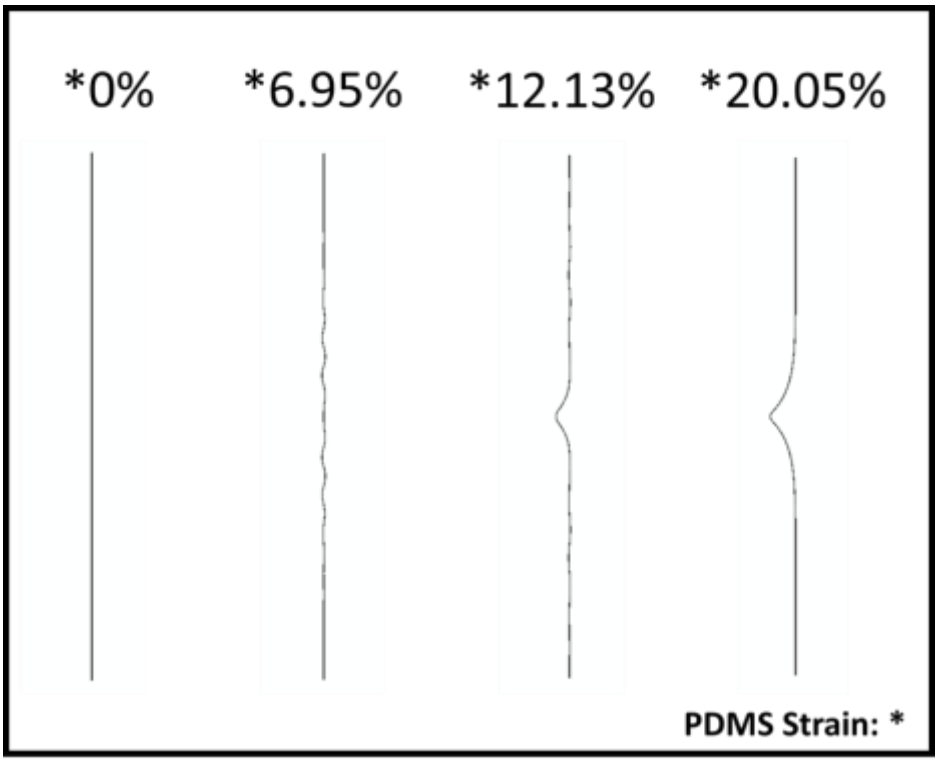

Figure 3.5 Buckling evolution of NW #3 obtained by FEA simulation at specific strain values applied to the PDMS COMPOSITE substrate.

3.3.3 Fracture of AgNWs on top of UVO-treated PDMS COMPOSITE

Since AgNW fracture could not be perceived using a pristine PDMS COMPOSITE, the substrate was UVO-treated in order to increase the adhesion between the components. The chemical bonds formed between AgNW and UVO-treated PDMS COMPOSITE are much stronger when compared to covalent bonding[31,57], which should ensure a more effective strain transfer from the substrate to the AgNW and increase the possibility of its fracture.

The PDMS COMPOSITE sample was subjected to a *45 min*. UVO-treatment carried out in a commercial UVO chamber. After that, AgNWs were placed on top of the UVO-treated PDMS COMPOSITE and aligned with the direction of the tensile strain applied to the substrate. As shown in **Figure 3.6**, two different AgNWs were used from the same PDMS COMPOSITE substrate: NW #1 (*11.6 μm*) and NW #2 (*14.4 μm*). The overall strain in the AgNW captured by the optical

microscope, was measured by the DIC software aforementioned. **Figure 3.7(b)** shows that the overall strain level is much higher than when the AgNWs are on top of a pristine PDMS COMPOSITE, which corroborates a stronger UVO-treated interface. Results show that both AgNWs #1 and #2 were broken when the strain applied to the PDMS COMPOSITE was about *5.32%* and the average strain at the fracture point for NW #1 was *1.38%* and for NW #2 was *1.75%*. Postmortem specimen were analyzed under SEM to make sure the AgNWs were indeed fractured rather than being out-of-plane buckled (**Figure 3.S1(b)**).

A 3D finite element analysis was conducted in Abaqus using cohesive zone modeling in order to derive the interface properties for the bonding between AgNW and UVO-treated PDMS COMPOSITE and subsequently determine the strain distribution of the AgNWs just before it breaks. Similarly to the case of a pristine PDMS COMPOSITE, a traction-separation law relationship was used to better fit the experimental data. Previous results[50] from the analysis of the SiNW on top of a UVO-treated PDMS COMPOSITE sample shows that a more suitable traction-separation law has the form shown in **Figure 3.7(a)**. The linear decrease in traction to zero after its maximum value can be attributed to the irreversible breaking of some of the interfacial chemical bonds. As an endergonic chemical reaction, these bonds need a certain time to take place and can be permanently broken as the interfacial stress increase which may cause not only sliding but also irreversible interfacial damage. In this case, not only interface stiffness (K_S) and interface shear strength (τ_s) but also the fracture toughness G_s, which is given by the area under the traction-separation plot, must be obtained. Eventually, the AgNW average strain found by the FEA model was compared to the experimental results.

The FEA model of AgNW on top of UVO-treated PDMS COMPOSITE also made use of the symmetry of the problem as previously stated. Mechanical properties, dimensions, and element

types of both AgNW and PDMS COMPOSITE were kept the same. The length of each AgNW was taken as the same as in the experiments. In the FEA model, it was applied a strain to the PDMS COMPOSITE up to the point when fracture in the AgNW could be perceived in the experiments. The FEA strain results were matched with the experimental results by varying the interface parameter values. The parameters chosen were $K_S = 140\,TPa/m$, $\tau_S = 24\,MPa$, and $G_S = 8\,N/m$. **Figure 3.7(b)** shows the average strain results found for the two AgNWs analyzed and it's possible to note that just before fracture NW #1 and NW #2 had an average strain of *1.25%* and *1.86%*, respectively. **Figure 3.7(c)** shows the strain distribution along the AgNW when the strain applied in the PDMS COMPOSITE caused the fracture of the AgNW (about *5.32%*). In the plot, it's possible to see that the maximum strain at the center of both AgNWs are *1.73%* and *2.28%* for NW #1 and NW #2, respectively. These values are very close to the fracture strain reported in the literature of AgNWs[26,29] which is about *2-3%* strain.

After fracture occurred, the length of the resultant segments were measured. NW #1 was initially broken into two segments with length of *6.15 μm* (left) and *5.60 μm* (right), while NW #2 was initially divided into two segments with length of *7.25 μm* (left) and *7.42 μm* (right). When adding the fractured segments, the resultant size is the same as the original size of each of the AgNWs just before its fracture. These results suggest the AgNWs tested did not suffer plastic deformation. In fact, these findings corroborates with the results obtained by tensile tests performed on AgNWs using an in-situ SEM nanomechanical testing setup[26]. In these experiments, after failure, a close examination of the AgNW fracture ends showed that there was no apparent diameter reduction (i.e. no large-scale yielding) along the AgNW excerpt very close to the fracture surface. The researchers agreed this observations was consistent with the stress-strain data where the plasticity is limited compared to bulk face-centered cubic (FCC) metals. Both fractography

and stress-strain data suggested that the dislocation-induced shear was localized, which agrees with molecular dynamics (MD) simulations of fivefold twinned AgNWs[58]. Also, it was recently reported[29] that AgNWs greater than approximately *40 nm* in diameter exhibited brittle fracture with a size-independent stress-strain response under tensile and buckling modes. **Figure 3.8** shows the comparison between experimental and FEA average strain for both segments of NW #1. The same interface parameters were used in the simulations. The applied strain in the PDMS COMPOSITE at the end of the experiment was about *18%*. NW #1 segments did not suffer any further fracture as maximum average strain for both segments was less than *1%*, which leads to a smaller strain value than the fracture strain found in the first fracture. Also, the small size of the segments did not contribute to an efficient stress transfer from the PDMS COMPOSITE substrate. **Figure 3.S1(b)** shows an example of a fractured AgNW image taken by SEM.

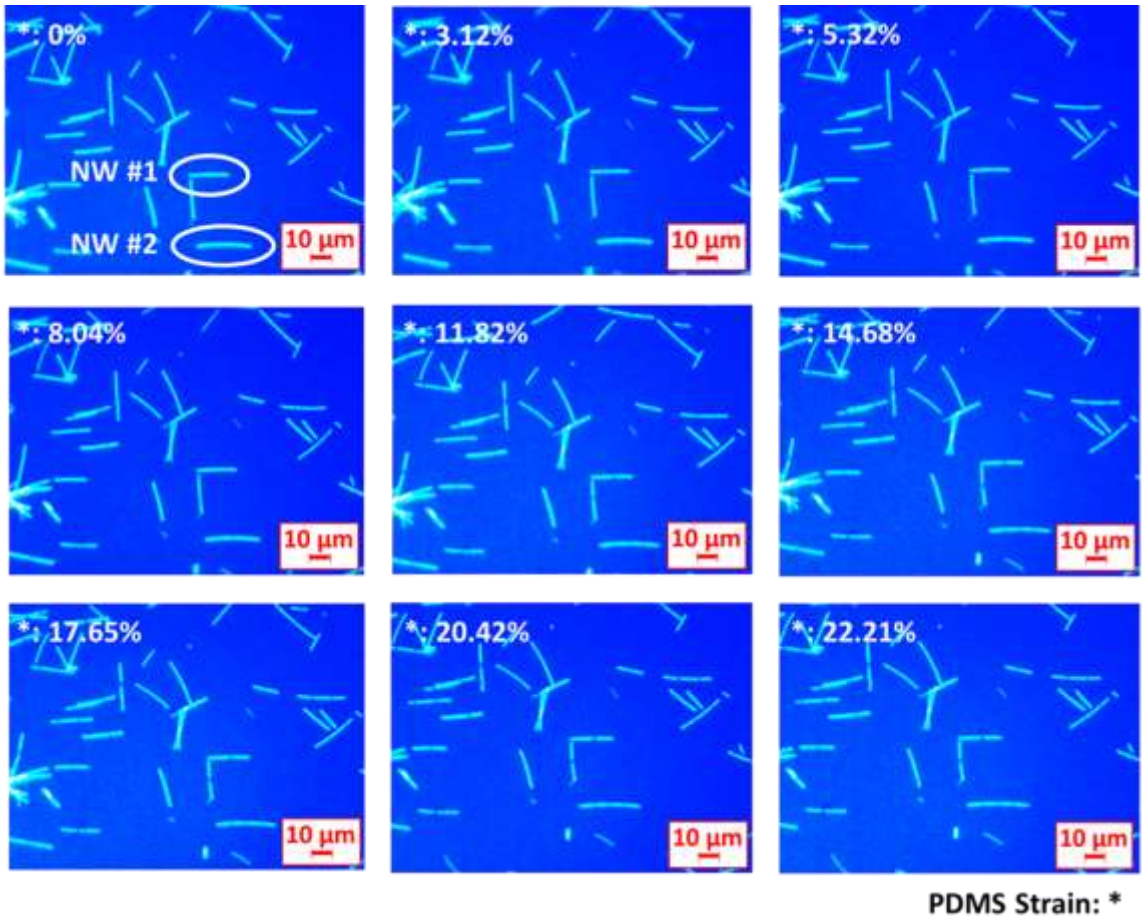

Figure 3.6 NW#1 and NW#2 placed on top of UVO-treated PDMS COMPOSITE substrate subjected to the tensile strain shown in the pictures.

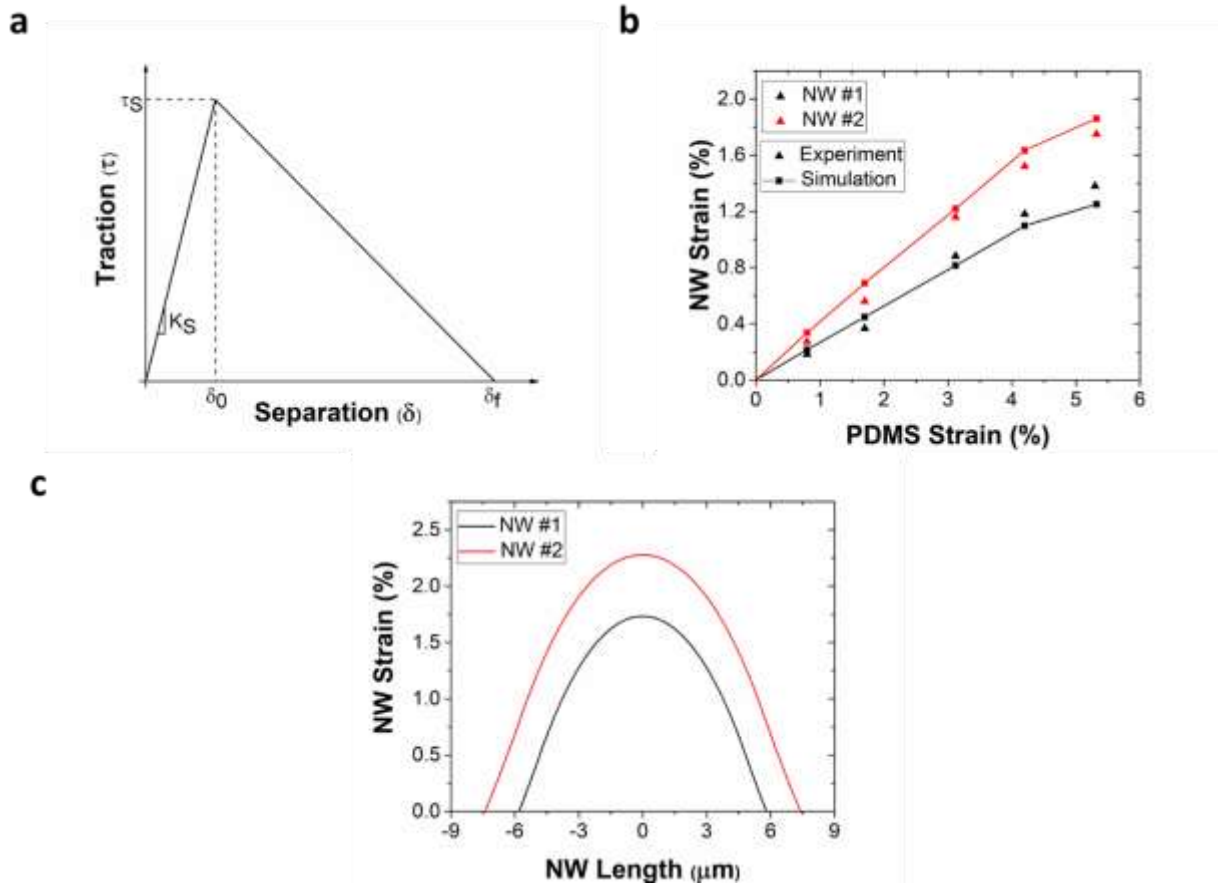

Figure 3.7 (a) Traction-separation law used in the FEA cohesive model for AgNW on top of UVO-treated PDMS COMPOSITE and (b) experimental vs. FEA results for the average strain in two different AgNWs on top of UVO-treated PDMS COMPOSITE.

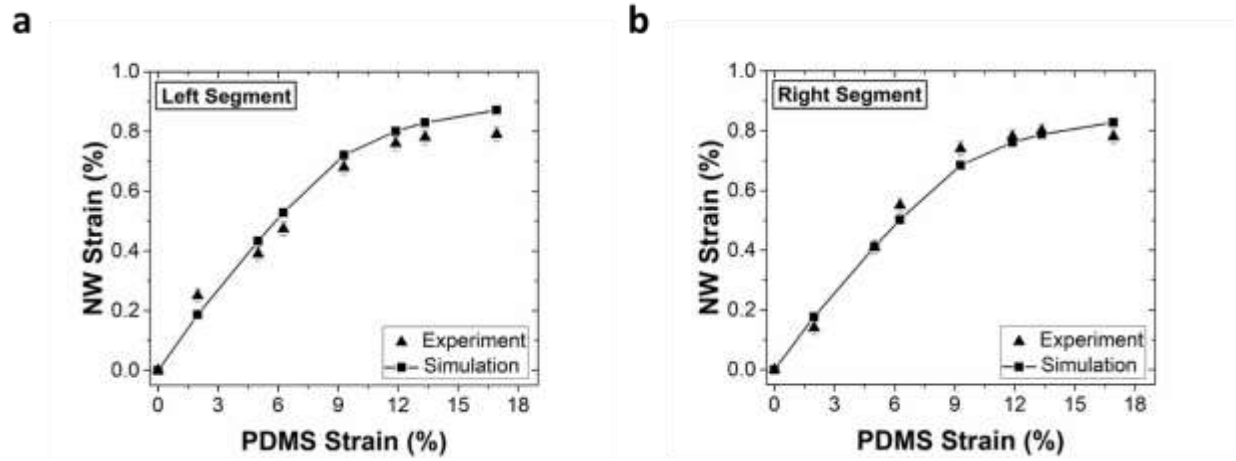

Figure 3.8 (a) Experimental vs. FEA results for the average strain for the left segment of AgNW #1 on top of UVO-treated PDMS COMPOSITE and (b) experimental vs. FEA results for the average strain for the right segment of AgNW #1 on top of UVO-treated PDMS COMPOSITE.

3.3.4 Fracture of AgNWs embedded UVO-treated PDMS COMPOSITE

An experiment was also conducted where the AgNW was embedded in an UVO-treated PDMS COMPOSITE substrate. In this case, the AgNW was embedded in between two halves of *45 min*. UVO-treated PDMS COMPOSITE substrates. The AgNW was placed parallel to the direction of the strain applied to the PDMS COMPOSITE. The main difference with respect when the AgNW is placed on top of a UVO-treated PDMS COMPOSITE substrate is that expected now the AgNW has a larger contact area with PDMS COMPOSITE, which would suggest that stress transfer from the substrate should be more efficient. **Figure 3.9** shows the fracture process of the AgNW picked to be analyzed (*20.5 μm* long and *30 nm* in radius). The experiments reported the breaking of the AgNW when its average strain was about *2.50%* and the applied strain on the PDMS COMPOSITE was *3.02%*. The FEA modeling considered the same materials properties and element types for both AgNW and PDMS COMPOSITE as previously used. The same traction-separation law parameters ($K_S = 140\ TPa/m$, $\tau_S = 24\ MPa$, and $G_S = 8\ N/m$) used in

the case of AgNW on top of UVO-treated PDMS COMPOSITE was employed. It was also assumed that the ends of the AgNW were traction-free. **Figure 3.10(a)** shows the comparison of the average strain in the AgNW from experiments and FEA simulation. The FEA analysis predicts an average strain in the AgNW of *2.40%* for the same applied strain on the PDMS COMPOSITE when the AgNW breaking was observed through the experiments. The smaller critical PDMS COMPOSITE strain value of *3%* when compared to the critical strain reported when the AgNW is on top of PDMS COMPOSITE has to do with the fact that there is a more efficient stress transfer when the AgNW is embedded in the substrate as the contact area now is larger. **Figure 3.10(b)** shows the strain distribution in the AgNW and it's noticed that the maximum strain reached at the center of the AgNW for the applied strain in PDMS COMPOSITE that causes it to break (*3.02%*) is *2.91%*. Again, this value is very close to the fracture strain reported in the literature of AgNWs[26,29] which is about *2-3%* strain. The two segments originated from the AgNW fracture were *9.87 μm* (left) and *11.23 μm* (right). Adding the segments together, it's concluded that the AgNW did not suffer plastic deformation which characterizes brittle fracture, similar to what was reported for AgNWs on top of UVO-treated PDMS COMPOSITE.

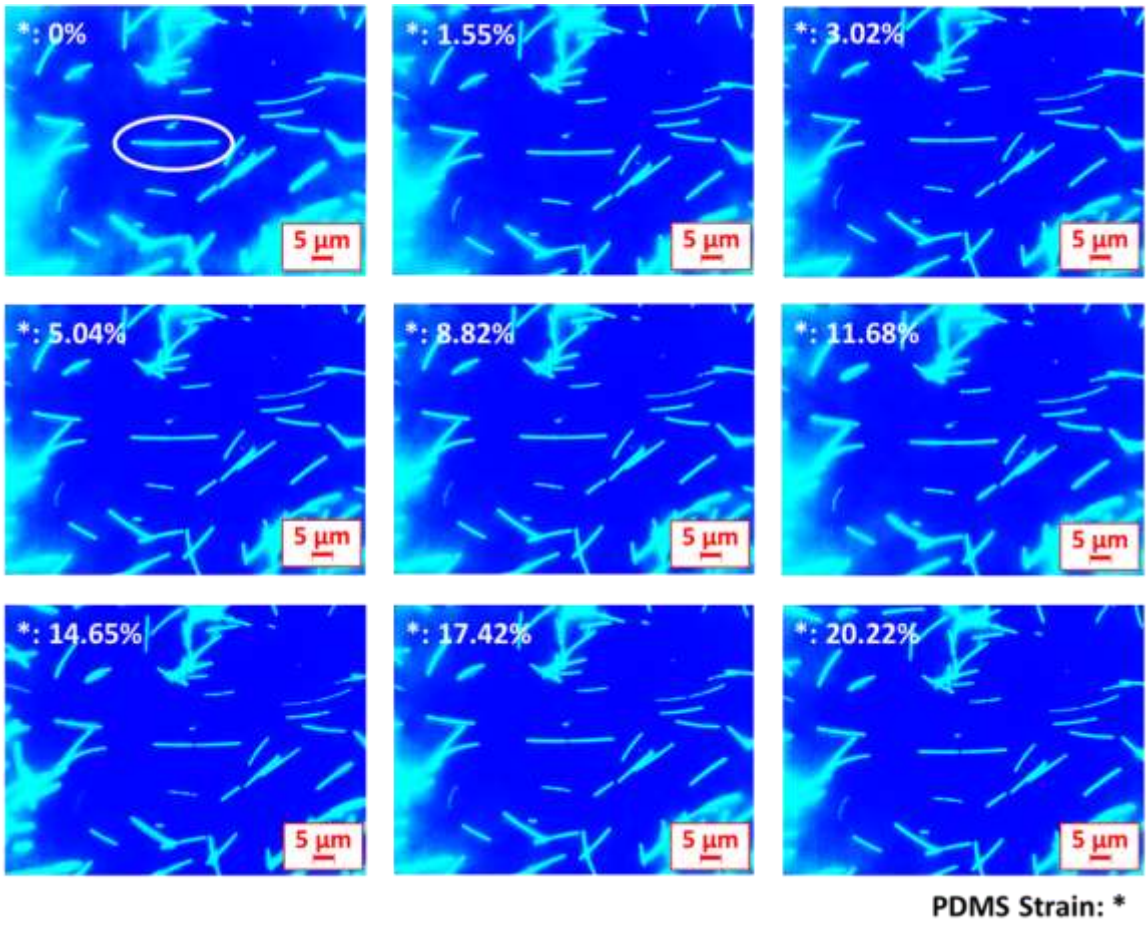

Figure 3.9 AgNW embedded in UVO-treated PDMS COMPOSITE substrate subjected to the tensile strain shown in the pictures.

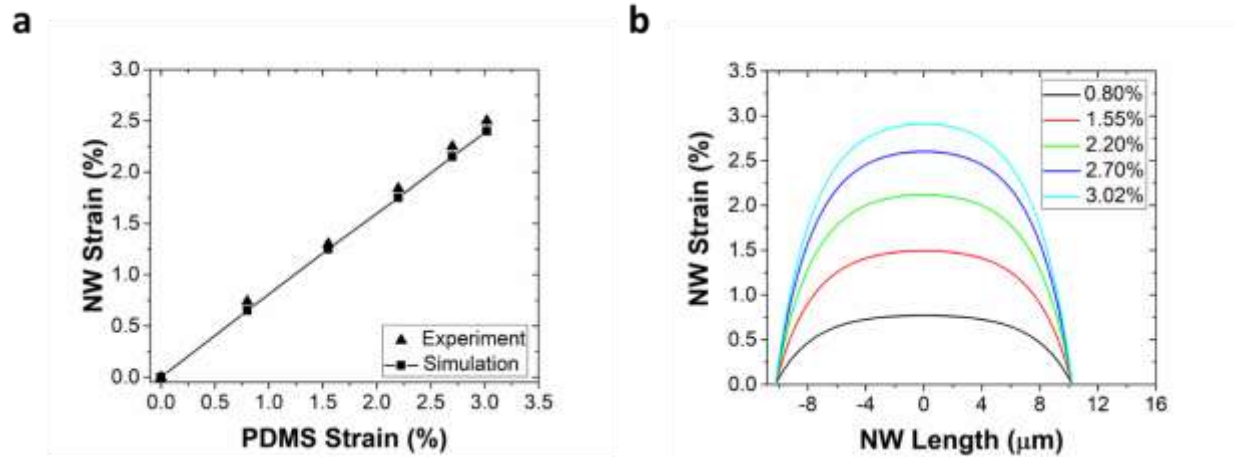

Figure 3.10 Experimental vs. FEA results for the average strain in an AgNW embedded in UVO-treated PDMS COMPOSITE.

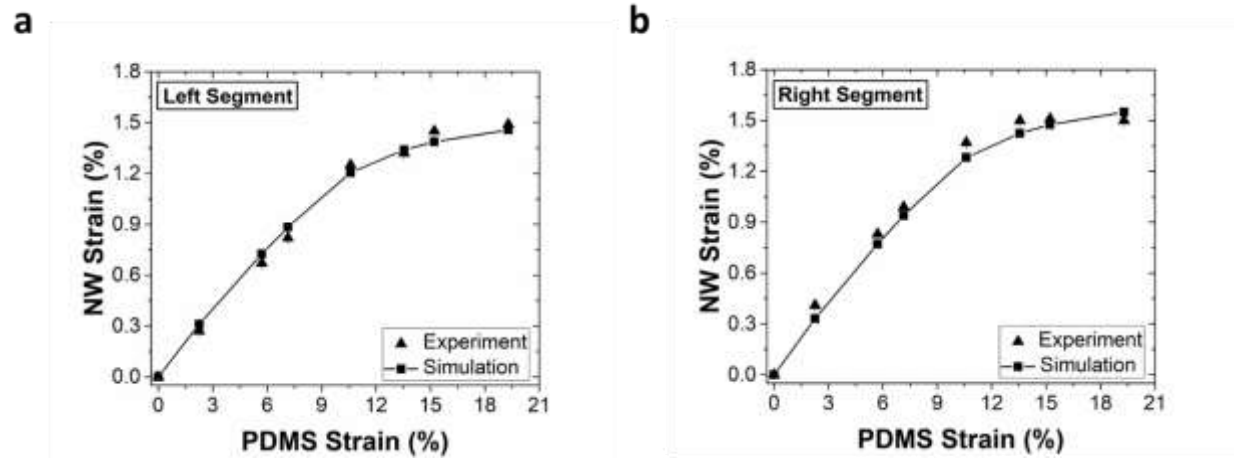

Figure 3.11 (a) Experimental vs. FEA results for the average strain for the left segment of an AgNW embedded in UVO-treated PDMS COMPOSITE and (b) experimental vs. FEA results for the average strain for the right segment of the same AgNW.

3.4 Conclusion

In this work, both buckling and fracture of AgNWs were studied taking into account the interface between AgNW and PDMS COMPOSITE. First, AgNWs on top of a pristine PDMS COMPOSITE and aligned to the direction of the applied strain in the substrate were considered. The covalent bonding between AgNW and pristine PDMS COMPOSITE, which is made of weak

dispersion forces, resulted in a lower stress transfer between them and a lower strain in the AgNW. For that reason, no fracture of AgNW could be observed. FEA modeling helped determine the interface parameters by fitting the FEA average strain with the experimental results ($K_S = 3.7\ TPa/m$ and $\tau_S = 1.2\ MPa$).

Buckling was studied by placing the AgNWs on top of a pristine PDMS COMPOSITE but perpendicular to the direction of applied strain in the substrate. Considering the AgNW as a slender beam on top of an elastic foundation, the critical NW buckling strain was calculated to be *0.21%*. FEA modeling was also used to predict the NW critical buckling strain, which is given by the peak strain value (in the center of the NW) in the strain distribution along the AgNW. The values found were close to the one analytically predicted. Also, in both experiments and FEA simulation, the buckling occurred in-plane. It has been reported that for SiNWs on top of PDMS COMPOSITE, the lateral in-plane buckling is more energetically favorable to occur than normal out-of-plane buckling.

After these experiments were conducted, the PDMS COMPOSITE substrate was subjected to a *45 min*. UVO-treatment in order to increase the bonding between AgNW and PDMS COMPOSITE. The chemical-type bonding that occurs when PDMS COMPOSITE is UVO-treated guarantees a more efficient stress transfer to the AgNWs. Because of that, AgNW fracture could be observed. Similar to the pristine PDMS COMPOSITE case, here also the interface parameters were derived based on the average strain fitting between experiment and FEA simulation ($K_S = 140\ TPa/m$, $\tau_S = 24\ MPa$, and $G_s = 8\ N/m$). Experiments and FEA simulations predicted a fracture strain of about *2%*, which is close to the values previously reported[25,28]. The length of the segments after the AgNW initial fracture when combined indicate that there was no presence of plastic deformation. These results agreed with the close analysis of fractured AgNWs broken by

tensile tests in an in-situ SEM nanomechanical setup[25], which revealed no apparent diameter reduction (i.e. no large-scale yielding) along the AgNW excerpt very close to the fracture surface. Also, it was reported[28] that AgNWs with diameter greater than 40 nm exhibited brittle fracture.

The findings presented in this work contribute to a better understanding of the interface mechanics between AgNW and PDMS COMPOSITE. It also provides information on critical buckling and fracture of AgNWs, which is critical in order to determine the reliability of devices that make use of such nanostructures. Both buckling and fracture of the AgNWs could cause problems when they are applied in flexible electronics. It was seen from the experiments that a strain level as low as *0.21%* could trigger AgNW buckling, which happens at the center of the AgNW. Further increasing the applied strain on PDMS COMPOSITE caused the fracture of the AgNW at that position due to the increase in buckling. UVO-treatment, which is generally used to improve the interface quality between nanomaterials and polymer substrates can also cause NW fracture as it was observed. Even though AgNWs have remarkable electrical properties, the strain levels that are applied to the substrate must be monitored in order to ensure that the device will continue to operate as expected. The experimental setup and FEA modeling can also be extended to the analysis of embedded NWs, which was demonstrated in the supporting material.

Supplementary Information (SI)

3.S1 SEM images of buckled and fractured AgNWs

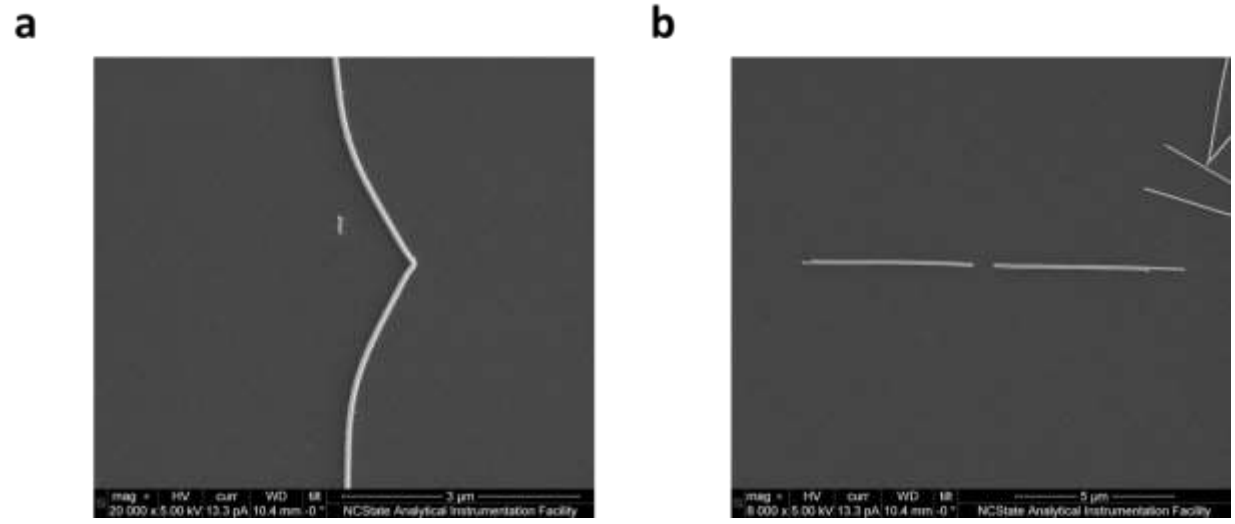

Figure 3.S1 (a) SEM image of a post-buckled AgNW on top of a pristine PDMS COMPOSITE and (b) SEM image of a fractured AgNW on top of a UVO-treated PDMS COMPOSITE.

REFERENCES

1. Fan, Z. Y., Ho, J. C., Takahashi, T., Yerushalmi, R., Takei, K., Ford, A. C., Chueh, Y. L., and Javey, A., 2009, Toward the Development of Printable Nanowire Electronics and Sensors. Adv. Mater., 21(37), pp. 3730–3743;
2. Ju, S., Facchetti, A., Xuan, Y., Liu, J., Ishikawa, F., Ye, P., Zhou, C., Marks, T. J., and Janes, D. B., 2007, Fabrication of Fully Transparent Nanowire Transistors for Transparent and Flexible Electronics. Nat. Nanotechnol., 2, pp. 378–384;
3. Xu, S., Qin, Y., Xu, C., Wei, Y., Yang, R., & Wang, Z. L., 2010, Self-powered nanowire devices. Nat. Nanotechnol, 5(5), 366;
4. Hammock, M. L., Chortos, A., Tee, B. C. K., Tok, J. B. H., & Bao, Z., 2013, 25th anniversary article: the evolution of electronic skin (e-skin): a brief history, design considerations, and recent progress. Adv. Mater., 25(42), 5997-6038;
5. Wu, B., Heidelberg, A., & Boland, J. J., 2005, Mechanical properties of ultrahigh-strength gold nanowires. Nat. Mater., 4(7), 525;
6. Xu, F., Wu, M. Y., Safron, N. S., Roy, S. S., Jacobberger, R. M., Bindl, D. J., ... & Arnold, M. S., 2014, Highly stretchable carbon nanotube transistors with ion gel gate dielectrics. Nano Lett., 14(2), 682-686;
7. Yang, C., Gu, H., Lin, W., Yuen, M. M., Wong, C. P., Xiong, M., & Gao, B., 2011, Silver nanowires: from scalable synthesis to recyclable foldable electronics. Adv. Mater., 23(27), 3052-3056;
8. Langley, D., Giusti, G., Mayousse, C., Celle, C., Bellet, D., & Simonato, J. P., 2013, Flexible transparent conductive materials based on silver nanowire networks: a review. Nanotechnology, 24(45), 452001;

9. Hecht, D. S., Hu, L., & Irvin, G., 2011, Emerging transparent electrodes based on thin films of carbon nanotubes, graphene, and metallic nanostructures. Adv. Mater., 23(13), 1482-1513;
10. De, S., & Coleman, J. N., 2011, The effects of percolation in nanostructured transparent conductors. Mrs Bulletin, *36*(10), 774-781;
11. Barnes, T. M., Reese, M. O., Bergeson, J. D., Larsen, B. A., Blackburn, J. L., Beard, M. C., ... & van de Lagemaat, J., 2012, Comparing the fundamental physics and device performance of transparent, conductive nanostructured networks with conventional transparent conducting oxides. Adv. Energy Mater., 2(3), 353-360;
12. Zeng, X. Y., Zhang, Q. K., Yu, R. M., & Lu, C. Z., 2010, A new transparent conductor: silver nanowire film buried at the surface of a transparent polymer. Adv. Mater., 22(40), 4484-4488;
13. Yu, Z., Zhang, Q., Li, L., Chen, Q., Niu, X., Liu, J., & Pei, Q., 2011, Highly flexible silver nanowire electrodes for shape-memory polymer light-emitting diodes. Adv. Mater., 23(5), 664-668;
14. Hu, W., Niu, X., Li, L., Yun, S., Yu, Z., & Pei, Q, 2012, Intrinsically stretchable transparent electrodes based on silver-nanowire–crosslinked-polyacrylate composites. Nanotechnology, 23(34), 344002;
15. Hu, W., Niu, X., Zhao, R., & Pei, Q., 2013, Elastomeric transparent capacitive sensors based on an interpenetrating composite of silver nanowires and polyurethane. Appl. Phys. Lett., 102(8), 38;

16. Xiao, J., Ryu, S. Y., Huang, Y., Hwang, K. C., Paik, U., & Rogers, J. A., 2010, Mechanics of nanowire/nanotube in-surface buckling on elastomeric substrates. Nanotechnology, *21*(8), 085708;
17. Ko, H. C., Stoykovich, M. P., Song, J., Malyarchuk, V., Choi, W. M., Yu, C. J., ... & Rogers, J. A., 2008, A hemispherical electronic eye camera based on compressible silicon optoelectronics. Nature, 454(7205), 748;
18. Nolte, A. J., Rubner, M. F., & Cohen, R. E., 2005, Determining the Young's modulus of polyelectrolyte multilayer films via stress-induced mechanical buckling instabilities. Macromolecules, 38(13), 5367-5370;
19. Lacour, S. P., Jones, J., Wagner, S., Li, T., & Suo, Z., 2005, Stretchable interconnects for elastic electronic surfaces. Proceedings of the IEEE, 93(8), 1459-1467;
20. Zhao, Y., Li, J., Cao, Y. P., & Feng, X. Q., 2016, Buckling of an elastic fiber with finite length in a soft matrix. Soft Matter., 12(7), 2086-2094;
21. Ryu, S. Y., Xiao, J., Park, W. I., Son, K. S., Huang, Y. Y., Paik, U., & Rogers, J. A., 2009, Lateral buckling mechanics in silicon nanowires on elastomeric substrates. Nano Lett., 9(9), 3214-3219;
22. Khang, D. Y., Xiao, J., Kocabas, C., MacLaren, S., Banks, T., Jiang, H., ... & Rogers, J. A., 2008, Molecular scale buckling mechanics in individual aligned single-wall carbon nanotubes on elastomeric substrates. Nano Lett., 8(1), 124-130;
23. Su, T., Liu, J., Terwagne, D., Reis, P. M., & Bertoldi, K., 2014, Buckling of an elastic rod embedded on an elastomeric matrix: planar vs. non-planar configurations. Soft Matter., 10(33), 6294-6302;

24. Wu, B., Heidelberg, A., Boland, J. J., Sader, J. E., Sun, X., & Li, Y., 2006, Microstructure-hardened silver nanowires. Nano Lett., *6*(3), 468-472;

25. Lucas, M., Leach, A. M., McDowell, M. T., Hunyadi, S. E., Gall, K., Murphy, C. J., & Riedo, E., 2008, Plastic deformation of pentagonal silver nanowires: comparison between AFM nanoindentation and atomistic simulations. Phys. Rev. B, 77(24), 245420;

26. Zhu, Y., Qin, Q., Xu, F., Fan, F., Ding, Y., Zhang, T., ... & Wang, Z. L, 2012, Size effects on elasticity, yielding, and fracture of silver nanowires: In situ experiments. Phys. Rev. B, 85(4), 045443;

27. Wu, H. A., Soh, A. K., Wang, X. X., & Sun, Z. H., 2004, Strength and fracture of single crystal metal nanowire. Key Eng. Mater. (Vol. 261, pp. 33-38). Trans Tech Publications;

28. Ho, D. T., Im, Y., Kwon, S. Y., Earmme, Y. Y., & Kim, S. Y., 2015), Mechanical failure mode of metal nanowires: global deformation versus local deformation. Sci. Rep., *5*, 11050;

29. Kim, D., Kim, S. H., Kim, J. H., Lee, J. C., Ahn, J. P., & Kim, S. W, 2017, Failure criterion of silver nanowire electrodes on a polymer substrate for highly flexible devices. Sci. Rep., *7*, 45903;

30. Xu, F., Lu, W., and Zhu, Y., 2011, Controlled 3D Buckling of Silicon Nanowires for Stretchable Electronics. ACS Nano, 5(1), pp. 672–678;

31. Qin, Q. Q., and Zhu, Y., 2011, Static Friction Between Silicon Nanowires and Elastomeric Substrates. ACS Nano 5(9), pp. 7404–7410;

32. Chen, Y., Zhu, Y., Chen, X., and Liu, Y., 2016, Mechanism of the Transition From In-Plane Buckling to Helical Buckling for a Stiff Nanowire on an Elastomeric Substrate. ASME J. Appl. Mech., 83(4), p. 041011;

33. Chen, Y., Liu, Y., Yan, Y., Zhu, Y., and Chen, X., 2016, Helical Coil Buckling Mechanism for a Stiff Nanowire on an Elastomeric Substrate. J. Mech. Phys. Solids, 95, pp. 25–43;
34. Kokorian, J., Buja, F., van Spengen, W. M., 2015, In-plane displacement detection with picometer accuracy on a conventional microscope. J. of Microelectromech. Syst., 24(3), 618-625;
35. Lawrence, E. M., Speller, K. E., & Yu, D., 2003, MEMS characterization using laser Doppler vibrometry. In Reliability, Testing, and Characterization of MEMS/MOEMS II. International Society for Optics and Photonics, 4980, 51-63;
36. Hart, M. R., Conant, R. A., Lau, K. Y., Muller, R. S., 2000, Stroboscopic interferometer system for dynamic MEMS characterization. Journal of Microelectromech. Syst., 9(4), 409-418;
37. Bosseboeuf, A., & Petitgrand, S., 2003, Characterization of the static and dynamic behaviour of M (O) EMS by optical techniques: status and trends. Journal Micromechanics Microengineering, 13(4), S23;
38. Serio, B., Hunsinger, J. J., & Cretin, B., 2004, In-plane measurements of microelectromechanical systems vibrations with nanometer resolution using the correlation of synchronous images. Rev. Sci. Instrum., 75(10), 3335-3341;
39. Ya'akobovitz, A., Krylov, S., & Hanein, Y. (2010). Nanoscale displacement measurement of electrostatically actuated micro-devices using optical microscopy and digital image correlation. Sens. Actuators, A, 162(1), 1-7;
40. Peters, W. H., & Ranson, W. F., 1982, Digital imaging techniques in experimental stress analysis. Opt. Eng., 21(3), 213427;

41. Yang, F., He, X., & Quan, C., 2006, Characterization of dynamic microgyroscopes by use of temporal digital image correlation. Appl. Opt., 45(30), 7785-7790;
42. Hung, P. C., & Voloshin, A. S., 2003, In-plane strain measurement by digital image correlation. J. Braz. Soc. Mech. Sci., 25(3), 215-221;
43. Van Paepegem, W., Shulev, A. A., Roussev, I. R., De Pauw, S., Degrieck, J., & Sainov, V. C., 2009, Study of the deformation characteristics of window security film by digital image correlation techniques. Opt. Lasers Eng., 47(3-4), 390-397;
44. Bruck, H. A., McNeill, S. R., Sutton, M. A., & Peters, W. H., 1989, Digital image correlation using Newton-Raphson method of partial differential correction. Exp. Mech., 29(3), 261-267;
45. Vendroux, G., & Knauss, W. G., 1998, Submicron deformation field measurements: Part 2. Improved digital image correlation. Exp. Mech., 38(2), 86-92;
46. https://www.mathworks.com/matlabcentral/fileexchange/12413-digital-image-correlation-and-tracking
47. Jiang, L. Y., Huang, Y., Jiang, H., Ravichandran, G., Gao, H., Hwang, K. C., & Liu, B., 2006, A cohesive law for carbon nanotube/polymer interfaces based on the van der Waals force. J. Mech. Phys. Solids, 54(11), 2436-2452;
48. Alfano, G., 2006, On the influence of the shape of the interface law on the application of cohesive-zone models. Compos. Sci. Technol., 66(6), 723-730;
49. Needleman, A., 1990, An analysis of tensile decohesion along an interface. J. Mech. Phys. Solids, 38(3), 289-324;
50. Robles Poblete, F., Xu, F., Zhu, Y., 2018, Interfacial stress transfer between a single nanowire and a stretchable substrate. Unpublished manuscript;

51. Zhu, Y., Qin, Q., Xu, F., Fan, F., Ding, Y., Zhang, T., ... & Wang, Z. L., 2012, Size effects on elasticity, yielding, and fracture of silver nanowires: In situ experiments. Phys. Rev. B, 85(4), 045443;
52. She, H., Malotky, D. and Chaudhury, M.K., 1998, Estimation of adhesion hysteresis at polymer/oxide interfaces using rolling contact mechanics. Langmuir, 14(11), pp.3090-3100;
53. Sneddon, I. N., 1965, The relation between load and penetration in the axisymmetric Boussinesq problem for a punch of arbitrary profile. Int. J. Eng. Sci., *3*(1), 47-57;
54. Johnston, I. D., McCluskey, D. K., Tan, C. K. L., & Tracey, M. C., 2014, Mechanical characterization of bulk Sylgard 184 for microfluidics and microengineering. J. Micromechanics Microengineering, 24(3), 035017;
55. Israelachvili, J.N., 2011. Intermolecular and surface forces. Academic press;
56. Jiang, T., Huang, R., & Zhu, Y., 2014, Interfacial sliding and buckling of monolayer graphene on a stretchable substrate. Adv. Funct. Mater., 24(3), 396-402;
57. Sun, Y., & Rogers, J. A., 2007, Structural forms of single crystal semiconductor nanoribbons for high-performance stretchable electronics. J. Mater. Chem., 17(9), 832-840;
58. Leach, A. M., McDowell, M., & Gall, K., 2007, Deformation of Top-Down and Bottom-Up Silver Nanowires. Adv. Funct. Mater., *17*(1), 43-53.

CHAPTER 4 Study of Al_2O_3 and ZnO nanopillars under nanoindentation

4.1 Introduction

The composition and architectural arrangement of constituent elements at the micro/nano-scale of naturally occurring cellular materials is reported to be responsible for improved stiffness modulus, strength, and energy absorption in these materials. That's why biological exoskeletons[1-4], bones[5], cork, and wood[6] are lightweight while at the same time exhibiting superior mechanical properties. As a result, many engineered cellular materials such as metal[7,8] and polymer foams[9-11] were developed by researchers. Although these materials have found many applications such as thermal insulation[11,12,13] and shock absorption[14,15] due to their increased surface area and extremely low density, it can be difficult to precisely control the architectural arrangement as many of these materials have micro/nano-scale geometrical constituent elements that are randomly oriented. Also, porous cellular materials with random architectures are mechanically less durable at low densities.

In order to circumvent the degradation of these materials, considerable research has been conducted in lightweight structures with a more favorable density scaling, which has been achieved by having an ordered arrangement of constituent elements resulting in significantly improved mechanical properties for porous materials[15-17]. The constituent elements can also be made hollow to achieve ultra-low density, while maintaining similar enhanced scaling. These architectural arrangements have produced structures with remarkable materials properties such as energy dissipation[18,19], negative Poisson's ratio[20], ductile-like recoverability and high stretchability[17].

Bearing that in mind, an ordered 3D nanolattice film with enhanced mechanical properties for normal compressive loading was fabricated via 3D colloidal nanolithography. Another

advantages of this material include near-linear modulus scaling with density, high specific energy dissipation, and near-complete material recovery for the thinnest shells ($t < 10\,mm$). Besides these novel mechanical properties, the nanolattice film has demonstrated refractive index very close to air and such highly porous material can also have dielectric constant and thermal conductivity very close to air, which gives it potential application as a multifunctional insulating film.

In this work, aluminum oxide (Al_2O_3) and zinc oxide (ZnO) were selected to fabricate the nanolattice films due to their attractive bulk properties. The mechanical properties of both nanolattice films were tested by applying uniaxial compressive loading through nanoindentation. FEA modeling was used to analyze energy absorption of the nanolattice material. Nanoindentation experiments were also conducted in order to investigate the anelastic behavior of these materials. Anelastic materials exhibit gradual full recovery of deformation once a load is removed, leading to dissipation of internal mechanical energy[21]. ZnO single crystal nanowires have presented such behavior[22]. In fact, single-crystalline materials reportedly have shown anelastic mechanisms such as thermoelastic relaxation, piezoelectric coupling, and relaxations involving point defect motion[21,23,24]. FEA modeling was also employed to model the anelastic response of the nanolattice films under nanoindentation.

4.2 Compressive experiments by nanoindentation

Al_2O_3 and ZnO samples were patterned using a periodic 3D photoresist template using colloidal phase lithography[25] and atomic layer deposition (ALD). More details on the nanolattice fabrication can be seen in the published results[26]. As seen from the cross-sectional SEM images in **Figure 4.1**, the nanolattice arrangement consists of vertically aligned thin-shell tubular columns with secondary interconnect structures in between. This unique ordered arrangement of thin-shell

tubular columns results in enhanced mechanical properties under compressive loading. Due to the impossibility of fabricating thinner ZnO nanolattice shells[26], ZnO thicker samples were developed (*95*, *45*, and *30 nm*-thick samples as shown in **Figure 4.1(a-c)**). In contrast, Al_2O_3 nanolattice films were fabricated with thinner shells (*19*, *10*, and *4 nm*-thick samples as shown in **Figure 4.1(d-f)**).

The mechanical properties of both nanolattice films were tested by applying uniaxial compressive loading through nanoindentation experiments. In these tests, a spherical diamond indenter with *10 μm* radius was applied with a predefined load on the nanolattice film. The indenter had a contact area spanning over a few unit cells, which ensures that the applied load predominantly acts normal to the sample surface and the nanolattice film behaves like a continuum material. Nanoindentation characterization was performed by a cyclic incremental loading scheme, which helped to determine indentation modulus prior to "pop-in" events that signify mechanical failure by either yielding, buckling or fracture. **Figure 4.2** shows cyclic loading-displacement curves from Al_2O_3 and ZnO samples of different thicknesses. After the structure collapse at the 'pop-in' event, the nanolattice densifies and the architectural arrangement of the structure changes, which will affect the mechanical properties of the structure during subsequent incremental loading cycles. To avoid this effect, only the cycles before the 'pop-in' event were considered for calculating modulus, hardness, and the energy dissipation. To get reliable data for mechanical properties, each nanolattice sample was tested at multiple locations.

The non-linear nanoindentation response in the later loading-unloading cycles results from elastic-plastic deformation of the nanolattice film. During unloading, the elastic work done is released by partial recovery of the nanolattice, but the plastic work done will be dissipated through localized, permanent deformations of the structure. **Figure 4.3** plots the dissipated energy per weight by Al_2O_3 and ZnO nanolattices as a function of relative density before the 'pop-in' event.

As expected, the thicker structures dissipate higher total energy before collapse. Specific energy dissipation, calculated by normalizing the total energy by the weight of the solid phase, can be examined to evaluate effectiveness for light-weight applications. Energy dissipated by the nanolattice film was the plastic work done on the structure during compressive loading. To calculate the specific energy dissipation by nanolattice film, the plastic work done in all the loading cycles before 'pop-in' was added together to get the cumulative plastic work. This cumulative plastic work was then divided by the total volume (V) displaced by the spherical nanoindenter during loading to calculate energy dissipation per unit volume (J/mm3). To accurately analyze the energy absorbing properties of the nanolattice material, the total failure volume zone within the lattice during nanoindentation was evaluated by finite element modeling of the nanolattice. This volume is important in estimating the specific energy dissipation, since the inelastic energy of the nanolattice material from the force-displacement curve is attributed to irreversible damage within the lattice film elements.

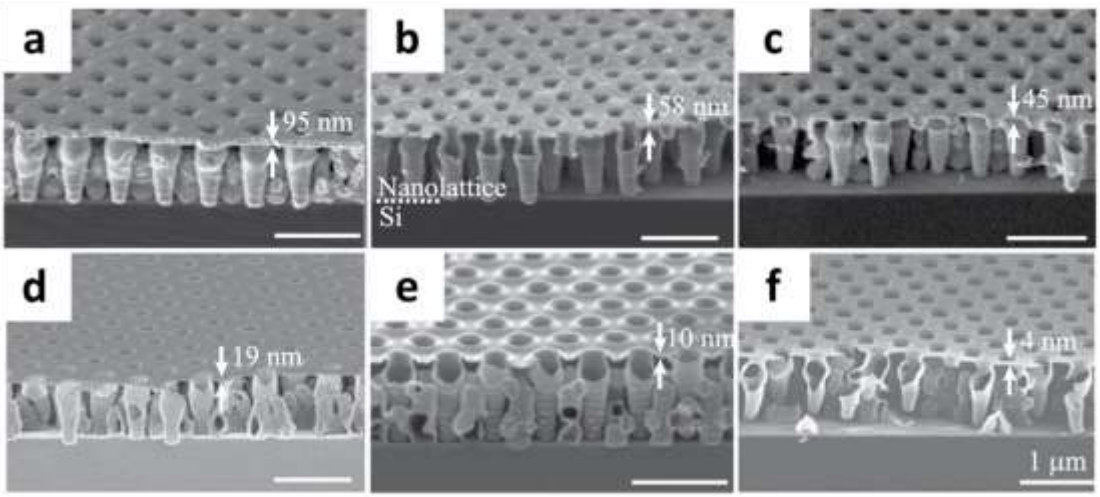

Figure 4.1 Scanning electron micrographs of samples used for mechanical testing. (a-c) Cross-sectional image of ZnO nanolattices with thicknesses 95 nm, 58 nm, and 45 nm respectively. (d-f) Cross-sectional SEM image of Al_2O_3 nanolattices with thicknesses 19 nm, 10 nm, 4 nm respectively. The thinnest nanolattice tested for mechanical properties had a shell thickness of 4 nm. Cross-sectional image of 4 nm nanolattice shows the structure is free-standing and does not collapse during template removal process.

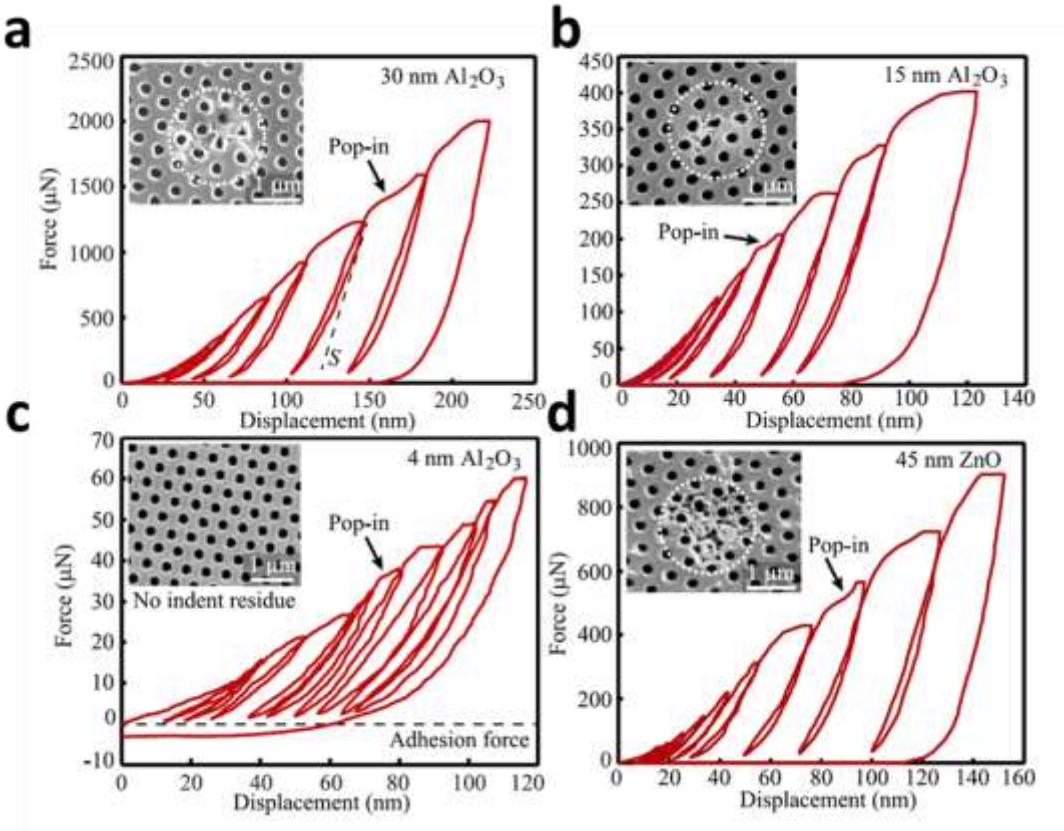

Figure 4.2 Mechanical testing of nanolattice using nanoindentation. (a) Typical cyclic load-displacement curve for 30 nm Al_2O_3 nanolattice. 'Pop-in' indicates first instance of mechanical failure of nanolattice film. Inset shows post-indent SEM image with residual indentation imprint, showing brittle fracture of top planar layer. (b) Load-displacement curve for 15 nm Al_2O_3 nanolattice showing similar loading-unloading behavior as 30 nm Al_2O_3 nanolattice. This is the thinnest sample tested which failed by fracture of top planar layer. (c) Load-displacement curve for 4 nm Al_2O_3 nanolattice showing gradual 'pop-in' event. Inset shows post-indent SEM with no residual indentation imprint. Non-zero adhesion force from van der Waal's attraction between the diamond indent and Al_2O_3 nanolattice indicate near-complete recovery post indentation. (d) Load-displacement curve for 45 nm ZnO nanolattice showing 'pop-in' event similar to thicker Al_2O_3 nanolattice. Inset shows post indent SEM image with brittle fracture around holes.

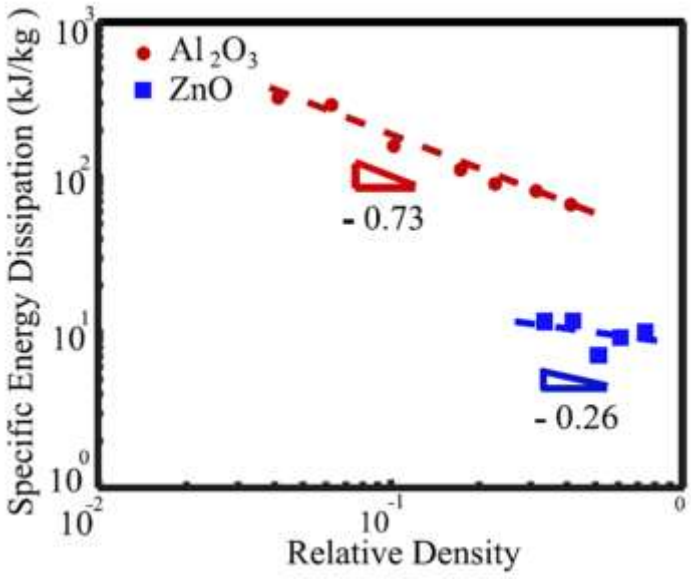

Figure 4.3 Specific energy dissipation for Al_2O_3 and ZnO nanolattice plotted against relative density. The Al_2O_3 nanolattice shows more favorable power law scaling.

4.3 FEA modeling of nanoindentation

Three-dimensional (3D) finite element analysis (FEA) of the indentation of Al_2O_3 and ZnO nanostructures were carried out in Abaqus 6.14. The nanolattice structure was modeled as a plate supported by thin-shell hollow pillars with average radius of *125 nm* in a square lattice with spacing of *500 nm*. The 3D FEA model is illustrated in **Figure 4.4**. A quarter of the nanolattice structure was modeled in view of the 4-fold symmetry of the structure. For both Al_2O_3 and ZnO nanostructures, isotropic linear elastic behaviors and 20-node quadratic brick with reduced integration elements (C30D20R) were used. The mechanical properties of the individual shell elements are based on experimental values reported in literature. For Al_2O_3, a Young's modulus of *180 GPa* and a Poisson's ratio of *0.24* were assigned[27] whereas for ZnO, a Young's modulus of *146 GPa* and a Poisson's ratio of *0.30*.[28] The shell thicknesses of both structures were varied to reflect the fabricated structures. The indenter tip was modeled as an analytical rigid structure with a diameter of *20 μm*. In each simulation, distribution of the maximum principal strain was

recorded. To calculate the energy dissipation, the volume in which the maximum principal strain is equal or above the critical strain value was used.

Representative results from the FEA simulations are shown for *10* and *40 nm* thick Al_2O_3 structure are shown in **Figure 4.5**. **Figure 4.5(a)** and **(c)** depict maximum principal strain contours at the maximum indentation depth of *80.23* and *82.32 nm* for the *10* and *40 nm* samples, respectively. To obtain the volume, the nanolattice model was subjected to the same indentation depth used in the experiments. **Figure 4.5(b)** and **(d)** depict the volume where the local strain exceeds the critical strain of *2* and *1.05%* for the *10* and *40 nm* samples, respectively. The total volume was multiple by a factor of *4* to calculate the total failure volume. Buckling was observed for Al_2O_3 structures with thickness below *30 nm*. For these cases, in order to avoid convergence issues, artificial damping was added to the model. It was assured that the ratio between the artificial damping energy and the strain energy of the model was no more than *5%*. A table summarizing the FEA simulation results for all samples are shown below in **Table 4.1**.

The specific energy dissipation for a nanolattice was calculated by dividing the energy dissipation per volume by samples density. For *4 nm* Al_2O_3 nanolattice, the averaged value of contact depth was *91.78 nm* at *50 μN* load, for which the total deformed volume from FEA was calculated to be $0.28*10^8\ nm^3$. The load-displacement curves for all the nanolattice samples show hysteresis during cyclic loading of the samples. This hysteresis over-predicts the plastic work done during each cycle, and are corrected by removing the hysteresis area when calculating the energy dissipation calculation for all the nanolattice samples. **Figure 4.6** shows the representative hysteresis loops before pop-in for the load-displacement curve of *4 nm* Al_2O_3 nanolattice shown in **Figure 4.2(c)**. The hysteresis error was in the range of *6.01 – 17.41%* for all the samples. The

corrected averaged cumulative plastic work for 4 nm nanolattice was *1.16 pJ*. Therefore the energy dissipated per volume by *4 nm* Al_2O_3 nanolattice is:

$$Energy\ dissipation\ per\ volume = \frac{W_p}{V} = 41.43 * 10^3\ \ kJ/m^3 \quad \textbf{(4.1)}$$

The specific energy dissipated by *4 nm* Al2O3 nanolattice was calculated by dividing the energy dissipation per volume by its density (*127.6 kg/m*^{3}).

$$Specific\ energy\ dissipation = \frac{41.43*10^3}{127.6} = 325.5\ \ kJ/kg \quad \textbf{(4.2)}$$

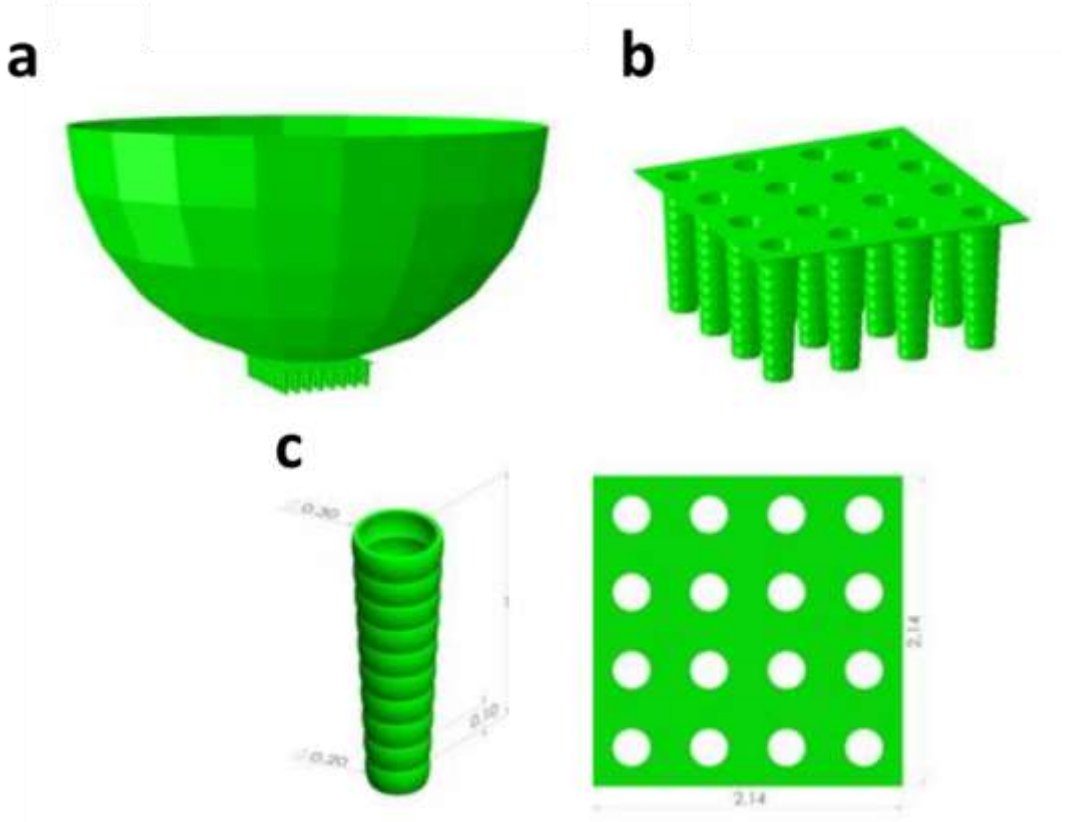

Figure 4.4 Nanolattice indentation modeled in FEA showing (a) the indenter tip positioned over the entire nanolattice, (b) actual nanolattice model analyzed considering a quarter symmetry, and (c) basic structure dimensions. The dimensions are in μm.

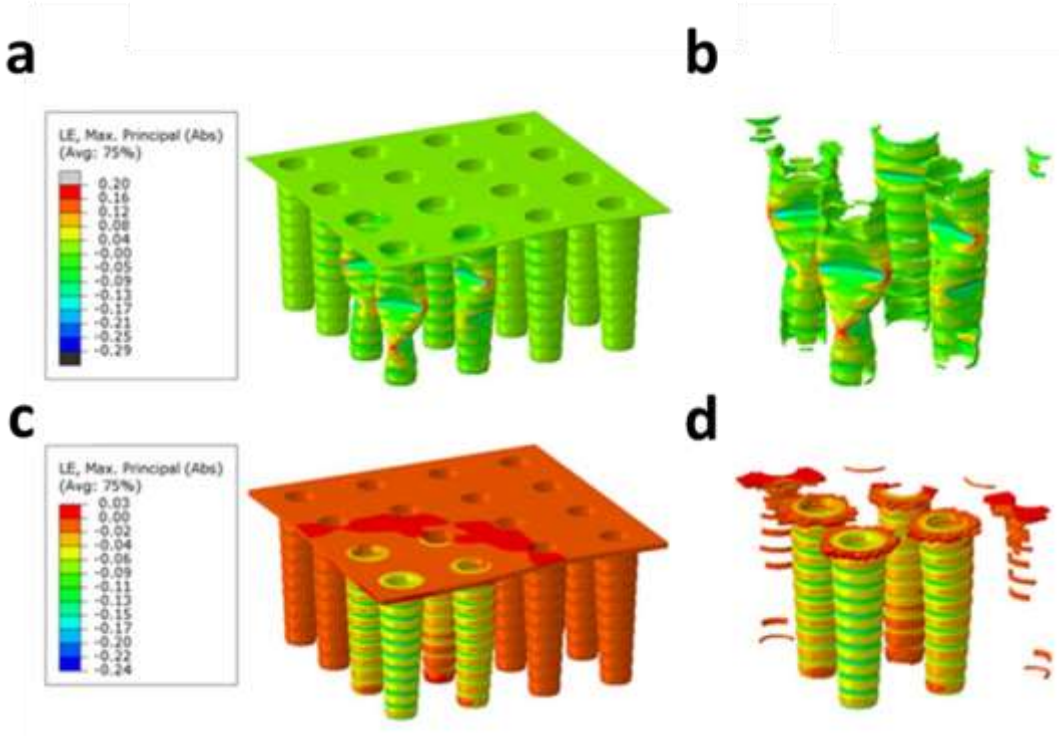

Figure 4.5 Maximum principal strain for the 10 nm and 40 nm thick Al_2O_3 structure. (a) Strain distribution across the entire 10 nm thick structure. (b) Part of the structure above the critical strain value for the 10 nm thick structure. (c) Strain distribution across the entire 40 nm thick structure. (d) Part of the structure above the critical strain value for the 40 nm thick structure.

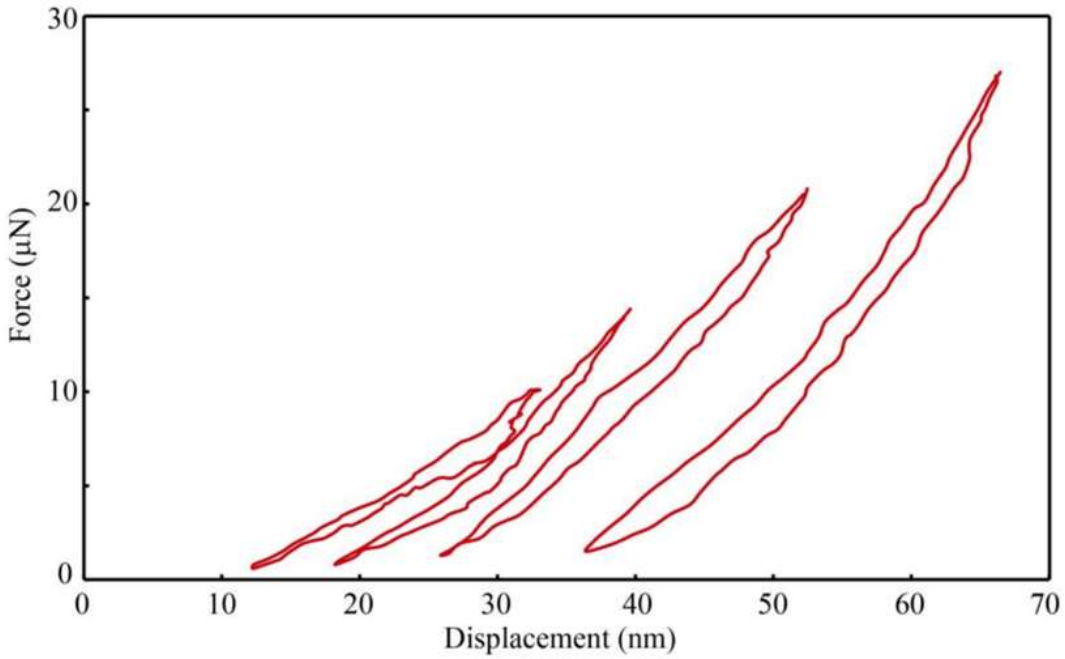

Figure 4.6 Hysteresis loops for 4 nm Al_2O_3 nanolattice.

Table 4.1 FEA Calculation of failure volume zone of nanolattice films.

Shell thickness (nm)		Indentation Depth (nm)	FEA Volume (μm^3)	Critical Compressive Strain (%)	Critical Tensile Strain (%)
Al_2O_3	**4**	91.78	0.028	2	2.41
	6	86.78	0.05	2	2.41
	10	80.23	0.10	2	1.62
	15	62.97	0.12	2	1.40
	20	97.29	0.28	2	1.19
	30	83.61	0.38	1.03	1.16
	40	82.32	0.50	1.05	0.95
ZnO	**30**	72.59	0.28	2	2
	45	96.61	0.56	2	2
	58	52.96	0.32	2	2
	75.5	83.73	0.71	2	2
	95	74.73	0.74	2	2

4.4 Anelasticity experiment

Nanoindentation tests were performed at room temperature by the same nanoindenter used in the previous tests (CSM Ultra Nanoindentation Tester). The sample tested was a *30 nm* Al_2O_3 nanolattice. According to **Figure 4.7**, a loading force of *500 µN* at a *800 µN/min* rate was applied and kept constant for *120 seconds*. After that, the load was reduced at the same rate to *10 µN* and kept constant for another *120 seconds*. The load could not be completely removed due to artifact interference from the system measurements.

Measurements were taken at several locations and an average force-displacement curve could be derived from the data. **Figure 4.8** shows the curve with three important values highlighted in it. The average loading indentation displacement (a) was *14.6 nm*, the average instant recovery displacement (b) was *63.6 nm*, and the average unloading relaxation displacement (c) was *9.1 nm*. Results showed that the Al_2O_3 nanolattice do present anelastic behavior even though the relaxation displacement is smaller than the loading displacement.

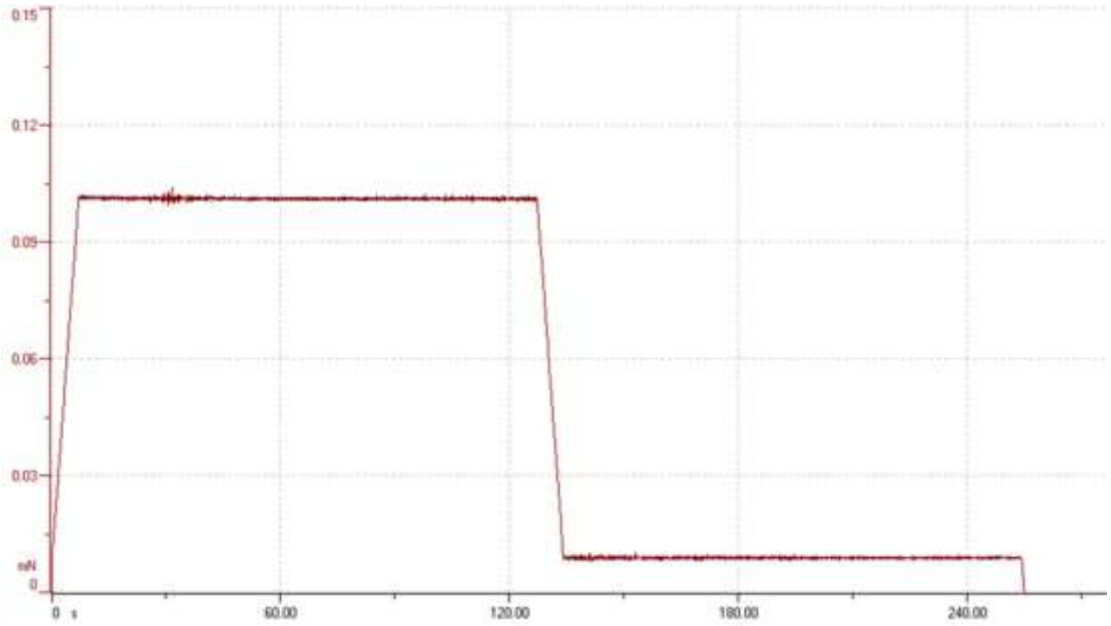

Figure 4.7 Loading history applied during the nanoindentation experiment to investigate the anelasticity behaviour of Al_2O_3 nanolattice films.

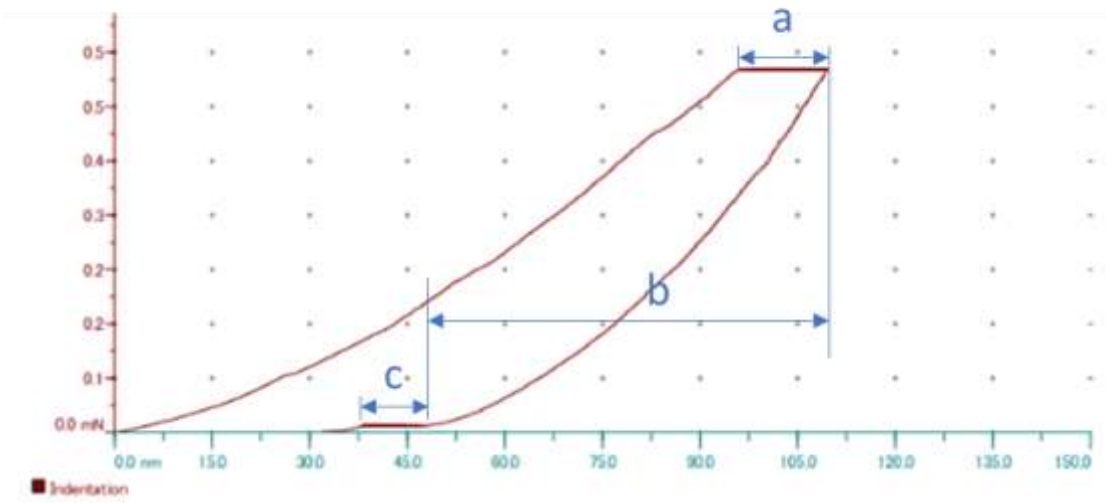

Figure 4.8 Average force-displacement resultant from the nanoindentation experiment to investigate the anelasticity behaviour of Al_2O_3 nanolattice films. Results show the average loading indentation displacement (a) was 14.6 nm, the average instant recovery displacement (b) was 63.6 nm, and the average unloading relaxation displacement (c) was 9.1 nm.

4.5 FEA modeling of anelasticity experiments

The theoretical model of anelasticity used in the analysis was developed in the analysis of ZnO nanowires[22]. Basically, this behavior was modeled through a theoretical framework by point defect diffusion under a high strain gradient and short diffusion distance, expanding the classic Gorsky theory. The time-dependent evolution of the concentration is given by:

$$\frac{\partial c_i}{\partial t} = D_i \frac{\partial}{\partial x}\left(\frac{\partial c_i}{\partial t} + \frac{1}{3}\frac{E\Omega_i c_i}{RT}\sum_{j=1,2\ldots n}\frac{1}{3}\Omega_j \frac{\partial c_j}{\partial x}\right) + D_i \frac{\partial}{\partial y}\left[\frac{\partial c_i}{\partial t} - \frac{1}{3}\frac{E\Omega_i c_i}{RT}\left(\kappa - \sum_{j=1,2\ldots n}\frac{1}{3}\Omega_j \frac{\partial c_j}{\partial x}\right)\right] \quad \textbf{(4.3)}$$

where c_i is the concentration of defect type i, $D_i = M_i RT$ is the diffusivity coefficient of defect type i, and κ is the curvature of the nanopillar.

The curvature of the nanopillar was then updated by the following equation:

$$\kappa = \kappa_e + \frac{16}{5\sqrt{3}h^4}\iint_D \sum_{i=1,2\ldots n}\frac{1}{3}\Omega_i c_i y dx dy \quad \textbf{(4.4)}$$

Differential **Equation (4.3)** was solved by assuming the defects are initially uniformly distributed throughout the structure, i.e.

$$c_i = c_i^0 \; at \; t = 0 \qquad \textbf{(4.5)}$$

The nonlinear partial differential **Equation (4.3)** was solved by COMSOL Multiphysics code in a general PDE mode. The force-extension curve obtained was compared with the experimental results. The first part of the simulation consisted in loading a *30 nm* Al_2O_3 nanolattice up to the same deformation depth obtained in the experiments, which was around *90 nm*. The first part of the curve shown in **Figure 4.10** shows that the maximum force attained was about *485 μN*, which is very close to the *500 μN* applied in the experiments. **Figure 4.9** shows a quarter of the deformed nanolattice structure and from the image, it's possible to notice that only the four pillars in the center suffer considerable deformation. Because of that, only these four pillars were exported from Abaqus to COMSOL using HyperMesh. Then in COMSOL, these four pillars were subjected to constant force of *485 μN* for *120 seconds* as the defect diffusion was accounted for. The second part of the curve in **Figure 4.10** shows the resultant deformation caused by the defect diffusion in the four pillars.

After that, the procedure is repeated for the relaxation part of the simulation. First, the deformation depth is decreased to about *50 nm* as in the experiments (third part of the simulation curve in **Figure 4.10**). Then, the four pillars are exported to COMSOL once again where they are subjected to a constant force of about *10 μN* during for *120 seconds* in order to capture the relaxation deformation (fourth part of the simulation curve in **Figure 4.10**). Two types of defects were used to fit the experimental results. The material properties used for the Al_2O_3 nanolattice film include a Young's modulus $E = 180 \; GPa$, a Poisson ratio $\upsilon = 0.24$, partial molar volumes $\Omega_1 = \Omega_2 = 4.25 \times 10^{-23} \; cm^3$, and the diffusivities[29-32] of the two kinds of point defects are

3.1×10^{-13} and 2.5×10^{-14} cm^2/s and the set temperature is *300 K*. **Figure 4.11** shows the concentration evolution of a defect type across the thickness of one of the pillars.

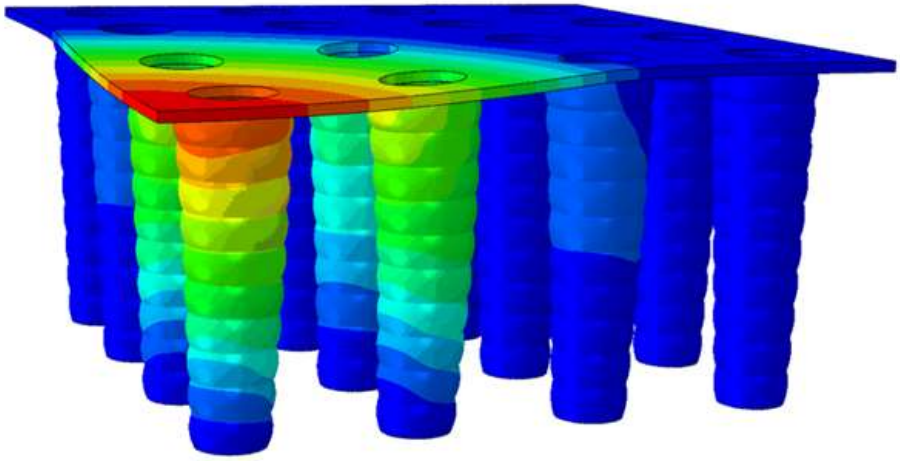

Figure 9 Deformed configuration of a 30 nm Al_2O_3 nanolattice structure subjected to a 90 nm indentation displacement.

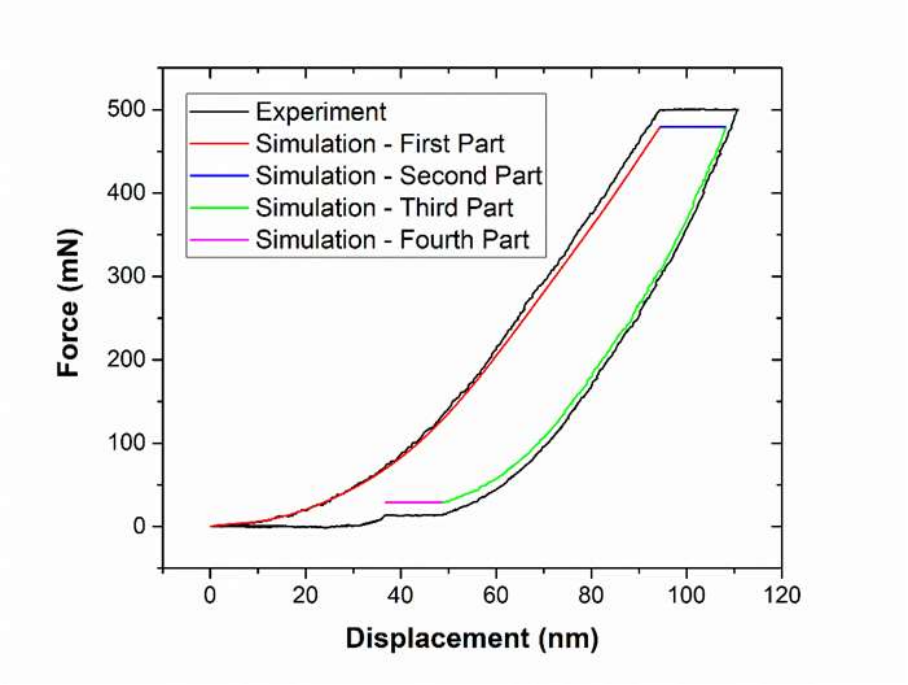

Figure 4.10 Force-displacement curve comparison between nanoindentation experiment and FEA model.

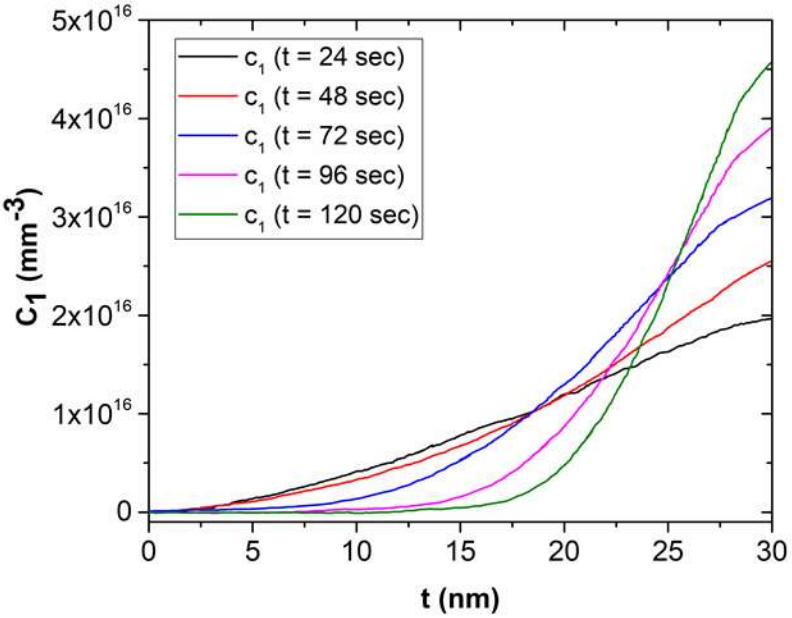

Figure 4.11 Concentration evolution of a defect type across the thickness of one of the pillars.

4.6 Conclusion

This work reported on the characterization of the mechanical properties of Al_2O_3 and ZnO nanolattice films, which compose a new class of mechanically robust material that can be applied over any surfaces as a thin film. Under normal compressive loading, the nanolattice film demonstrates near-linear scaling between relative modulus and density, high specific energy dissipation, and near-complete recoverability from strains of about *20%* for the thinnest shell samples. FEA modeling of the nanoindentation experiments helped in the calculation of the specific energy dissipation based on the deformed volume of material that undergoes larger strain than the failure threshold. Nanoindentation experiments also showed that Al_2O_3 nanolattices present anelastic behavior once the load applied to the sample is held constant for *120 seconds*. The theoretical analysis of point defect diffusion was implemented in FEA with PDE solving capabilities, modeling the anelastic response of the nanopillars.

REFERENCES

1. Meyers, M. A., Chen, P. Y., Lopez, M. I., Seki, Y., & Lin, A. Y., 2011, Biological materials: A materials science approach. J. Mech. Beha. Biomed. Mater., 4(5), 626-657;
2. Meyers, M. A., Chen, P. Y., Lin, A. Y. M., & Seki, Y., 2008, Biological materials: structure and mechanical properties. Prog. Mater. Sci., 53(1), 1-206;
3. Chen, P. Y., Lin, A. Y. M., McKittrick, J., & Meyers, M. A., 2008, Structure and mechanical properties of crab exoskeletons. Acta Biomater., 4(3), 587-596;
4. Chen, P. Y., Lin, A. Y. M., Lin, Y. S., Seki, Y., Stokes, A. G., Peyras, J., ... & McKittrick, J., 2008, Structure and mechanical properties of selected biological materials. J. Mech. Behav. Biomed. Mater., 1(3), 208-226;
5. Gibson, L. J., 2005, Biomechanics of cellular solids. J. Biomech., 38(3), 377-399;
6. Ando, K., & Onda, H., 1999, Mechanism for deformation of wood as a honeycomb structure II: First buckling mechanism of cell walls under radial compression using the generalized cell model. J. Wood Sci., 45(3), 250-253;
7. Tappan, B. C., Huynh, M. H., Hiskey, M. A., Chavez, D. E., Luther, E. P., Mang, J. T., & Son, S. F., 2006, Ultralow-density nanostructured metal foams: combustion synthesis, morphology, and composition. J. Am. Chem. Soc., 128(20), 6589-6594;
8. Verdooren, A., Chan, H. M., Grenestedt, J. L., Harmer, M. P., & Caram, H. S., 2006, Fabrication of Low-Density Ferrous Metallic Foams by Reduction of Chemically Bonded Ceramic Foams. J. Am. Ceram. Soc., 89(10), 3101-3106;
9. Chanda, M., & Roy, S. K., 2006, Plastics technology handbook. CRC press;
10. Lee, L. J., Zeng, C., Cao, X., Han, X., Shen, J., & Xu, G., 2005, Polymer nanocomposite foams. Compos. Sci. Technol., 65(15-16), 2344-2363;

11. Hüsing, N., & Schubert, U., 1998, Aerogels—airy materials: chemistry, structure, and properties. Angewandte Chemie International Edition, 37(1-2), 22-45;
12. Pierre, A. C., & Pajonk, G. M., 2002, Chemistry of aerogels and their applications. Chem. Rev., *102*(11), 4243-4266;
13. Ashby, M. F., & Johnson, K., 2013, Materials and design: the art and science of material selection in product design. Butterworth-Heinemann;
14. Gibson, L. J., & Ashby, M. F., 1999, Cellular solids: structure and properties. Cambridge university press;
15. Schaedler, T. A., Jacobsen, A. J., Torrents, A., Sorensen, A. E., Lian, J., Greer, J. R., ... & Carter, W. B., 2011, Ultralight metallic microlattices. Science, 334(6058), 962-965;
16. Zheng, X., Lee, H., Weisgraber, T. H., Shusteff, M., DeOtte, J., Duoss, E. B., ... & Kucheyev, S. O., 2014, Ultralight, ultrastiff mechanical metamaterials. Science, 344(6190), 1373-1377;
17. Meza, L. R., Das, S., & Greer, J. R., 2014, Strong, lightweight, and recoverable three-dimensional ceramic nanolattices. Science, 345(6202), 1322-1326;
18. Lee, J. H., Wang, L., Boyce, M. C., & Thomas, E. L., 2012, Periodic bicontinuous composites for high specific energy absorption. Nano letters, 12(8), 4392-4396;
19. Zhang, Q., Zhao, M., Liu, Y., Cao, A., Qian, W., Lu, Y., & Wei, F., 2009, Energy-absorbing hybrid composites based on alternate carbon-nanotube and inorganic layers. Adv. Mater., 21(28), 2876-2880;
20. Greaves, G. N., Greer, A. L., Lakes, R. S., & Rouxel, T., 2011, Poisson's ratio and modern materials. Nat. Mater., 10(11), 823;
21. Lakes, R., & Lakes, R. S., 2009, Viscoelastic materials. Cambridge University Press;

22. Cheng, G., Miao, C., Qin, Q., Li, J., Xu, F., Haftbaradaran, H., ... & Zhu, Y., 2015, Large anelasticity and associated energy dissipation in single-crystalline nanowires. Nat. Nanotechnol., 10(8), 687;
23. Zener, C., 1948, Elasticity and anelasticity of metals. University of Chicago press;
24. Nowick, A. S., 2012, Anelastic relaxation in crystalline solids (Vol. 1). Elsevier;
25. Chang, C. H., Tian, L., Hesse, W. R., Gao, H., Choi, H. J., Kim, J. G., ... & Barbastathis, G., 2011, From two-dimensional colloidal self-assembly to three-dimensional nanolithography. Nano Letters, 11(6), 2533-2537;
26. Bagal, A., Zhang, X. A., Shahrin, R., Dandley, E. C., Zhao, J., Poblete, F. R., ... & Chang, C. H., 2017, Large-Area Nanolattice Film with Enhanced Modulus, Hardness, and Energy Dissipation. Sci. Rep., 7(1), 9145;
27. Jen, S. H., Bertrand, J. A., & George, S. M., 2011, Critical tensile and compressive strains for cracking of Al2O3 films grown by atomic layer deposition. J. Appl. Phys., 109(8), 084305;
28. Tapily, K., Gu, D., Baumgart, H., Namkoong, G., Stegall, D., & Elmustafa, A. A., 2011, Mechanical and structural characterization of atomic layer deposition-based ZnO films. Semicond. Sci. Tech., 26(11), 115005;
29. Oishi, Y., & Kingery, W. D., 1960, Self-diffusion of oxygen in single crystal and polycrystalline aluminum oxide. J. Chem. Phys., 33(2), 480-486;
30. Paladino, A. E., & Kingery, W. D., 1962, Aluminum ion diffusion in aluminum oxide. J. Chem. Phys., 37(5), 957-962;
31. Tomlins, G. W., Routbort, J. L., & Mason, T. O., 1998, Oxygen diffusion in single-crystal zinc oxide. J. Am. Ceram. Soc., 81(4), 869-876;

32. Tomlins, G. W., Routbort, J. L., & Mason, T. O., 2000, Zinc self-diffusion, electrical properties, and defect structure of undoped, single crystal zinc oxide. J. Appl. Phys., 87(1), 117-123;